

NASA Contractor Report 4486

# Predicting Multi-Wall Structural Response to Hypervelocity Impact Using the Hull Code

William P. Schonberg  
*University of Alabama in Huntsville*  
*Huntsville, Alabama*

Prepared for  
George C. Marshall Space Flight Center  
under Contract NAS8-36955



National Aeronautics and  
Space Administration

Office of Management

Scientific and Technical  
Information Program

1993

N93-18406

Unclass

H1/18 0145782

(NASA-CR-4486) PREDICTING  
MULTI-WALL STRUCTURAL RESPONSE TO  
HYPERVELOCITY IMPACT USING THE HULL  
CODE (Alabama Univ.) 93 p



## TABLE OF CONTENTS

1.0	INTRODUCTION . . . . .	1
2.0	THE HYPERVELOCITY IMPACT PROCESS . . . . .	4
3.0	PART ONE: HULL CODE PREDICTIONS VS. EXPERIMENTAL RESULTS . . . . .	6
3.1	Introductory Comments . . . . .	6
3.2	Impact Parameters and Structural Configurations . . . . .	6
3.3	Comparison of Hull Code Predictions and Experimental Results . . . . .	8
3.3.1	Single-Bumper Systems -- Test-by-Test Comparison . . . . .	8
3.3.2	Double-Bumper Systems -- Test-by-Test Comparison . . . . .	10
3.3.3	Overall Response Comparison . . . . .	12
3.4	Concluding Comments . . . . .	13
4.0	PART TWO: PARAMETRIC STUDY OF HYPERVELOCITY IMPACT BY CYLINDRICAL PROJECTILES . . . . .	15
4.1	Introductory Comments . . . . .	15
4.2	Impact Parameters and Structural Configurations . . . . .	16
4.3	Results and Observations . . . . .	17
4.3.1	Single-Bumper Systems -- Spherical vs. Cylindrical Projectile Impact . . . . .	17
4.3.2	Single-Bumper Systems -- Effect of L/d Ratio . . . . .	19
4.3.3	Single-Bumper Systems -- Effect of Projectile Orientation . . . . .	21
4.3.4	Single vs. Double-Bumper System Impact . . . . .	23
4.4	Concluding Comments . . . . .	24
5.0	ACKNOWLEDGEMENTS . . . . .	25
6.0	REFERENCES . . . . .	26

PREDICTING MULTI-WALL STRUCTURAL RESPONSE TO HYPERVELOCITY

IMPACT USING THE HULL CODE

William P. Schonberg  
Associate Professor

Mechanical Engineering Department  
University of Alabama in Huntsville  
Huntsville, Alabama 35899

Figure Captions

- Figure 1 Normal Impact of a Single-Bumper Structure
- Figure 2 Normal Impact of a Double-Bumper Structure
- Figure 3 Final Output Frame, HULL Code Impact Simulation NR-26
- Figure 4a Pressure Wall Plate, Experimental Test No. EHSS-2B (Front)
- Figure 4b Pressure Wall Plate, Experimental Test No. EHSS-2B (Rear)
- Figure 5 Final Output Frame, HULL Code Impact Simulation NR-2
- Figure 6a Pressure Wall Plate, Experimental Test No. 115-3 (Front)
- Figure 6b Pressure Wall Plate, Experimental Test No. 115-3 (Rear)
- Figure 7 Final Output Frame, HULL Code Impact Simulation NR-3
- Figure 8a Pressure Wall Plate, Experimental Test No. 117-1 (Front)
- Figure 8b Pressure Wall Plate, Experimental Test No. 117-1 (Rear)
- Figure 9 Final Output Frame, HULL Code Impact Simulation NR-4
- Figure 10a Pressure Wall Plate, Experimental Test No. 117-2 (Front)

Figure 10b Pressure Wall Plate, Experimental Test No. 117-2 (Rear)

Figure 11 Ballistic Limit Curve, Single Bumper System, Normal Impact  
 $t_s = 1.6$  mm,  $t_w = 3.175$  mm,  $S = 10.16$  cm

Figure 12 Ballistic Limit Curve, Double Bumper System, Normal Impact  
 $t_{s1} = t_{s2} = 0.8$  mm,  $t_w = 3.175$  mm,  $S_1 = 2.54$  cm,  $S_2 = 7.62$  cm

Figure 13 Normal Unyawed Cylindrical Projectile Impact of a Single-Bumper Structure

Figure 14 Normal Unyawed Cylindrical Projectile Impact of a Double-Bumper Structure

Figure 15 Coordinate System for Yaw Angle Definitions

Figure 16 Example of Yawed Trajectory in the x-z Plane

Figure 17a HULL Code Impact Simulation NR-67 -- Spherical Projectile  
 $t = 0.000$   $\mu s$

Figure 17b HULL Code Impact Simulation NR-67 -- Spherical Projectile  
 $t = 9.000$   $\mu s$

Figure 17c HULL Code Impact Simulation NR-67 -- Spherical Projectile  
 $t = 14.836$   $\mu s$

Figure 18a HULL Code Impact Simulation NR-66 -- Cylindrical Projectile  
 $t = 0.000$   $\mu s$

Figure 18b HULL Code Impact Simulation NR-66 -- Cylindrical Projectile  
 $t = 6.000$   $\mu s$

Figure 18c HULL Code Impact Simulation NR-66 -- Cylindrical Projectile  
 $t = 12.710$   $\mu s$

Figure 19a HULL Code Impact Simulation NR-38 -- Cylindrical Projectile  
 $L/d = 2.0$ ,  $t = 0.000$   $\mu s$

- Figure 19b HULL Code Impact Simulation NR-38 -- Cylindrical Projectile  
 $L/d = 2.0$ ,  $t = 12.000 \mu s$
- Figure 19c HULL Code Impact Simulation NR-38 -- Cylindrical Projectile  
 $L/d = 2.0$ ,  $t = 30.000 \mu s$
- Figure 20a HULL Code Impact Simulation NR-44 -- Cylindrical Projectile  
 $L/d = 1.0$ ,  $t = 0.000 \mu s$
- Figure 20b HULL Code Impact Simulation NR-44 -- Cylindrical Projectile  
 $L/d = 1.0$ ,  $t = 10.000 \mu s$
- Figure 21a HULL Code Impact Simulation NR-45 -- Cylindrical Projectile  
 $L/d = 0.31$ ,  $t = 0.000 \mu s$
- Figure 21b HULL Code Impact Simulation NR-45 -- Cylindrical Projectile  
 $L/d = 0.31$ ,  $t = 15.000 \mu s$
- Figure 22a HULL Code Impact Simulation NR-42 -- Cylindrical Projectile  
 $L/d = 0.11$ ,  $t = 0.000 \mu s$
- Figure 22b HULL Code Impact Simulation NR-42 -- Cylindrical Projectile  
 $L/d = 0.11$ ,  $t = 20.000 \mu s$
- Figure 22c HULL Code Impact Simulation NR-42 -- Cylindrical Projectile  
 $L/d = 0.11$ ,  $t = 42.360 \mu s$
- Figure 23a HULL Code Impact Simulation NR-43 -- Cylindrical Projectile  
 $L/d = 0.0277$ ,  $t = 0.000 \mu s$
- Figure 23b HULL Code Impact Simulation NR-43 -- Cylindrical Projectile  
 $L/d = 0.0277$ ,  $t = 36.000 \mu s$
- Figure 23c HULL Code Impact Simulation NR-43 -- Cylindrical Projectile  
 $L/d = 0.0277$ ,  $t = 65.320 \mu s$
- Figure 24a HULL Code Impact Simulation NR-46 -- Cylindrical Projectile  
 $L/d = 0.11$ ,  $\theta = 60^\circ$ ,  $\phi = 0^\circ$ ,  $\psi = 90^\circ$ ,  $t = 0.000 \mu s$

- Figure 24b HULL Code Impact Simulation NR-46 -- Cylindrical Projectile  
 $L/d = 0.11$ ,  $\theta = 60^\circ$ ,  $\phi = 0^\circ$ ,  $\psi = 90^\circ$ ,  $t = 12.000 \mu s$
- Figure 24c HULL Code Impact Simulation NR-46 -- Cylindrical Projectile  
 $L/d = 0.11$ ,  $\theta = 60^\circ$ ,  $\phi = 0^\circ$ ,  $\psi = 90^\circ$ ,  $t = 28.265 \mu s$
- Figure 25a HULL Code Impact Simulation NR-48 -- Cylindrical Projectile  
 $L/d = 0.11$ ,  $\theta = 0^\circ$ ,  $\phi = 0^\circ$ ,  $\psi = 90^\circ$ ,  $t = 0.000 \mu s$
- Figure 25b HULL Code Impact Simulation NR-48 -- Cylindrical Projectile  
 $L/d = 0.11$ ,  $\theta = 0^\circ$ ,  $\phi = 0^\circ$ ,  $\psi = 90^\circ$ ,  $t = 12.000 \mu s$
- Figure 25c HULL Code Impact Simulation NR-48 -- Cylindrical Projectile  
 $L/d = 0.11$ ,  $\theta = 0^\circ$ ,  $\phi = 0^\circ$ ,  $\psi = 90^\circ$ ,  $t = 22.290 \mu s$
- Figure 26a HULL Code Impact Simulation NR-49 -- Cylindrical Projectile  
 $L/d = 0.11$ ,  $\theta = 0^\circ$ ,  $\phi = 60^\circ$ ,  $\psi = 0^\circ$ ,  $t = 0.000 \mu s$
- Figure 26b HULL Code Impact Simulation NR-49 -- Cylindrical Projectile  
 $L/d = 0.11$ ,  $\theta = 0^\circ$ ,  $\phi = 60^\circ$ ,  $\psi = 0^\circ$ ,  $t = 15.173 \mu s$
- Figure 26c HULL Code Impact Simulation NR-49 -- Cylindrical Projectile  
 $L/d = 0.11$ ,  $\theta = 0^\circ$ ,  $\phi = 60^\circ$ ,  $\psi = 0^\circ$ ,  $t = 23.564 \mu s$
- Figure 27 Critical Yaw Angle Calculation Geometry
- Figure 28a HULL Code Impact Simulation NR-39 -- Cylindrical Projectile  
Double-Bumper System,  $L/d = 2.0$ ,  $t = 0.000 \mu s$
- Figure 28b HULL Code Impact Simulation NR-39 -- Cylindrical Projectile  
Double-Bumper System,  $L/d = 2.0$ ,  $t = 6.000 \mu s$
- Figure 28c HULL Code Impact Simulation NR-39 -- Cylindrical Projectile  
Double-Bumper System,  $L/d = 2.0$ ,  $t = 18.000 \mu s$
- Figure 29a HULL Code Impact Simulation NR-47 -- Cylindrical Projectile  
Double-Bumper System,  $L/d = 0.0277$ ,  $t = 0.000 \mu s$
- Figure 29b HULL Code Impact Simulation NR-47 -- Cylindrical Projectile  
Double-Bumper System,  $L/d = 0.0277$ ,  $t = 24.000 \mu s$

Figure 29c HULL Code Impact Simulation NR-47 -- Cylindrical Projectile  
Double-Bumper System,  $L/d = 0.0277$ ,  $t = 79.641 \mu s$



### Notation

$A_d$	pressure wall plate damage area
$A_s$	pressure wall plate rear-side spall area
$C_o$	material sound velocity
$d$	base diameter of cylindrical projectile; spherical projectile diameter
$d_h$	pressure wall plate equivalent single hole diameter
$D$	bumper plate hole diameter, single-bumper system
$D1, D2$	outer, inner bumper plate hole diameter, double-bumper system
$K$	slope of shock velocity-particle velocity curve
$L$	length of cylindrical projectile
$S$	bumper plate/pressure wall plate stand-off distance, single-bumper system
$S_1$	outer bumper plate/inner bumper plate stand-off distance, double-bumper system
$S_2$	inner bumper plate/pressure wall plate stand-off distance, double-bumper system
$t_s$	bumper plate thickness, single-bumper system
$t_{s1}, t_{s2}$	outer, inner bumper plate thickness, double-bumper system
$t_w$	pressure wall plate thickness
$U_s$	shock wave velocity
$V$	impact velocity
$\theta$	impact trajectory obliquity
$\gamma$	debris cloud cone angle, single-bumper system
$\phi$	yaw angle in x-z plane
$\phi_{cr}$	critical yaw angle in x-z plane
$\psi$	yaw angle in y-z plane



## 1.0 INTRODUCTION

Hydrocodes are a valuable numerical tool for the analysis of hypervelocity impact phenomena. Part of their value lies in their ability to provide detailed information about the impact process which may be difficult or impossible to obtain experimentally. For example, in the study of the response of multi-wall structures under hypervelocity impact, the growth of the debris cloud created by the impact of the projectile with the first wall, or bumper plate, may be a point of interest. While it may be possible to record the spread of the debris cloud experimentally (see, e.g. [1-4]), velocity and density distributions within the debris cloud are more easily obtained from a numerical simulation of the impact event (see, e.g., [5,6]). Additionally, impact conditions such as velocity, trajectory, etc., can be more precisely controlled in numerical simulations than in experimental tests where a range of uncertainty always exists. Once a numerical impact simulation scheme has been validated through comparison with experimental data, it can be used, albeit with great care, to extrapolate response characteristics in impact regimes where testing cannot be performed.

Over the last three decades, multi-wall structures have been analyzed extensively, primarily through experiment, as a means of increasing the protection afforded to the interior of habitable spacecraft (see, e.g., [7-12]). This work has contributed significantly to the design of spacecraft that will be exposed to high-speed impacts by pieces of orbital space debris, such as the habitable modules of the Space Station Freedom. However, as structural configurations become more varied (material composition, geometry, etc.), the number of tests required to characterize the response of such structures and the cost of such tests has increased dramatically.

Although several analytical techniques have been developed to model the response of multi-wall structures under high speed projectile impact, the calculations involved often become unruly for geometries and material properties even slightly removed from the simplest assumptions (see, e.g., [13,14]). As an alternative to experimental testing and analytical models, numerical modeling of high-speed impact phenomena has enjoyed a fairly high level of use and success in predicting the response of a variety of structural systems under different kinds of impact loading conditions [15,16]. However, it is incumbent upon the user of numerical impact simulation codes to be fully aware of their limitations with respect to the particular geometry and impact conditions under consideration.

This report presents the results of a two-phase numerical/experimental investigation of the hypervelocity impact response of multi-wall structures. In the first phase, the results of a series of experimental high-speed impact tests are compared against the predictions of the HULL hydrodynamic computer code. The results of this comparative analysis are presented in Part One of this report. In the second phase, a numerical parametric study of multi-wall structural response to hypervelocity cylindrical projectile impact was performed. These results are presented in Part Two of this report.

The numerical impact simulation results were generated on the NASA/Marshall Space Flight Center Cray X/MP supercomputer using the HULL hydrodynamic computer code (hereafter referred to as the 'HULL code'), a Eulerian finite difference code with explicit time integration. In the HULL code, an elastic/plastic constitutive law with work hardening and thermal softening was employed with an ultimate strength failure criterion and the Mie-Gruneir-

sen equation of state. The hypervelocity impact testing was performed at the Space Debris Simulation Facility of the Materials and Processes Laboratory at the NASA/Marshall Space Flight Center. This Facility consists of a two-stage light gas gun capable of launching 2.5 mm to 12.7 mm projectiles at velocities of 2 to 8 km/sec [17].

In both phases of this investigation, the conditions of the numerical impact simulations and the experimental tests were chosen to simulate the orbital debris impact of light-weight space structures as closely as possible, and still remain within the realm of experimental and numerical feasibility. Kessler, et.al., [18] state that the average mass density for orbital debris particles less than 10 mm in diameter is approximately 2.8 gm/cm<sup>3</sup>, which is approximately that of aluminum. Therefore, the projectile material for the experimental tests and numerical simulations was chosen to be aluminum 1100-0.

## 2.0 THE HYPERVELOCITY IMPACT PROCESS

Consider the hypervelocity impact of a multi-wall structure by a spherical projectile of diameter  $d$  traveling at velocity  $V$ . Figure 1 illustrates the normal impact of a single-bumper system while Figure 2 shows the normal impact of a double-bumper system. In the single-bumper system impact, the projectile collides initially with the protective bumper (thickness  $t_s$ ), which is a relatively thin layer of material placed at a small distance  $S$  in front of the pressure wall (thickness  $t_w$ ) of the structural system. Upon impact, strong shock waves propagate through both the projectile and the bumper plate. The pressures associated with these shocks typically exceed the strength of the projectile and bumper plate materials. As the shock waves propagate, the projectile and bumper materials are heated adiabatically and non-isentropically. The release of the shock pressures occurs isentropically through the action of rarefaction waves that are created as the shock waves interact with the free surfaces of the projectile and bumper plate. This process leaves the projectile and bumper materials in high energy states and can cause either or both to fragment, melt, or vaporize, depending on material properties, geometry, and the impact velocity.

The bumper plates in multi-wall systems protect the pressure wall plates against perforation by causing the disintegration of the impacting projectiles and the creation of diffuse debris clouds which impart significantly lower impulsive loadings to the pressure wall plates. In the single-bumper system impact shown in Figure 1, the debris cloud (with cone angle  $\gamma$ ) travels towards and impacts the pressure wall plate. In the double-bumper system impact shown in Figure 2, the debris cloud created as a result of the impact on the outer bumper plate first travels toward and impacts the inner

bumper plate. This creates another debris cloud which then travels toward and impacts the pressure wall plate. In either case, an area of damage  $A_d$  is created on the pressure wall plate. The size of this impulsively loaded area is governed by the manner in which the projectile and bumper plate(s) fragment, melt, or vaporize, and by the spacing(s) between the bumper plate(s) and the pressure wall plate. Occasionally the impact of a debris cloud on the pressure wall plate results in rarefaction stresses near the rear surface of the pressure wall that exceed the dynamic tensile strength of the pressure wall material. In these cases, spall fragments are ejected at high velocities from the rear side of the pressure wall, creating an area of rear surface spall  $A_s$ .

### 3.0 PART ONE: HULL CODE PREDICTIONS VS. EXPERIMENTAL RESULTS

#### 3.1 Introductory Comments

In this part, the results of a study in which experimental hypervelocity impact response characteristics of multi-wall structures were compared against the predictions of the HULL code are presented and discussed. Following these introductory comments and a discussion of the experimental and numerical test parameters, a comparative analysis is performed between experimental results and numerical predictions of multi-wall structural response under hypervelocity projectile impact. This analysis consists of test-by-test comparisons and a comparison of numerically and experimentally generated ballistic limit curves. The comparative analyses performed reveals many interesting features of Hull code prediction capabilities for multi-wall structures under a variety of hypervelocity impact conditions.

#### 3.2 Impact Parameters and Structural Configurations

To maintain repeatability and consistency, spherical projectiles with diameters from 0.25 to 1.0 cm were used in this part of the investigation. The impact velocities of the numerical impact simulations ranged from 0.5 to 6.9 km/s, while in the experimental impact tests, the impact velocities ranged from 3.0 to 6.9 km/s. Two types of multi-wall structures were considered: single-bumper and double-bumper. In all cases, experimental and numerical, the bumper plates were aluminum 6061-T6 and the pressure wall plates were aluminum 2219-T87. In the single-bumper systems, the bumper plates were 1.6 mm thick; in the double-bumper systems, each bumper was 0.8 mm thick for a total bumper thickness of again 1.6 mm. In all of the single-bumper systems, the stand-off distance between the bumper plate and pressure wall was kept constant at 10.16 cm. In the double-bumper systems,



although various combinations of intermediate stand-off distances were considered, the total stand-off distance between the outer bumper plate and the pressure wall plate was also kept constant at 10.16 cm. In all of the experimental tests and numerical impact simulations, the thicknesses of the pressure wall plates was kept constant at 3.175 mm.

The mechanical and thermal properties of the projectile, bumper plate, and pressure wall plate materials are presented in Table 1. These are the values used as input by the HULL code in the impact simulations performed for this investigation. In Table 1, 'ambient melt energy' and 'ambient vaporization energy' refer to internal energies at the inception of material melt and vaporization, respectively. Additional numerical simulation and experimental test parameters are given in Tables 2 and 3 for single- and double-bumper systems, respectively. In Tables 2,3, and subsequent results comparison tables, an 'NR-' prefix is used to designate a HULL code impact simulation; all tests without an 'NR-' prefix are experimental impact tests.

The test-by-test comparisons of the experimental results and the numerical predictions are given in Tables 4 and 5; additional impact simulation results are given at the ends of these Tables. These additional impact simulations were performed for the construction of ballistic limit curves. In Tables 4 and 5, experimental and numerical results are grouped according to both geometric and impact energy similarity. It is noted that in these tables, entries of '-----' indicate that certain phenomena, such as pressure wall perforation or front surface crater damage, did not occur. Additionally,  $d_h$  is the equivalent single hole diameter of all the holes in the pressure wall plate in the event of pressure wall perforation. Figures 3 through 10 show final HULL code output frames and photographs of damaged

pressure wall plates of corresponding experimentally-tested multi-wall systems. Finally, Figures 11 and 12 present a comparison of numerical and experimental ballistic limit curves for some of the single-bumper systems and double-bumper systems, respectively, that were considered in this investigation. It is noted that the curves in Figures 11 and 12 are merely lines of demarcation between regions of pressure wall perforation (above) and no perforation (below).

### 3.3 Comparison of Hull Code Predictions and Experimental Results

#### 3.3.1 Single-Bumper Systems -- Test-by-Test Comparison

A test-by-test comparison of numerical predictions and experimental results for the single-bumper systems impact revealed a number of discrepancies between observed phenomena and HULL code predictions. Although there was good agreement for the diameter of the hole in the bumper plate, significant differences were found to exist between prediction and observation of the debris cloud cone angles, the extent of the pressure wall damage areas, whether or not pressure wall perforation had occurred, and the diameters of the pressure wall holes in the event of a perforation (Table 4).

Without exception, HULL code predictions of pressure wall damage areas and cone angles were smaller than the corresponding experimental values. On the average, the HULL code underpredicted pressure wall damage areas by approximately 56%, with a standard deviation of approximately 20%. This underprediction of the damage areas by the HULL code was partly due to the fact that the HULL code simulations were terminated somewhat prematurely and partly due to an inadequate material response modelling within the HULL code. Had the impact simulation been allowed to run for several more micro-

seconds, the debris cloud would have had that much more time to expand. Its impact would then have naturally resulted in a somewhat larger damage area. However, because an instantaneous failure criterion was used, the bumper and projectile material that formed the debris cloud was not allowed to expand fully in the numerical scheme before failing (i.e. fragmenting) and creating the debris cloud.

With regard to the discrepancies between HULL code predictions of pressure wall perforation and experimental results, the HULL code agreed with experimental observations of pressure wall perforation or no perforation in 2 out of 6 cases. In the 2 cases where agreement existed, 1 was a perforation and 1 was a perforation. Where both HULL predicted and experiment showed pressure wall perforation, HULL agreed with the nature of the perforation (i.e. a single small hole) but predicted a hole diameter slightly larger than that which was observed experimentally (Table 4). In addition, the HULL code predicted a centrally-located hole whereas the hole in the experimental test was slightly off-center. The symmetric location of the hole in the HULL code run was obviously due to the symmetric nature of the numerical scheme. In the testing of real structures and materials, where voids and manufacturing defects are invariably present, such symmetric response will rarely occur.

Finally, although rear-side spallation of the pressure wall plate occurred frequently in single-bumper system impact, it was never predicted by the HULL code (Table 4). Figures 4a,b show the front and rear surfaces of a pressure wall plate that exhibited extensive rear-side spallation. Figure 3 shows the final output frame of the corresponding HULL code run. In order to be able to predict rear-side spallation, a significant increase in the

number of zones utilized by HULL is required [15]. However, this increase would also increase memory requirements and run times. Thus, unless a significant investment of computer time and funds is possible, it appears that the HULL code cannot be used to study rear-side spallation phenomena in multi-wall systems under high-speed impact.

### 3.3.2 Double-Bumper Systems -- Test-by-Test Comparison

A comparison of experimental results and numerical predictions for double-bumper systems under spherical projectile impact revealed that there were again differences between predicted and observed pressure wall damage (Table 5). The HULL code impact simulations over-predicted the pressure wall damage areas by an average of approximately 6%, with a standard deviation of approximately 56%. However, as indicated by the high value of the standard deviation, this 'small' average difference is the result of a fortuitous combination of 'large' over- and under-predictions of damage areas by the HULL code.

An examination of the differences in pressure wall damage areas in cases where the impact energy of the HULL code simulations matched exactly those of the experimental tests revealed that a correlation may have existed between the arrangement of the bumper plates and the over- or under-prediction of pressure wall damage areas by the HULL code. When the outer and inner bumpers were close together, the HULL code under-predicted pressure wall damage area by approximately 34%. When the inner bumper plate was moved closer to the pressure wall plate, the numerically predicted pressure wall damage area went from an under-predicted value to an over-predicted value: in those cases where the outer and inner bumpers were far apart, the

HULL code over-predicted pressure wall damage areas by approximately 76%.

HULL code predictions of pressure wall perforation or no perforation agreed with experiment in all 8 cases (Table 5). Of these 8 cases, 7 were perforations and 1 was a no perforation. However, the nature of the perforation as predicted by the HULL code did not always agree with that which was observed experimentally. In the 7 cases of pressure wall perforation, the HULL code predicted single holes in each case (with relatively large holes in 2 cases) while experimental results showed single holes in 3 tests (although one test resulted in a pin-hole), a double-hole in 1 test, and through-cracks in 3 tests. In the instances where the HULL code predicted and experiment showed clear-through pressure wall holes, the hole diameters predicted by the HULL code were on average twice as large as those observed experimentally.

Figures 5 through 10 show final HULL code output frames and photographs of damaged pressure wall plates from corresponding experimentally tested double-bumper systems. These figures illustrate some of the interesting similarities and discrepancies between HULL code predictions of pressure wall damage and experimental results. In Figures 5 and 6, the location of the pressure wall plate hole is predicted by the HULL code to be centrally located while the experimental test showed the hole to be located slightly off-center. Some major differences between HULL code predictions and experimental results are evident in Figures 7 through 10. In Figures 7 and 9, it can be seen that the HULL code predicted rather large central holes in the pressure wall plates. Although no clear holes are evident in Figures 7 and 9, the extreme necking of the material in the circled regions implies that had the numerical impact simulations been allowed to run for a few more

microseconds, complete perforations similar to that shown in Figure 5 would have occurred. As can be seen in Figures 8a,b and 10a,b, the experimental tests of the corresponding double-bumper systems resulted in a pressure wall plate with a through-crack and a pressure wall plate with a central bulge and a pin-hole perforation. Thus, although the HULL code agreed with experiment as to whether or not pressure wall perforation occurred, the exact details of the predicted and observed perforation are significantly different.

Finally, there was excellent agreement between HULL code predictions and experimental results for the diameter of the hole in the outer bumper plate (Table 5). However, the HULL code under-predicted the diameter of the hole in the inner bumper by an average of approximately 43%. This is again due to the fact that in the HULL code impact simulations, the primary debris clouds were not able to expand as rapidly as they did in the experimental tests. In addition, although the Hull code agreed with experiment in not showing any rear-side spallation of pressure wall plates in double-bumper systems, this was probably due to the inability of the Hull code to predict spall in such systems using the parameters with which it was run.

### 3.3.3 Overall Response Comparison

The ability of the Hull code to predict overall system response was studied by comparing ballistic limit curves generated with Hull code and experimental data. Using the numerical results in Table 4, a ballistic limit curve was obtained for aluminum single-bumper systems with  $t_s=1.6$  mm,  $t_w=3.175$  mm and  $S=10.16$  cm under spherical projectile impact. This plot is shown in Figure 11 superposed on an experimental ballistic limit curve for the same structural system which was obtained from Figure 3.2 in [12]. A

comparison of the two curves reveals fairly close agreement at velocities above approximately 4 km/sec. No experimental results were generated at speeds lower than 3 km/sec; hence, no comparisons can be made for low velocity impacts. A similar observation can be made by comparing the numerical and experimental ballistic limit curves for aluminum double-bumper systems with  $t_{s1}=t_{s2}=0.8$  mm,  $t_w=3.175$  mm,  $S_1=2.54$  cm and  $S_2=7.62$  cm (Figure 12). In Figure 12, the numerical curve was generated using the data in Table 5 while the experimental curve was taken from Figure 8.3 in [12]. Based on these observations, it appears that the HULL code correctly predicts the ballistic limit curves for the single- and double-bumper systems considered in this study, especially in the velocity range 4 to 7 km/sec.

### 3.4 Concluding Comments

A comparative study between HULL code predictions and experimental observations of hypervelocity impact response has been successfully performed. In a test-by-test comparison, differences between numerical prediction and test result were frequently observed for single- and double-bumper configurations impacted by hypervelocity projectiles. For the single-bumper systems, the most serious discrepancies were in the magnitudes of the damage areas on the pressure wall plates and whether or not perforation or spallation of the pressure wall occurred due to the hypervelocity impact loading. For the double-bumper systems, there was good agreement between prediction and test result with respect to pressure wall plate perforation. However, the Hull code predictions differed from test results in the nature of the perforation and the extent of the damage areas on the pressure wall plates. Finally, a comparison of perforation curves generated with experimental and Hull code data revealed good agreement between observed and predicted bal-

listic limit curves for both single- and double-bumper systems at velocities between approximately 4 and 7 km/sec.

Based on these observations, it appears that HULL code predictions of hypervelocity impact response characteristics of a specific multi-wall system (i.e. pressure wall perforation or no perforation, pressure wall hole diameter in the event of a perforation, pressure wall damage area, etc.) can be inaccurate and misleading. Serious errors in system design can occur if the design were to be based on a small number of Hull code predictions of impact response. However, if a wide range of impact loading conditions are considered, then the ballistic limit curve of the system generated from the entire series of numerical simulations can be used as a relatively accurate indicator of actual system response.



## 4.0 PART TWO: PARAMETRIC STUDY OF HYPERVELOCITY IMPACT

### BY CYLINDRICAL PROJECTILES

#### 4.1 Introductory Comments

While cylindrical projectile impact has long been of interest to the impact mechanics community, the majority of the work performed has been with long rod projectiles (i.e.  $L/d \gg 1$ ) and has been focused primarily on the response of thin and thick single-plate targets to impacts at speeds on the order of 1-3 km/sec (see, e.g., [19-23]). Unfortunately, because of the significant changes in target response that occur as impact velocity is increased, it is difficult to extrapolate the results of such 'low' velocity single-plate studies to multi-wall structures under 'high' velocity or 'hypervelocity' impact. Furthermore, hypervelocity impact testing of multi-wall structures with non-spherical projectiles has been very limited in scope. Such testing was often included as a small part of a much larger test program that, for the most part, employed spherical projectiles (see, e.g., [3,6]). However, the test results did show that projectile shape does affect the perforation response of multi-wall structures (see also [24]). Orbital debris particles are in general not spherical and can impact an orbiting spacecraft at speeds in excess of 5 km/sec, in order to optimize the design of a structure destined for the orbital debris environment, it is important for the design engineer to be aware of the many damage modes possible in multi-wall structures under a variety of hypervelocity projectile impact conditions.

Since the response of multi-wall structures to spherical projectile impact has been relatively well-analyzed, the objective of this part of the investigation was to perform a numerical parametric study of multi-wall

structural response to high speed cylindrical projectile impact. Following these introductory comments and a discussion of the numerical impact simulation parameters, the results of the parametric study are presented and discussed. Impact simulation results for a variety of different cylindrical projectiles and impact conditions are reviewed qualitatively and quantitatively. Impact damage in the structural systems is characterized according to the extent of pressure wall perforation and crater damage as a result of the impact loadings. The parametric analyses performed revealed many interesting features of multi-wall structural response to hypervelocity cylindrical projectile impact conditions. However, in light of the conclusions drawn at the end of the first phase of this investigation, the results obtained in this phase and presented in this part of the report are used only to observe response trends and are not intended to be used to predict specific impact response characteristics.

#### 4.2 Impact Parameters and Structural Configurations

To assess the effect of projectile shape on structural response, equal-mass spherical and cylindrical projectiles were used in the numerical impact simulations; the L/d values of the cylindrical projectiles were varied from 0.0277 to 3.0. Two types of multi-wall structures were considered in this part of the investigation: single-bumper and double-bumper. In each case, the bumper plates and pressure wall plates were 6061-T6 and 2219-T87 aluminum, respectively. The mechanical and thermal properties of the projectile, bumper plate, and pressure wall plate are presented in Table 1. These are the values used as input by the HULL code in the impact simulations performed for this investigation. Additional numerical impact simulation parameters are given in Table 6 in which the angle  $\theta$  is the trajectory

obliquity measured from the vertical, that is,  $\theta=0^\circ$  is a normal impact.

Tables 7 through 10 present the results of the numerical parametric study. In Tables 7 through 10, experimental and numerical results are grouped according to both geometric and impact energy similarity. It is noted that in these Tables, entries of '----' indicate that certain phenomena, such as pressure wall perforation or front surface crater damage, did not occur. Additionally,  $d_h$  is the equivalent single hole diameter of all the holes in the pressure wall plate in the event of pressure wall perforation. Figures 13 and 14 illustrate the normal impact of an unyawed cylindrical projectile of diameter  $d$  and length  $L$  travelling at a velocity  $V$  on a single- and double-bumper system, respectively. In Figure 15, coordinate axes are superimposed on a cylindrical projectile in order that trajectory yaw angles may be defined. Specifically, the yaw angles  $\phi$  and  $\psi$  are defined to be the yaw angles in the x-z and y-z planes, respectively (see, e.g., Figure 16). In this manner, a normal 'straight-on' disk or cylinder has yaw angles of  $\phi=\psi=0^\circ$  while a normal 'edge-on' disk or cylinder has yaw angles of  $\phi=0^\circ$  and  $\psi=90^\circ$ . Figures 17 through 26 and 28,29 show pertinent HULL code output frames that are used for more detailed impact response comparisons; Figure 27 shows the geometry of a yawed impact for a critical yaw angle calculation.

#### 4.3 Results and Observations

##### 4.3.1 Single-Bumper Systems -- Spherical vs. Cylindrical Projectile Impact

A comparison of single-bumper system response to spherical and cylindrical projectile impact clearly demonstrated the effect of projectile geometry on system response. When the projectile trajectory was normal to the bumper plate, it was found that cylindrical projectiles with large  $L/d$

ratios (ie. long rods) were more damaging than equal-mass spherical projectiles (Table 7). In the spherical projectile impacts, the projectile and the bumper plate were completely fragmented and a disperse debris cloud was created (see, e.g., the HULL code output for NR-67 in Figures 17a-c). However, when a long rod impacted the bumper plate, only the front portion of the cylinder was fragmented, leaving the remaining rear section intact. For example, in NR-66 ( $L/d=3.0$ ), nearly one-third of the original cylindrical projectile was left undisturbed after the projectile had passed through the bumper plate (Figure 18b). Eventually, this large projectile fragment perforated the pressure wall plate (Figure 18c). Similarly, in NR-68 and NR-38, the portions of the rod which remained intact after passing through the bumper plates had sufficient energy to perforate the pressure wall plates.

As the  $L/d$  ratio decreased to unity, cylindrical and spherical projectile impacts were observed to inflict similar levels of damage to the pressure wall plates of single-bumper systems. This is in agreement with the results of a previous experimental study of the effects of projectile shape on the hypervelocity impact response of dual-wall structures [25]. For example, in the comparing the results of NR-38, NR-44, and NR-45, as the  $L/d$  ratio decreased from 2.0 to 0.31, the damage sustained by the pressure wall plate decreased markedly (Table 7). In fact, in NR-45 ( $L/d=0.31$ ), the impact of the cylindrical projectile on the bumper plate resulted in complete fragmentation of the projectile. Subsequently, there was no measurable damage to the pressure wall plate. In this case, the debris cloud created strongly resembled that observed in NR-24, the corresponding spherical projectile impact test.

#### 4.3.2 Single-Bumper Systems -- Effect of L/d Ratio

It was found that the cylindrical projectiles considered in this study could be divided into three groups depending on their L/d ratios. These groups are 'long rods' ( $L/d > 1$ ), 'compact rods' ( $L/d \approx 1$ ) and 'thin disks' ( $L/d < 1$ ). Figures 19 through 23 demonstrate the changes in debris cloud composition and pressure wall response for single-bumper system impacts as the L/d ratio was decreased from 2.0 to 0.0277 while the mass of the impacting projectile was kept constant.

As noted previously, when a long-rod projectile impacted a single-bumper system, complete fragmentation of the projectile upon impact with the bumper failed to occur. For example, in NR-38 ( $L/d = 2.0$ ), the solid fragment remaining after bumper plate impact went on to perforate the pressure wall plate (see the results for NR-38 in Figure 19a-c and in Table 8). As the L/d ratio decreased to unity, more complete fragmentation of the projectile occurred, which in turn resulted in an increase in the spread of the debris cloud. As a result, although the crater damage area increased, the perforation threat of the projectile decreased (see, e.g., the results for NR-44 in Table 8 and compare with those for NR-38). In Figures 20a,b and 21a,b, cylindrical projectiles with L/d ratios of 1.0 and 0.31, respectively, are seen to be completely broken up by the bumper plates and cause minimal damage to the pressure wall plates. Finally, in the thin disk impacts ( $L/d = 0.11$  and  $0.0277$ ), intact sections of the bumper plate were ripped away and sent speeding towards the pressure wall plate. In addition, for these L/d ratios, the debris clouds were noticeably 'spiked' in appearance (see Figures 22a-c and 23a-c). The spiked shape of the debris clouds and the large fragments contained within them eventually resulted in pressure wall

perforation and extreme pressure wall deformation to the point of incipient perforation (Figures 22c and 23c, respectively).

It is interesting to note that the projectiles in NR-42 and NR-45 appear to be in a transition region between 'compact rod' and 'thin disk' projectiles. In NR-45, the debris cloud produced by the impact of a cylindrical projectile with  $L/d=0.31$  quickly degraded into very small particles which cause no measurable pressure wall damage. This behavior resembled that observed in NR-44 where  $L/d=1.0$ . On the other hand, in NR-42 where  $L/d=0.11$ , a small disk appeared to be present at the leading edge of the debris cloud as it left the bumper plate immediately after impact. This behavior resembled that observed in NR-43 where  $L/d=0.0277$ . It would appear, therefore, that for the projectile and target materials considered in this study, a transition from a compact rod to a thin disk projectile occurs between  $L/d=0.31$  and  $L/d=0.11$  or approximately at  $L/d=0.2$ .

#### 4.3.3 Single-Bumper Systems -- Effect of Projectile Orientation

From Table 9, it can be seen that, of the different projectile orientations investigated, normal and oblique edge-on disk impacts (e.g. NR-48 and NR-46, respectively) were more damaging to the pressure wall than normal straight-on (e.g. NR-42) and yawed (e.g. NR-49) impacts. This can be seen by comparing the pressure wall hole diameters for these four tests in Table 9 and the HULL code output in Figures 22 and 24 through 26. In tests NR-46 and NR-48 (Figures 24a-c and 25a-c, respectively), the pressure wall was impacted by a large debris cloud containing large bumper plate and projectile fragments. Although the impact of NR-42 created a spiked debris cloud with a high mass concentration at the leading tip of the cloud (see Figures

22a-c), the high degree of projectile fragmentation resulted in a smaller pressure wall plate hole than in NR-46 and NR-48 (compare Figures 22c, 24c, and 25c). The least damaging projectile orientation was that of the disk in NR-49, in which the projectile had a yaw angle of  $\phi=60^\circ$ . The normal impact of this yawed projectile also resulted in a high degree of fragmentation and did not perforate the pressure wall plate (see Figures 26b,c).

The harmlessness of the yawed impact considered in this study can be explained by using a relatively simple model of yawed cylindrical projectile impact [26]. Consider the normal impact at velocity  $V$  of a cylindrical projectile whose longitudinal axis is yawed an angle  $\phi$  with respect to the trajectory of the projectile (Figure 27). In Figure 27, point A is a point of contact between the projectile and the surface of the target, point B is a point along the surface of the projectile facing the target, and point C is the projection of point b onto the surface of the target. We define a 'critical angle of yaw'  $\phi_{cr}$  such that if  $\phi=\phi_{cr}$ , then the shock wave generated along the target-facing surface of the projectile will reach point B at exactly the same time that point B will reach the target surface (at point C). Given this definition of  $\phi_{cr}$ , two possibilities arise. First, if  $\phi<\phi_{cr}$ , then the shock wave will reach point B after point B strikes the target surface. In this case, the amplitude and duration of the shock pressures along the projectile/target interface will be essentially the same as that for an impact of the same projectile at the same velocity without yaw (ie.  $\phi=0^\circ$ ). Second, if  $\phi>\phi_{cr}$ , then the shock wave will reach point B before point B strikes the target surface. In this case, the full shock pressure will exist only at the initial point of impact. At other points along the projectile surface facing the target, the projectile material will

be shocked and partially released before striking the target surface. As a result, the shock pressures generated upon impact will be lower in magnitude and will have a shorter duration than those generated in a yawed impact where  $\phi > \phi_{cr}$ .

To find  $\phi_{cr}$ , we note that if  $\phi = \phi_{cr}$ , then

$$BC/V_o = AB/U_s \quad (1)$$

that is, the time required for the shock wave to reach point B ( $AB/U_s$ ) is equal to the time required for point B to reach point C ( $BC/V$ ), where  $U_s$  is the projectile material shock wave velocity. Rearranging eqn (1) yields

$$V_o/U_s = BC/AB = \sin(\phi_{cr}) \quad (2)$$

so that

$$\phi_{cr} = \sin^{-1}(V/U_s) \quad (3)$$

Finally, for a like material-like material impact, the shock wave velocity is related to the impact velocity through the relationship

$$U_s = C_o + KV/2 \quad (4)$$

For the projectile and target materials in NR-49 (both aluminum),  $C_o \approx 5.2$  km/sec and  $K \approx 1.38$ . For  $V = 6.0$  km/sec, equations (3,4) yield a critical yaw angle of  $\phi_{cr} \approx 40^\circ$ . Based on the discussion in the preceding paragraph, since the yaw angle of NR-49 exceeds  $\phi_{cr}$ , the projectile in NR-49 has already begun to deteriorate by the time it completely passes through the bumper plate. This explains why the debris cloud is larger in NR-49 than in NR-42 and NR-46 and why the impact is relatively harmless.



#### 4.3.4 Single vs. Double-Bumper System Impact

As expected, it was found that double bumper systems offered more pressure wall protection against perforation by cylindrical projectiles with large L/d ratios than did equal-weight single bumper systems. The most dramatic illustration of this can be seen by comparing the results for NR-39 in which a long rod impacted a double-bumper system with those for NR-38 in which an the sme long rod impacted an equal-weight single-bumper system (Table 10). While a large section of the long rod projectile remained intact after impact with the single bumper in NR-38 (Figure 19b) and the first bumper in NR-39 (Figure 28b), the second bumper in NR-39 caused additional projectile fragmentation. As a result, the pressure wall of NR-39 was not perforated and suffered only minor damage (Figure 28c) while that of NR-38 was completely perforated (Figure 19c).

In case of thin disk impact (NR-47 and NR-43 in Table 10), the impact of the disk on the single bumper of NR-43 and the first bumper of NR-47 caused intact sections of the bumper plates to rip away and travel towards either the pressure wall in the single-bumper system or the inner bumper of the double-bumper system (Figures 23b and 29b, respectively). Although neither system was perforated, in the double-bumper system the impact of the outer bumper and projectile fragments on the inner bumper caused more complete fragmentation to occur than that which was observed in the single-bumper system (compare Figures 23c and 29c). Therefore, it would appear that the pressure walls of single-bumper configurations would also be at a greater risk of perforation by thin disk projectiles than the pressure walls of equal-weight double-bumper systems.

#### 4.4 Concluding Comments

A numerical parametric study of hypervelocity impact response using the HULL hydrodynamic computer code has revealed several interesting response characteristics of single- and double-bumper systems under cylindrical projectile impact. For single-bumper systems, long rod impacts were found to be more damaging than equal-weight spherical projectiles because the trailing end of the rods survived the initial bumper plate impacts relatively intact. The damage caused by compact rod impacts was similar to that caused by spherical projectile impacts. Thin disk impacts caused a relatively intact section of the bumper plate to rip away and impact the pressure wall. Finally, edge-on disk impacts, whether normal or oblique, were more damaging than straight-on impacts. In the case of long rod and thin disk impacts, double-bumper systems were found to offer more protection to the pressure wall against perforation than equal-weight single-bumper systems because the inner bumpers caused additional fragmentation of the debris cloud particles.

## 5.0 ACKNOWLEDGEMENTS

The author is grateful for support from NASA/Marshall Space Flight Center contract (NAS8-36955/D.O.74) with Miria Finckenor serving as Technical Monitor. The author would also like to express his appreciation to Roy Taylor, Hubert Smith, and Joe Lambert of the Laboratory Support Branch of the NASA/Marshall Space Flight Center Materials and Processes Laboratory, to Phillip Pettie and Robert Stowell of the Martin Marietta Corporation, and to Ben Ramsey, George Duncan, and Earl Shirley of the Boeing Corporation for conducting the impact testing that made this investigation possible. The author is grateful to John Tipton of the U.S. Army Corps of Engineers, Huntsville Division, for performing the HULL code runs that contributed to this investigation and to Jeffrey Peck for his assistance during the data analysis phase of this investigation.

## 6.0 REFERENCES

1. S.A. Finnegan, J.C. Schulz, and O.E.R. Heimdahl, "Spatial Fragment Mass and Velocity Distributions For Ordance and Ultra-Ordance Speed Impacts", Int. J. Impact Engng., Vol. 10, pp. 159-170 (1990).
2. D.E. Grady, and D.E. Passman, "Stability and fragmentation of Ejecta in Hypervelocity Impact", Int. J. Impact Engng., Vol. 10, pp. 197-212 (1990).
3. A.J. Piekutowski, "A Simple Dynamic Model for the Formation of Debris Clouds", Int. J. Impact Engng., Vol. 10, pp. 453-471 (1990).
4. A.J. Stilp, V. Hohler, E. Schneider, and K. Weber, "Debris Cloud Expansion Studies", Int. J. Impact Engng., Vol. 10, pp. 543-553 (1990).
5. K.S. Holian, "Hydrodynamics Code Calculations of Debris Clouds Produced by Ball-Plate Impacts", Int. J. Impact Engng., Vol. 10, pp. 231-239 (1990).
6. T.G. Trucano, D.E. Grady, and J.M. McGlaun, "Fragmentation Statistics from Eulerian Hydrocode Calculations", Int. J. Impact Engng., Vol. 10 pp. 587-660 (1990).
7. C.J. Maiden, J.W. Gehring, and A.R. McMillian, Investigation of Fundamental Mechanism of Damage to Thin Targets by Hypervelocity Projectiles, General Motors Defense Research Labratory, Report No. TR63-225, Santa Barbara, California, September (1963).
8. A.R. McMillian, Experimental Investigations of Simulated Meteoroid Damage to Various Spacecraft Structures, NASA CR-915, Washington, D.C. (1965).
9. J.F. Lundeberg, P.H. Stern, and J.R. Bristow, Meteoroid Protection for Spacecraft Structures, NASA TM-54201, Washington, D.C. (1965).
10. G.T. Burch, Multi-Plate Damage Study, Air Force Armament Laboratory, Report No. AFATL-TR-67-116, Eglin AFB, Florida (1967).
11. A.R. Coronado, M.N. Gibbins, M.A. Wright, and P.H. Stern, Space Station Integrated Wall Design and Penetration Damage Contol, Boeing Aerospace

- Company, Report No. D180-30550-4, Final Report, Contract NAS8-36426, Seattle, Washington (1987).
12. W.P. Schonberg, A.J. Bean, and K. Darzi, Hypervelocity Impact Physics, Final Report, Contract NAS8-36955/D.O.16, NASA CR-4343 (1991).
  13. C.E. Anderson, ed., Proceedings of the 1986 Symposium on Hypervelocity Impact, Int. J. Impact Engng., Vol. 5 (1987)
  14. C.E. Anderson, ed., Proceedings of the 1989 Symposium on Hypervelocity Impact, Int. J. Impact Engng., Vol. 10 (1990).
  15. C.E. Anderson, "An Overview of the Theory of Hydrocodes", Int. J. Impact Engng., Vol. 5, pp. 33-59 (1987)
  16. C.E. Anderson, "History and Application of Hydrocodes in Hypervelocity Impact", Int. J. Impact Engng., Vol. 5, pp. 423-439 (1987).
  17. R.A. Taylor, "A Space Debris Simulation Facility for Spacecraft Materials Evaluation", SAMPE Quarterly, Vol. 18, pp. 28-34 (1987).
  18. D.J. Kessler, R.C. Reynolds, and P.P. Anz-Meador, Orbital Debris Environment for Spacecraft Designed to Operate in Low Earth Orbit, NASA TM-100471, Houston, Texas (1988).
  19. R.K. Fujita, and G.E. Cort, "Comparison of Multidimensional Calculations of Long Rod Impacts on Oblique Plates", Computational Techniques for Contact, Impact, Penetration, and Perforation of Solids, L.E. Schwer, N.J. Salamon, and W.K. Liu, eds, ASME AMD Vol. 103, New York (1989).
  20. A.J. Stilp, and V. Hohler, "Hypervelocity Impact of Rod Projectiles with L/d from 1 to 32", Int. J. Impact Engng., Vol. 5, 331-373 (1987).
  21. D.A. Shockey, D.R. Curran, J.E. Osher, and H.H. Chau, "Disintegration Behavior of Metal Rods Subjected to Hypervelocity Impact", Int. J. Impact Engng., Vol. 5, 585-595 (1987).

22. D.J. Cagliostro, D.A. Mandell, L.A. Schwalbe, T.F. Adams, and E.J. Chapyak, "MESA 3-D Calculations of Armor Penetration by Projectiles with Combined Obliquity and Yaw", *Int. J. Impact Engng.*, Vol. 10, 81-92 (1990).
23. A.C. Charters, T.L. Menna, and A.J. Piekutowski, "Penetration Dynamics of Rods from Direct Ballistic Tests of Advanced Armor Components at 2-3 km/s", *Int. J. Impact Engng.*, Vol. 10, 93-106 (1990).
24. R.J. Morrison, A Preliminary Investigation of Projectile Shape Effects in Hypervelocity Impact Of Double Sheet Structure, NASA TN-D-6944, Washington, D.C. (1972).
25. W.P. Schonberg, and K. Darzi, "Projectile Shape and Material Effects in Hypervelocity Impact Response of Dual-wall Structures", *J. Aero. Engng.*, in press (1991).
26. J.S. Wilbeck, Impact Behavior of Low Strength Projectiles, Air Force Materials Laboratory, Report No. AFML-TR-77-134 (1978).

TABLE 1 Material Properties

Material Property	Projectile	Pressure Wall	Bumper
	1100-0	2219-T87	6061-T6
Ambient Density (gm/cm <sup>3</sup> )	2.71	2.80	2.71
Speed of Sound (km/sec)	5.38	5.38	5.38
Shock Velocity- Particle Velocity Slope	1.337	1.337	1.337
Initial Gruneisen Coefficient	2.10	2.10	2.10
Poisson's Ratio	0.33	0.33	0.33
Initial Yield Strength (x10 <sup>11</sup> dynes/cm <sup>2</sup> )	3.44738	3.79212	2.48211
Saturation Yield Strength (x10 <sup>11</sup> dynes/cm <sup>2</sup> )	8.96318	4.41264	2.89580
Plastic Strain at Saturation Yield Strength (Ultimate Failure Strain)	0.35	0.06	0.10
Ultimate Failure Stress (x10 <sup>10</sup> dynes/cm <sup>2</sup> )	1.00	1.16	1.16
Debye Temp. (°K)	375	375	375
Vapor Coefficient	0.1	0.1	0.1
Ambient Melt Energy per Unit Mass (x10 <sup>9</sup> ergs/gm)	7.30	7.30	7.30
Fusion Energy per Unit Mass (x10 <sup>9</sup> ergs/gm)	3.96	3.96	3.96
Ambient Vaporization Energy per Unit Mass (x10 <sup>9</sup> ergs/gm)	3.20	3.20	3.20
Sublimation Energy per Unit Mass (x10 <sup>9</sup> ergs/gm)	1.192	1.192	1.192
Ambient Energy per Unit Mass at Vaporization End (x10 <sup>11</sup> ergs/gm)	1.512	1.512	1.512

TABLE 2 Single-Bumper System Impact Parameters

Numerical Run No.	d (cm)	V (km/s)	$\theta$ (deg)	$t_s$ (mm)	$t_w$ (mm)	S (cm)
Numerical Simulations						
NR-14	1.000	6.00	0	1.6	3.175	10.16
NR-21	0.400	3.00	0	1.6	3.175	10.16
NR-22	0.400	4.00	0	1.6	3.175	10.16
NR-23	1.000	0.50	0	1.6	3.175	10.16
NR-24	0.500	6.00	0	1.6	3.175	10.16
NR-25	0.600	1.00	0	1.6	3.175	10.16
NR-26	0.625	6.00	0	1.6	3.175	10.16
NR-27	0.250	3.50	0	1.6	3.175	10.16
NR-28	0.500	1.50	0	1.6	3.175	10.16
NR-29	0.300	2.00	0	1.6	3.175	10.16
NR-30	0.400	5.00	0	1.6	3.175	10.16
NR-92	0.475	4.35	0	1.6	3.175	10.16
NR-94	0.635	6.90	0	1.6	3.175	10.16
Experimental Tests						
EHSS2B	0.635	5.88	0	1.6	3.175	10.16
P05	0.635	6.90	0	1.6	3.175	10.16
P27	0.475	4.53	0	1.6	3.175	10.16
P27A	0.475	3.87	0	1.6	3.175	10.16
P27B	0.475	4.15	0	1.6	3.175	10.16
PT4B	0.635	4.25	0	1.6	3.175	10.16



TABLE 3 Double-Bumper System Impact Parameters

Numerical Run No.	d (cm)	V (km/s)	$\theta$ (deg)	$t_{s1}$ (mm)	$t_{s2}$ (mm)	$t_w$ (mm)	$s_1$ (cm)	$s_2$ (cm)
Numerical Simulations								
NR-1	0.635	4.40	0	0.8	0.8	3.175	2.54	7.62
NR-2	0.635	3.82	0	0.8	0.8	3.175	2.54	7.62
NR-3	0.635	4.09	0	0.8	0.8	3.175	5.08	5.08
NR-4	0.635	4.34	0	0.8	0.8	3.175	5.08	5.08
NR-5	0.635	4.40	0	0.8	0.8	3.175	7.62	2.54
NR-6	0.635	4.97	0	0.8	0.8	3.175	7.62	2.54
NR-15	1.000	6.00	0	0.8	0.8	3.175	2.54	7.62
NR-31	0.700	7.00	0	0.8	0.8	3.175	2.54	7.62
NR-32	0.500	2.00	0	0.8	0.8	3.175	2.54	7.62
NR-33	0.400	3.00	0	0.8	0.8	3.175	2.54	7.62
NR-34	0.350	3.50	0	0.8	0.8	3.175	2.54	7.62
Experimental Tests								
115-1	0.635	4.40	0	0.8	0.8	3.175	2.54	7.62
115-3	0.635	3.82	0	0.8	0.8	3.175	2.54	7.62
116-2	0.475	2.57	0	0.8	0.8	3.175	2.54	7.62
117-1	0.635	4.09	0	0.8	0.8	3.175	5.08	5.08
117-2	0.635	4.17	0	0.8	0.8	3.175	5.08	5.08
118-1	0.635	4.40	0	0.8	0.8	3.175	7.62	2.54
118-3	0.635	4.52	0	0.8	0.8	3.175	7.62	2.54
130C	0.762	5.25	0	0.8	0.8	3.175	2.54	7.62

TABLE 4 Comparison of Numerical and Experimental Results,  
Single-Bumper Systems

Test No.	Test Type	Energy (J)	Pressure Wall Perforated?	D (cm)	$d_h$ (cm)	$A_d$ (cm <sup>2</sup> )	$\gamma$ (deg)	$A_s$ (cm <sup>2</sup> )
NR-30	num.	1,136	N	0.86	----	3.0	12.5	----
P27A	exp.	1,140	Y	0.86	0.44	21.7	29.0	----
NR-92	num.	1,440	Y	1.04	0.35	23.1	31.5	----
P27	exp.	1,562	N	1.07	----	45.6	41.0	----
NR-92	num.	1,440	Y	1.04	0.35	23.1	31.5	----
P27B	exp.	1,311	Y	1.00	0.30	31.7	34.5	----
NR-24	num.	3,196	N	1.01	----	40.9	41.0	----
PT4B	exp.	3,285	Y	1.27	0.64	98.1	57.5	2.58
NR-26	num.	6,242	N	1.29	----	18.4	28.0	----
EHSS2B	exp.	6,287	N	1.22	----	62.1	47.5	5.23
NR-94	num.	8,657	N	1.39	----	48.4	44.5	----
P05	exp.	8,657	Y	1.42	0.47	91.5	56.0	0.19
NR-14	num.	25,566	Y	1.72	3.02	32.8	37.0	----
NR-21	num.	409	Y	0.65	3.23	2.6	11.0	----
NR-22	num.	727	Y	0.75	0.38	2.0	9.5	----
NR-23	num.	177	N	0.80	----	75.4	54.5	----
NR-25	num.	153	N	0.65	----	77.1	55.5	----
NR-27	num.	136	N	0.43	----	3.9	7.0	----
NR-28	num.	199	Y	0.59	0.43	12.1	11.0	----
NR-29	num.	77	N	0.38	----	12.5	13.5	----

TABLE 5 Comparison of Numerical and Experimental Results,  
Double-Bumper Systems

Test No.	Test Type	S <sub>1</sub> (cm)	S <sub>2</sub> (cm)	Energy (J)	Pressure Wall Perforated?	D1 (cm)	D2 (cm)	d <sub>h</sub> (cm)	A <sub>d</sub> (cm <sup>2</sup> )
NR-33	num.	2.54	7.62	409	Y	0.65	0.65	0.43	3.3
116-2	exp.	2.54	7.62	503	Y	0.66	0.89	crack	1.9
NR-2	num.	2.54	7.62	2,653	Y	1.08	1.23	0.76	29.6
115-3	exp.	2.54	7.62	2,653	Y	0.91	1.95	0.49	38.3
NR-1	num.	2.54	7.62	3,520	N	1.13	1.18	----	21.2
115-1	exp.	2.54	7.62	3,520	N	0.97	2.58	----	38.1
NR-31	num.	2.54	7.62	11,936	Y	1.19	2.80	0.43 <sup>1</sup>	23.7
130C	exp.	2.54	7.62	8,826	Y	1.12	3.46	0.36 <sup>2</sup>	34.8
NR-3	num.	5.08	5.08	3,042	Y	1.08	1.29	1.34	7.1
117-1	exp.	5.08	5.08	3,042	Y	0.97	3.80	crack	13.2
NR-4	num.	5.08	5.08	3,425	Y	1.08	1.08	2.08	13.9
117-2	exp.	5.08	5.08	3,425	Y	0.92	2.70	0.10 <sup>3</sup>	14.3
NR-5	num.	7.62	2.54	3,520	Y	1.08	0.97	1.19	11.2
118-1	exp.	7.62	2.54	3,520	Y	0.96	3.68	0.37	6.5
NR-6	num.	7.62	2.54	4,492	Y	1.08	1.02	1.19	12.5
118-3	exp.	7.62	2.54	3,715	Y	1.01	3.83	crack	7.0
NR-15	num.	2.54	7.62	25,566	Y	1.72	2.80	3.02	36.2
NR-32	num.	2.54	7.62	355	Y	0.75	0.75	0.65	8.2
NR-34	num.	2.54	7.62	373	N	0.65	0.65	----	1.8

<sup>1</sup>Single hole

<sup>2</sup>Double hole

<sup>3</sup>Pin-hole

TABLE 6 Numerical Impact Simulation Parameters for Parametric Study

Numerical Run No.	d (cm)	L/D	V (km/s)	$\theta$ (deg)	$\phi$ (deg)	$\psi$ (deg)	$t_{s1}$ (mm)	$t_{s2}$ (mm)	$t_w$ (mm)	$S_1$ (cm)	$S_2$ (cm)
Single-Bumper Systems, Spherical Projectiles											
NR-24	0.500	----	6.0	0	----	----	1.6	----	3.175	10.16	----
NR-67	0.890	----	10.5	0	----	----	1.6	----	3.175	11.25	----
Single-Bumper Systems, Cylindrical Projectiles											
NR-38	0.350	2.00	6.0	0	0	0	1.6	----	3.175	10.16	----
NR-42	0.913	0.11	6.0	0	0	0	1.6	----	3.175	10.16	----
NR-43	1.440	0.0277	6.0	0	0	0	1.6	----	3.175	10.16	----
NR-44	0.437	1.00	6.0	0	0	0	1.6	----	3.175	10.16	----
NR-45	0.635	0.31	6.0	0	0	0	1.6	----	3.175	10.16	----
NR-46	0.913	0.11	6.0	60	0	90	1.6	----	3.175	10.16	----
NR-48	0.913	0.11	6.0	0	0	90	1.6	----	3.175	10.16	----
NR-49	0.913	0.11	6.0	0	60	0	1.6	----	3.175	10.16	----
NR-66	0.519	3.00	10.5	0	0	0	1.6	----	3.175	11.25	----
NR-68	0.606	2.00	10.5	0	0	0	1.6	----	3.175	11.25	----
Double-Bumper Systems, Cylindrical Projectiles											
NR-39	0.350	2.00	6.0	0	0	0	0.8	0.8	3.175	2.54	7.62
NR-47	1.440	0.0277	6.0	0	0	0	0.8	0.8	3.175	2.54	7.62

TABLE 7 Comparison of Numerical Spherical and Cylindrical Projectile Impact Test Results, Single-Bumper Systems,  $\theta=\phi=\psi=0^\circ$

Numerical Run No.	L/D	Energy (kJ)	Pressure Wall Perforated?	D (cm)	$d_h$ (cm)	$A_d$ (cm <sup>2</sup> )	$\gamma$ (deg)
NR-67	Sphere	55.197	N	1.8	----	20.2	22.5
NR-66	3.0	49.255	Y	1.4	1.3	28.3	26.5
NR-68	2.0	52.273	Y	1.4	1.4	11.4	17.0
NR-24	Sphere	3.196	N	1.0	----	40.9	41.0
NR-38	2.0	3.196	Y	1.0	0.9	11.8	11.5
NR-44	1.0	3.200	N	1.1	----	32.8	37.0
NR-45	0.31	3.196	N	1.3	----	----	----

TABLE 8 Effect of Cylindrical Projectile L/D Ratio on Single-Bumper System Response,  $\theta=\phi=\psi=0^\circ$

Numerical Run No.	L/D	Energy (kJ)	Pressure Wall Perforated?	D (cm)	$d_h$ (cm)	$A_d$ (cm <sup>2</sup> )	$\gamma$ (deg)
NR-38	2.0	3.196	Y	1.0	0.9	3.0	11.5
NR-44	1.0	3.200	N	1.1	----	32.8	37.0
NR-45	0.31	3.196	N	1.3	----	----	----
NR-42	0.11	3.210	Y	1.5	0.4	11.8	22.5
NR-43	0.0277	3.172	Y	1.8	(1)	19.3	29.0

(1) Severe necking of pressure wall plate near debris cloud impact site.

TABLE 9 Effect of Cylindrical Projectile Orientation on  
Single-Bumper System Response

Numerical Run No.	L/D	$\theta$ (deg)	$\phi$ (deg)	$\psi$ (deg)	Energy (kJ)	Pressure Wall Perforated?	D (cm)	$d_h$ (cm)	$A_{d2}$ (cm <sup>2</sup> )	$\gamma$ (deg)
NR-42	0.11	0	0	0	3.210	Y	1.5	0.4	11.8	22.5
NR-46	0.11	60	0	90	3.210	Y	1.8	1.4	14.6	17.5
NR-48	0.11	0	0	90	3.210	Y	1.4	1.2	25.6	33.0
NR-49	0.11	0	60	0	3.210	N	1.3	---	30.6	35.0

TABLE 10 Comparison of Numerical Single- and Double-Bumper  
Test Results, Cylindrical Projectiles,  $\theta=\phi=\psi=0^\circ$

Numerical Run No. (cm <sup>2</sup> )	L/D	$S_1$ (cm)	$S_2$ (cm)	Energy (kJ)	Pressure Wall Perforated?	D1 (cm)	D2 (cm)	$d_h$ (cm)	$A_d$
NR-39	2.0	2.54	7.62	3.196	N	0.8	1.3	----	25.6
NR-38	2.0	10.16	----	3.196	Y	1.0	----	0.9	3.0
NR-47	0.0277	2.54	7.62	3.206	N	2.0	4.3	----	11.8
NR-43	0.0277	10.16	----	3.172	N	1.8	----	----	19.3

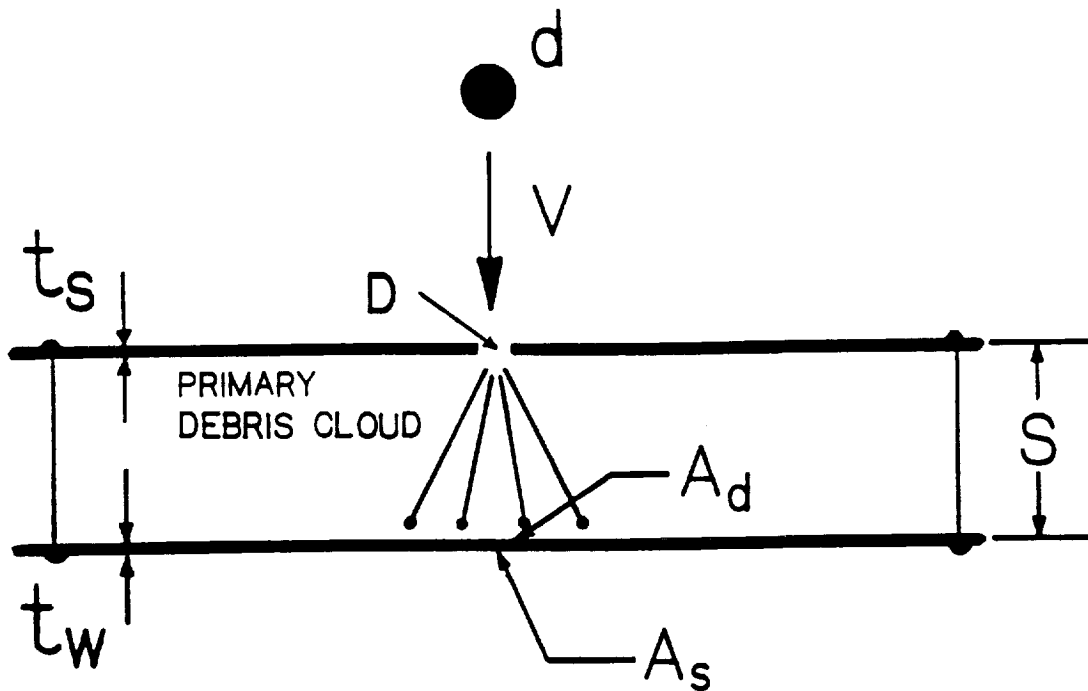


Figure 1. Normal Impact of a Single-Bumper Structure.

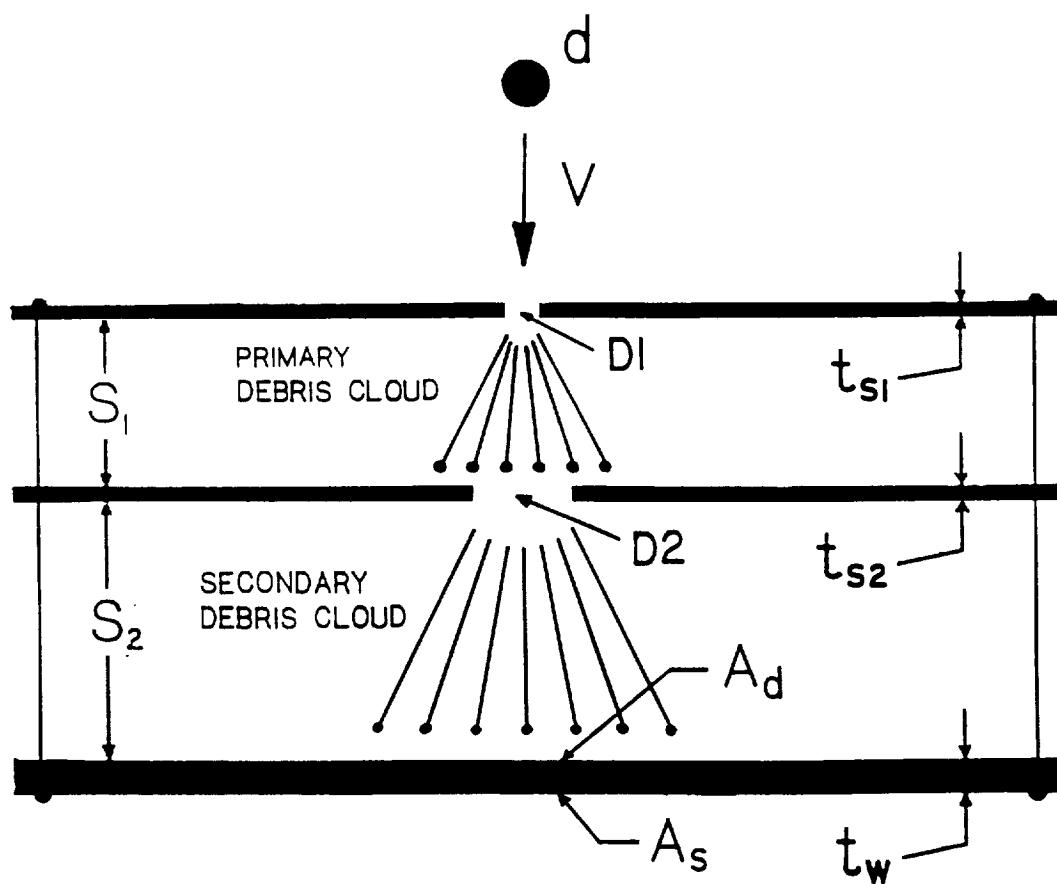


Figure 2. Normal Impact of a Double-Bumper Structure.

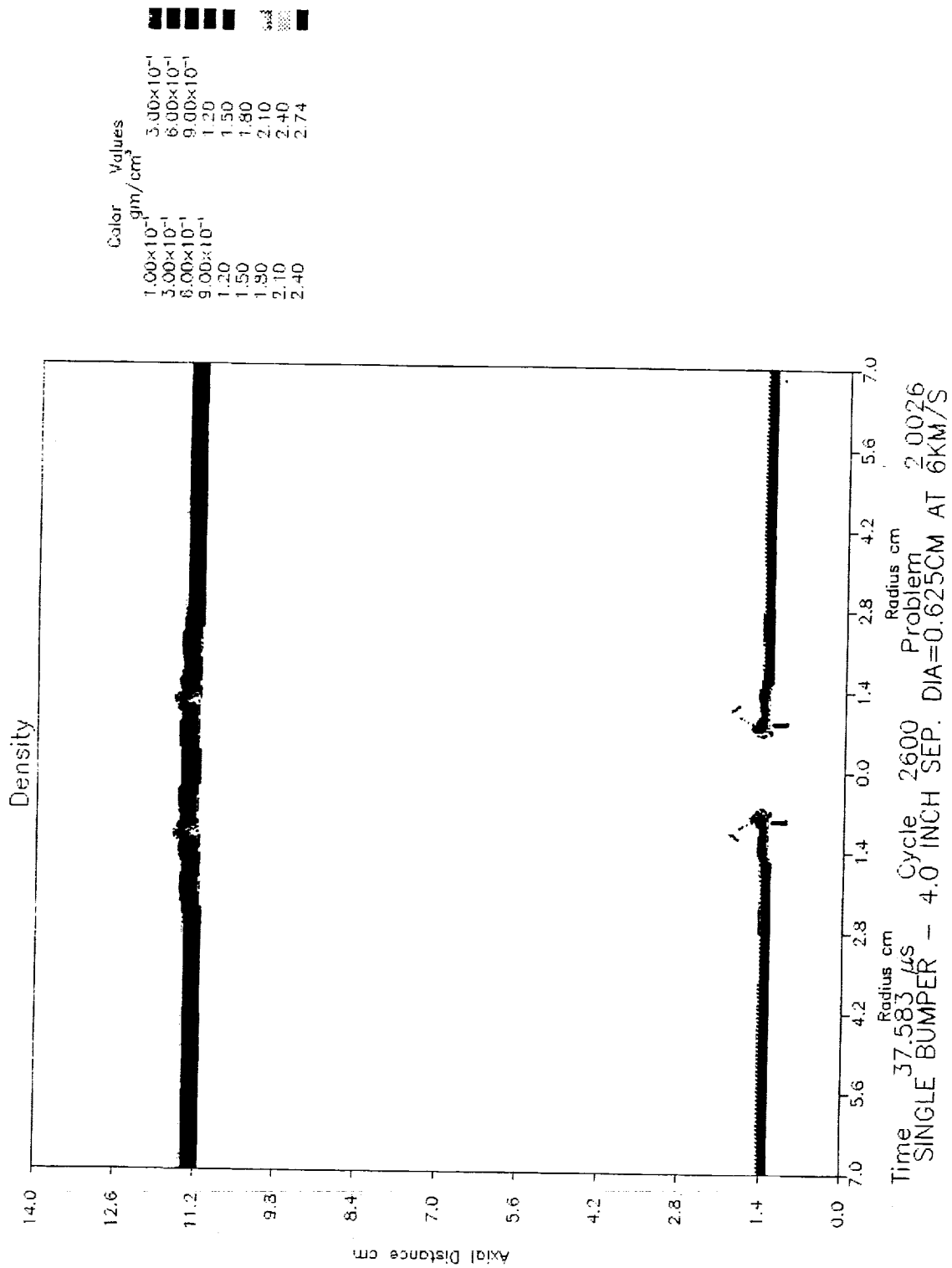


Figure 3. Final Output Frame, HULL Code Impact Simulation NR-26.



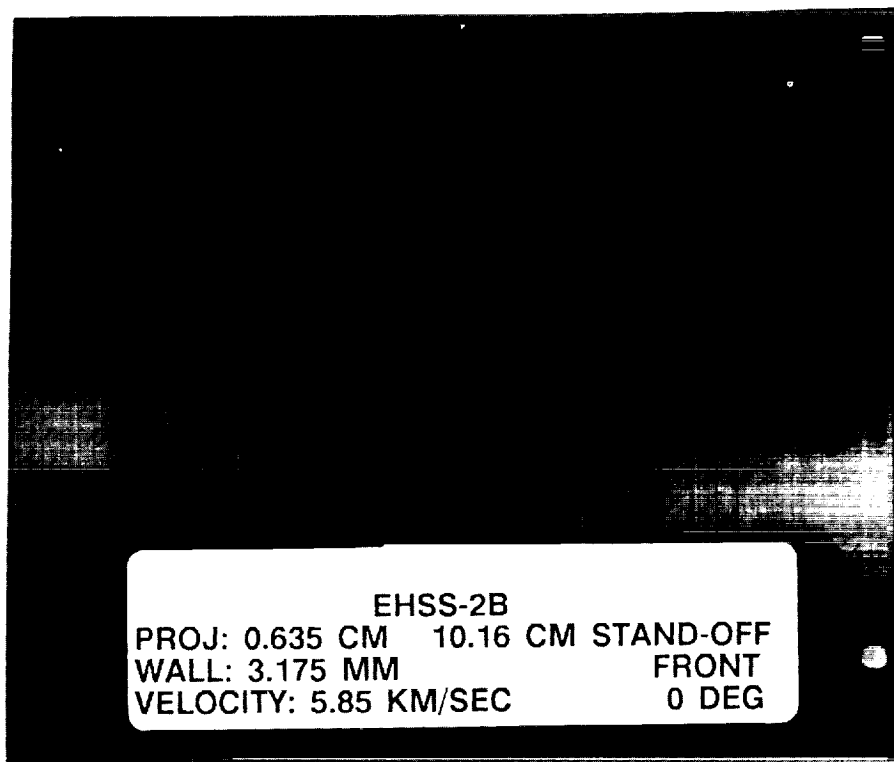


Figure 4a. Pressure Wall Plate, Experimental Test No. EHSS-2B (Front).

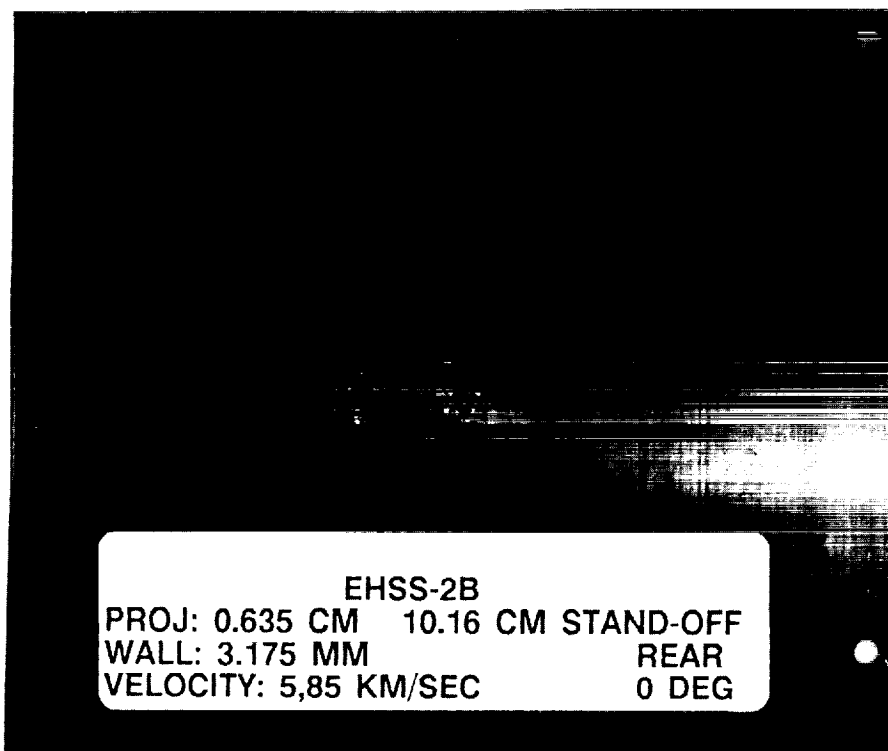


Figure 4b. Pressure Wall Plate, Experimental Test No. EHSS-2B (Rear).

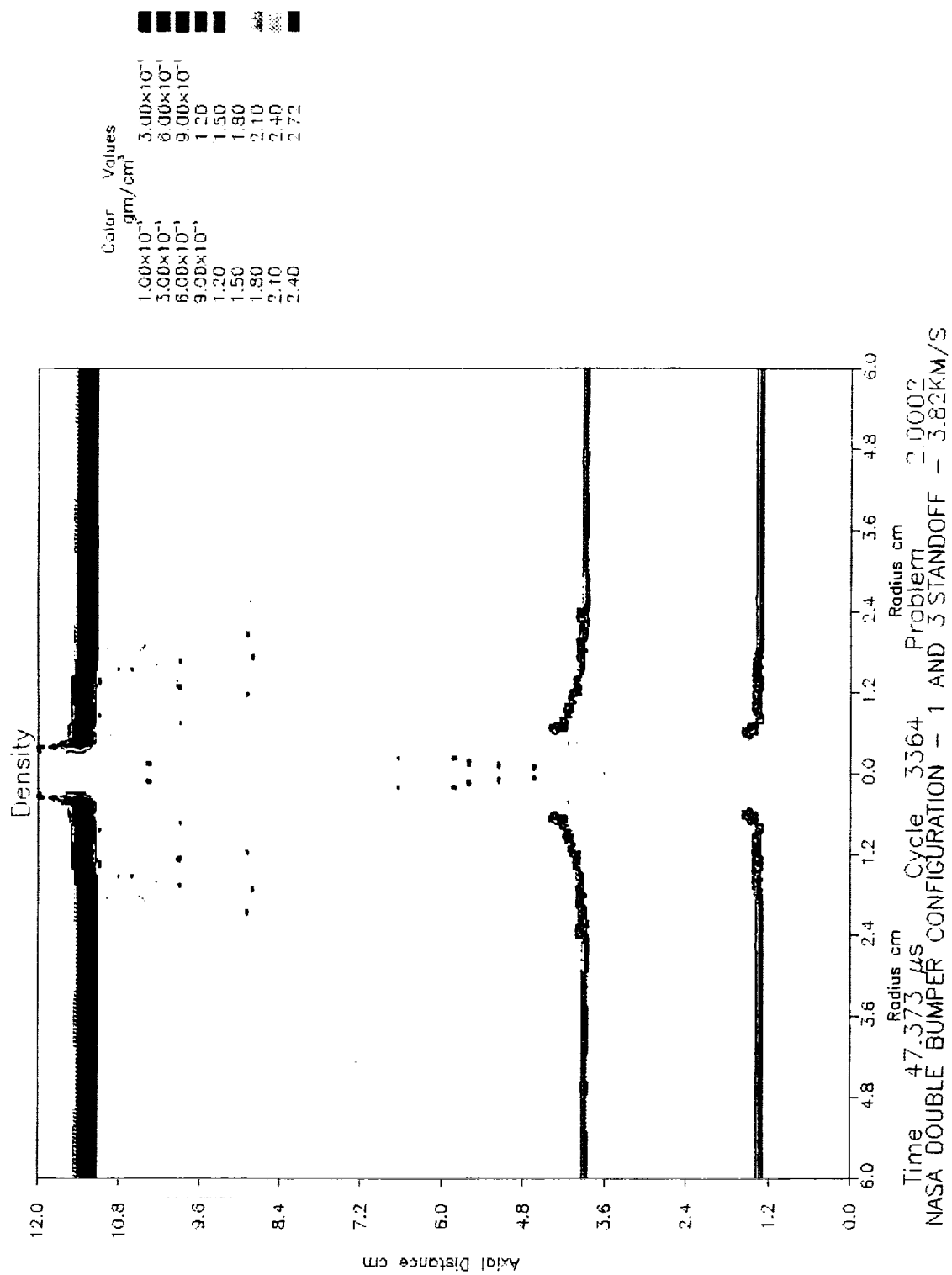
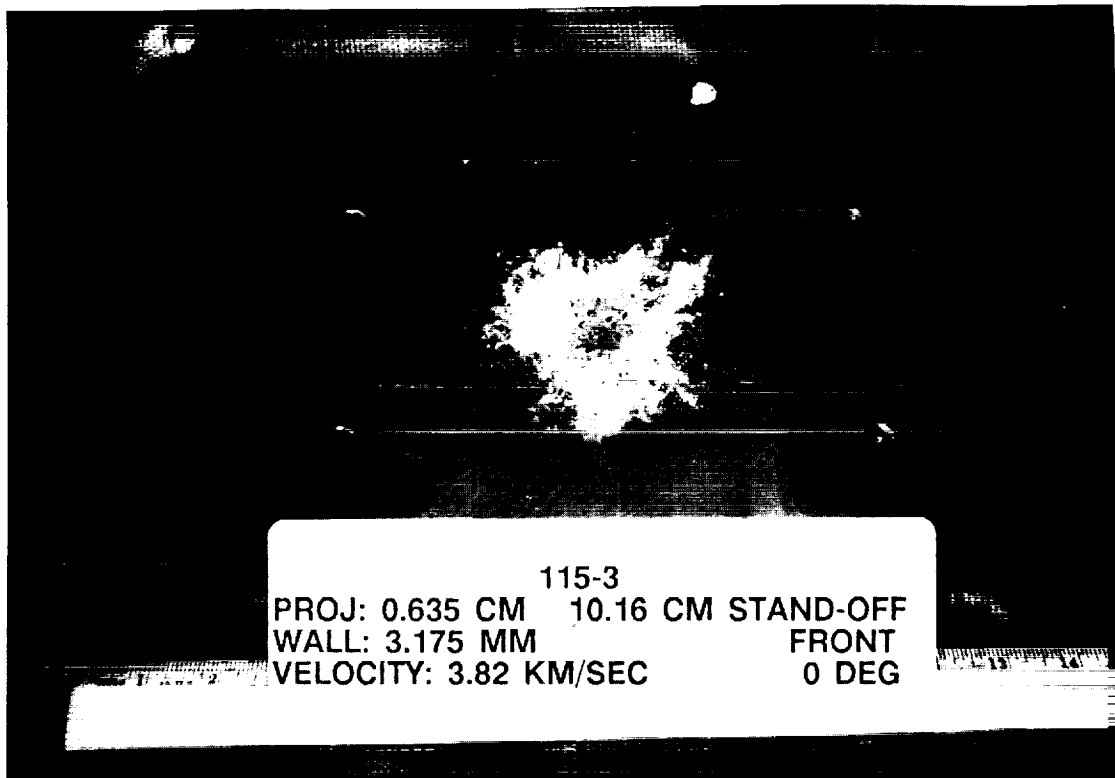
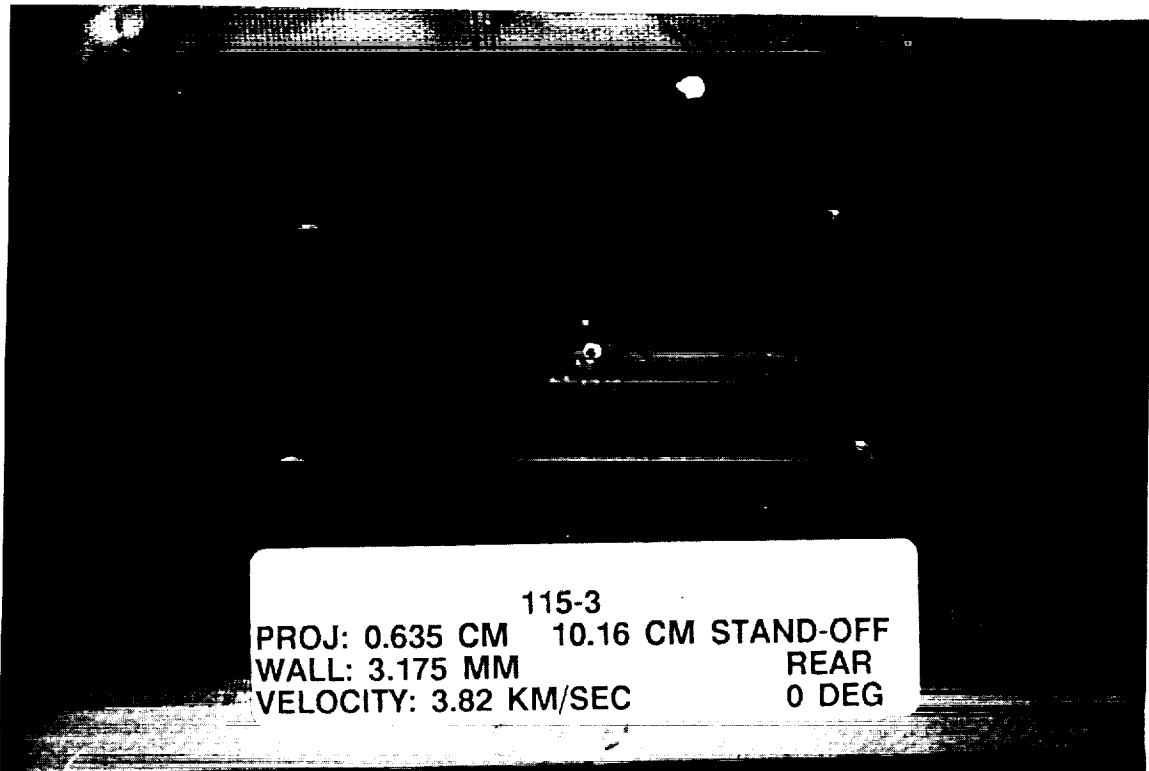


Figure 5. Final Output Frame, HULL Code Impact Simulation NR-2.



115-3  
PROJ: 0.635 CM 10.16 CM STAND-OFF  
WALL: 3.175 MM FRONT  
VELOCITY: 3.82 KM/SEC 0 DEG

Figure 6a. Pressure Wall Plate, Experimental Test No. 115-3 (Front).



115-3  
PROJ: 0.635 CM 10.16 CM STAND-OFF  
WALL: 3.175 MM REAR  
VELOCITY: 3.82 KM/SEC 0 DEG

Figure 6b. Pressure Wall Plate, Experimental Test No. 115-3 (Rear).

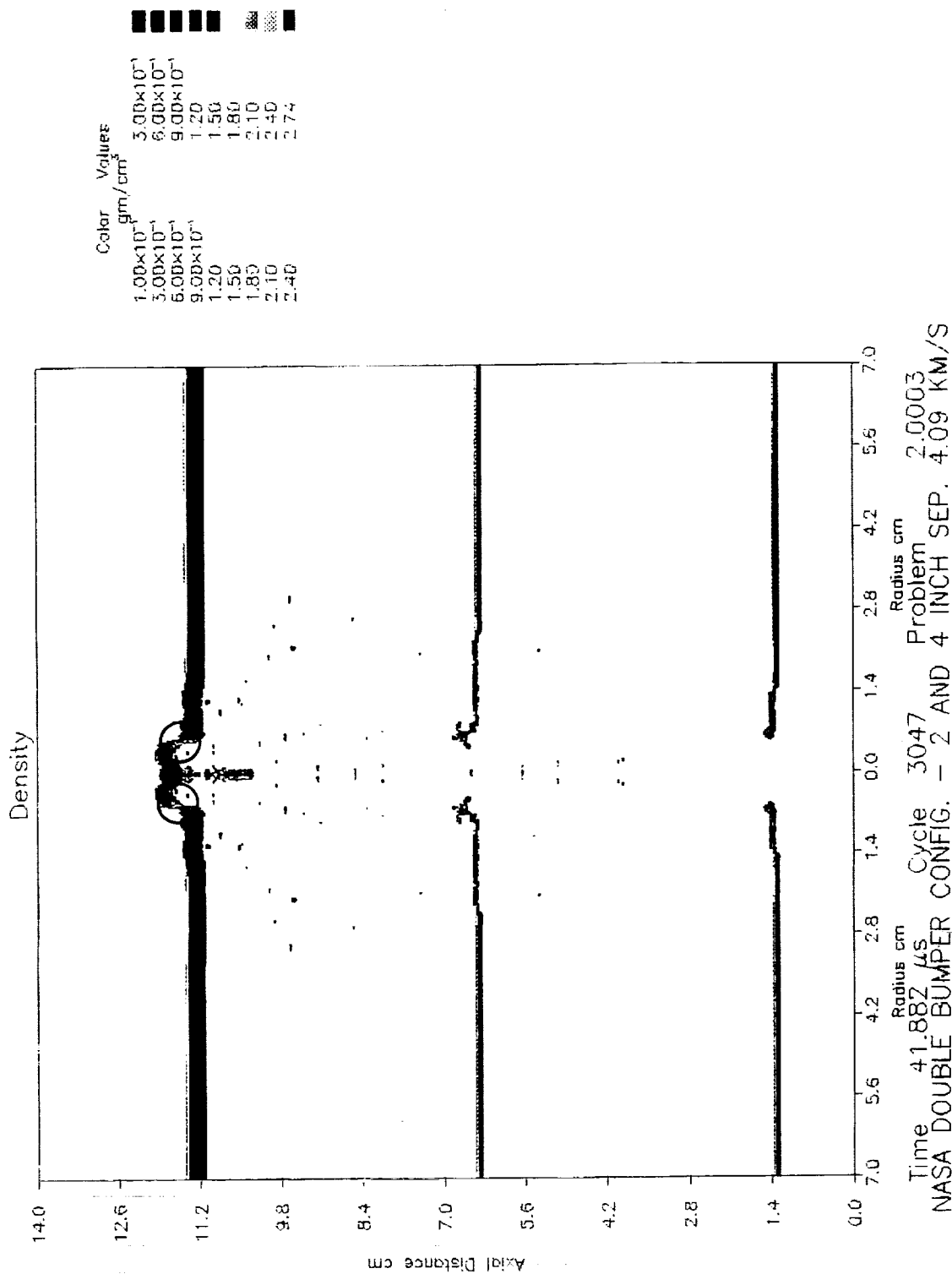


Figure 7. Final Output Frame, HULL Code Impact Simulation NR-3.

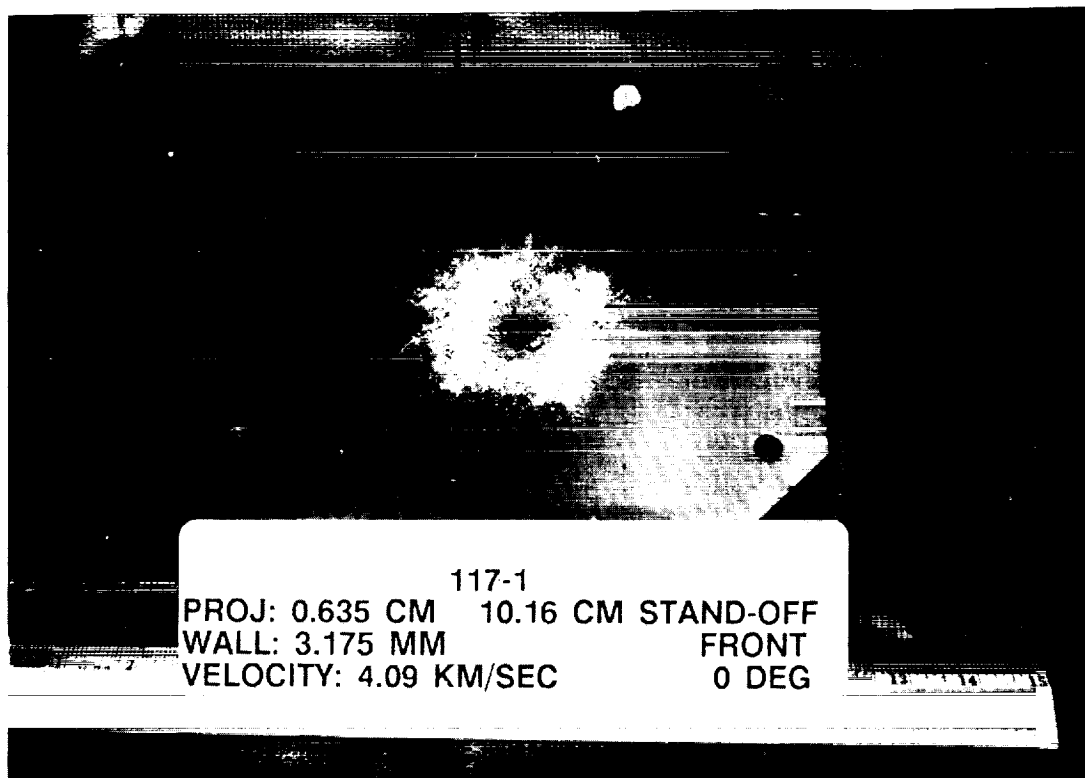


Figure 8a. Pressure Wall Plate, Experimental Test No. 117-1 (Front).

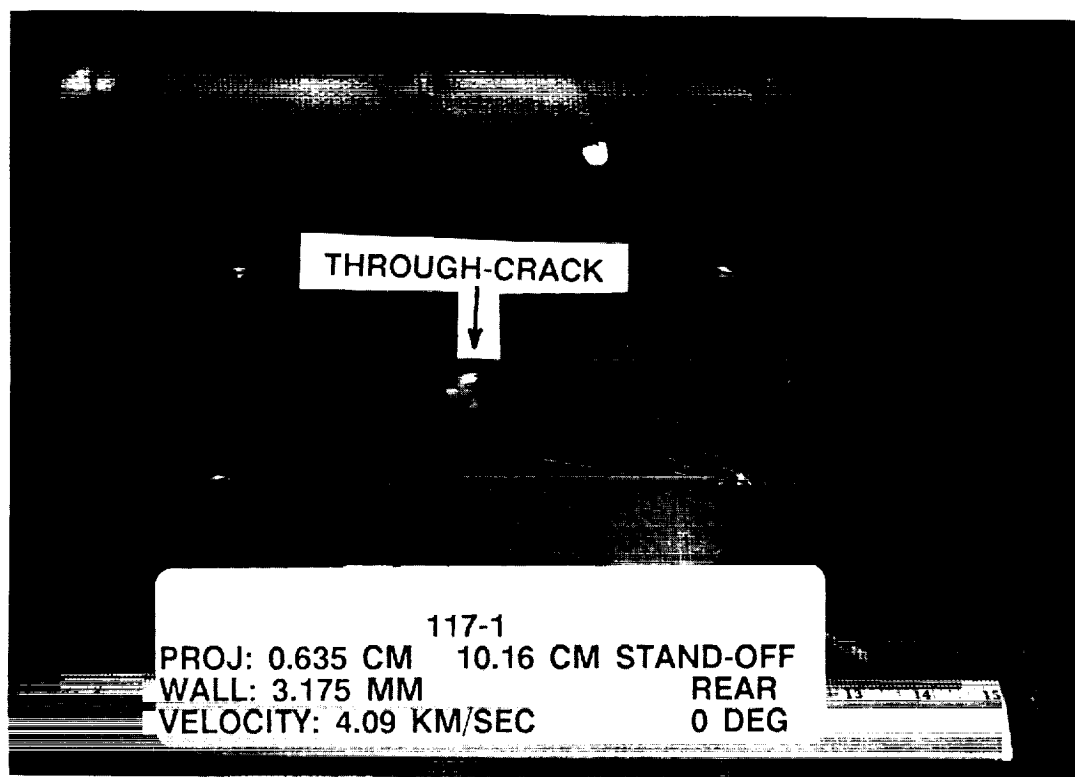


Figure 8b. Pressure Wall Plate, Experimental Test No. 117-1 (Rear).

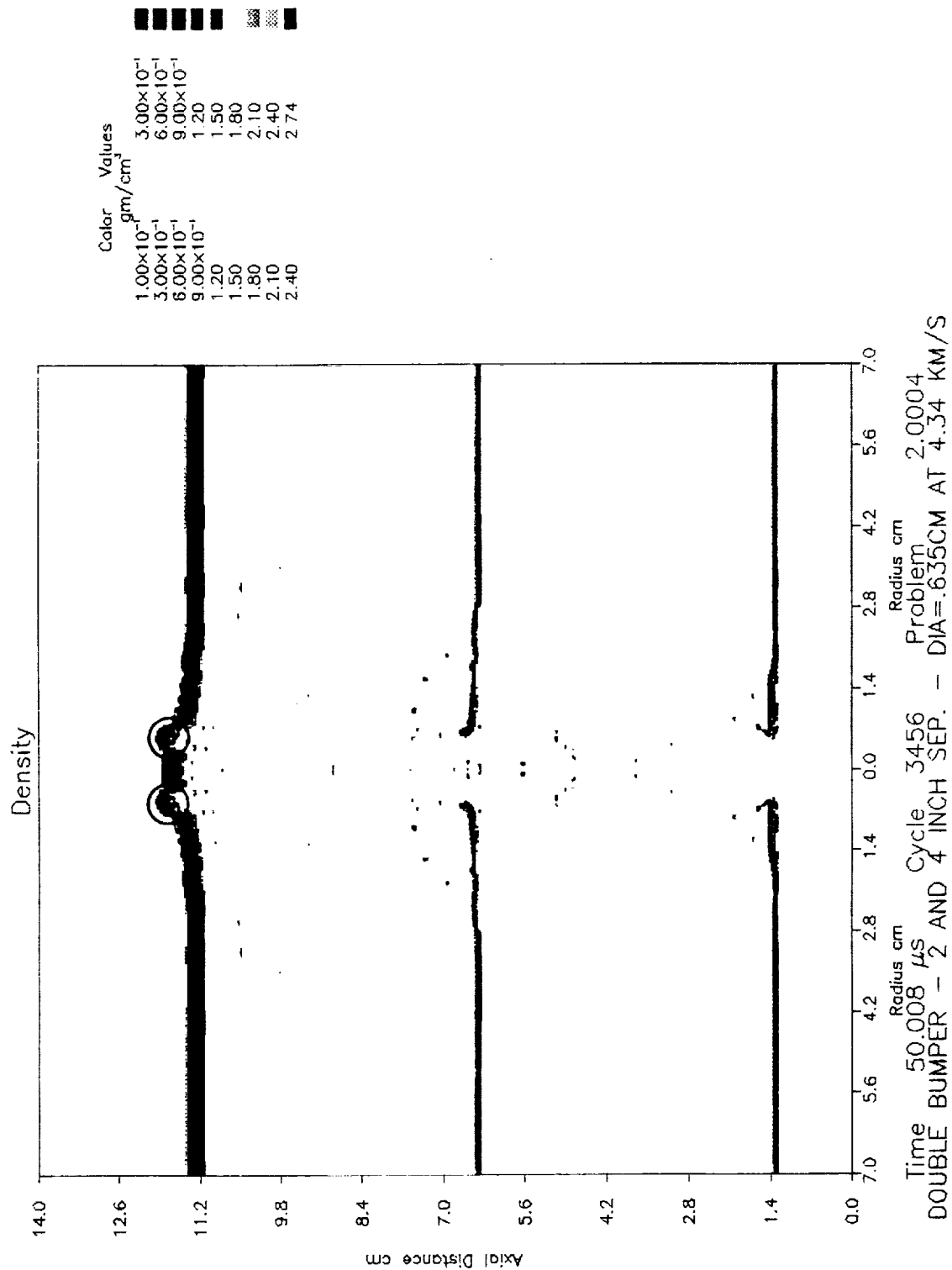


Figure 9. Final Output Frame, HULL Code Impact Simulation NR-4.

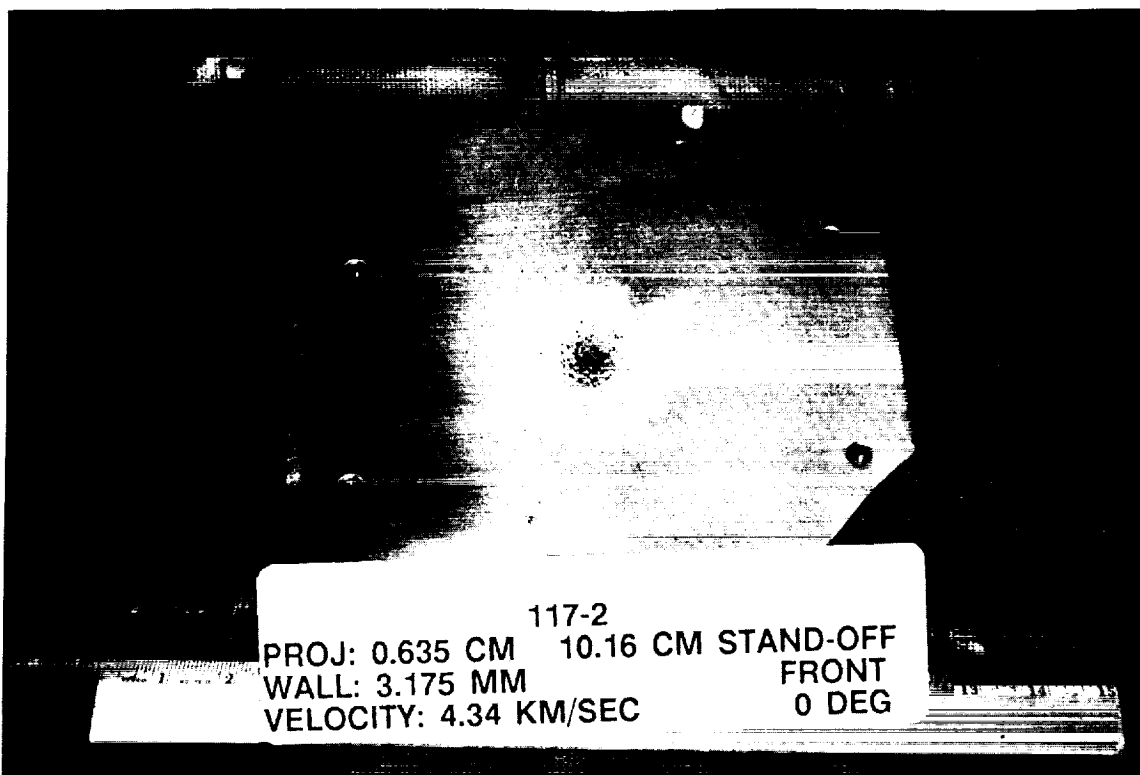


Figure 10a. Pressure Wall Plate, Experimental Test No. 117-2 (Front).

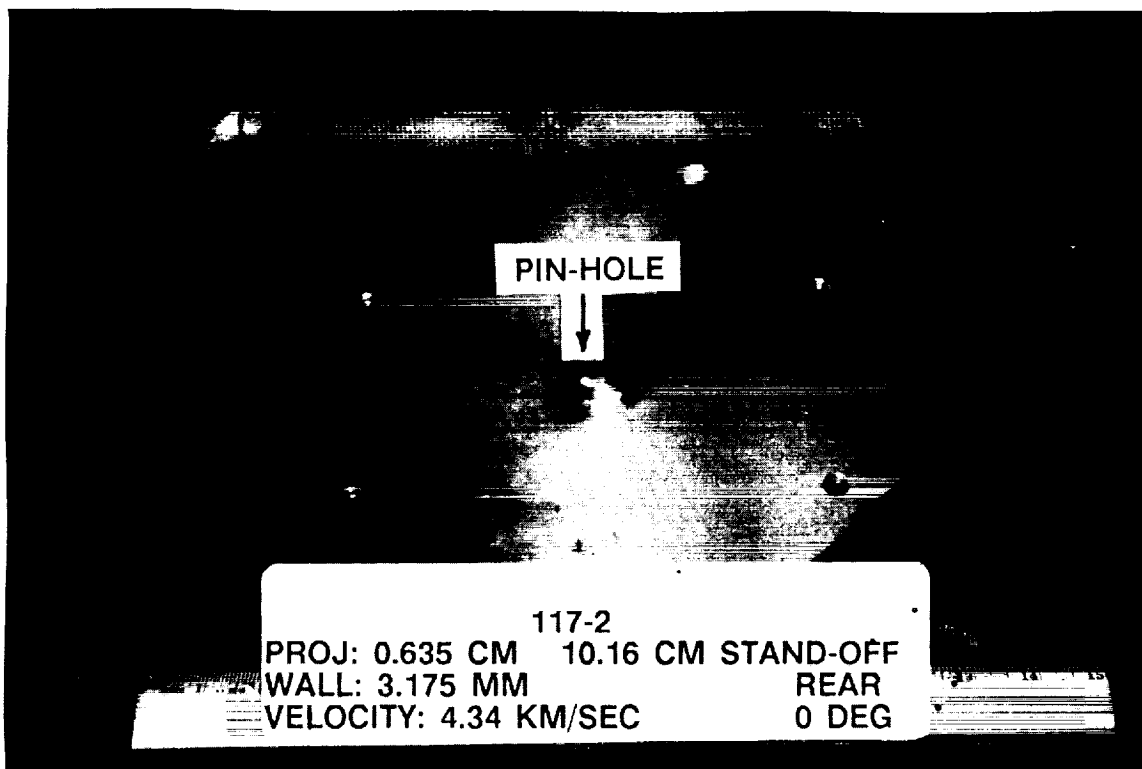


Figure 10b. Pressure Wall Plate, Experimental Test No. 117-2 (Rear).

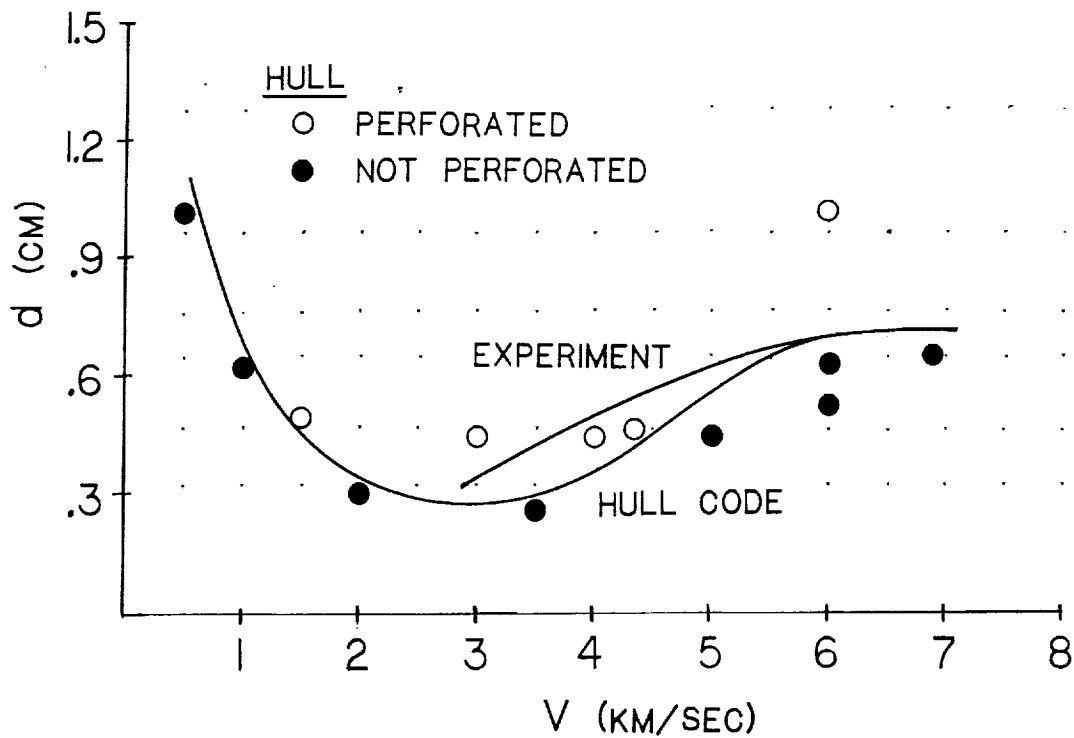


Figure 11. Ballistic Limit Curve, Single-Bumper System, Normal Impact  
 $t_s = 1.6$  mm,  $t_w = 3.175$  mm,  $S = 10.16$  cm.

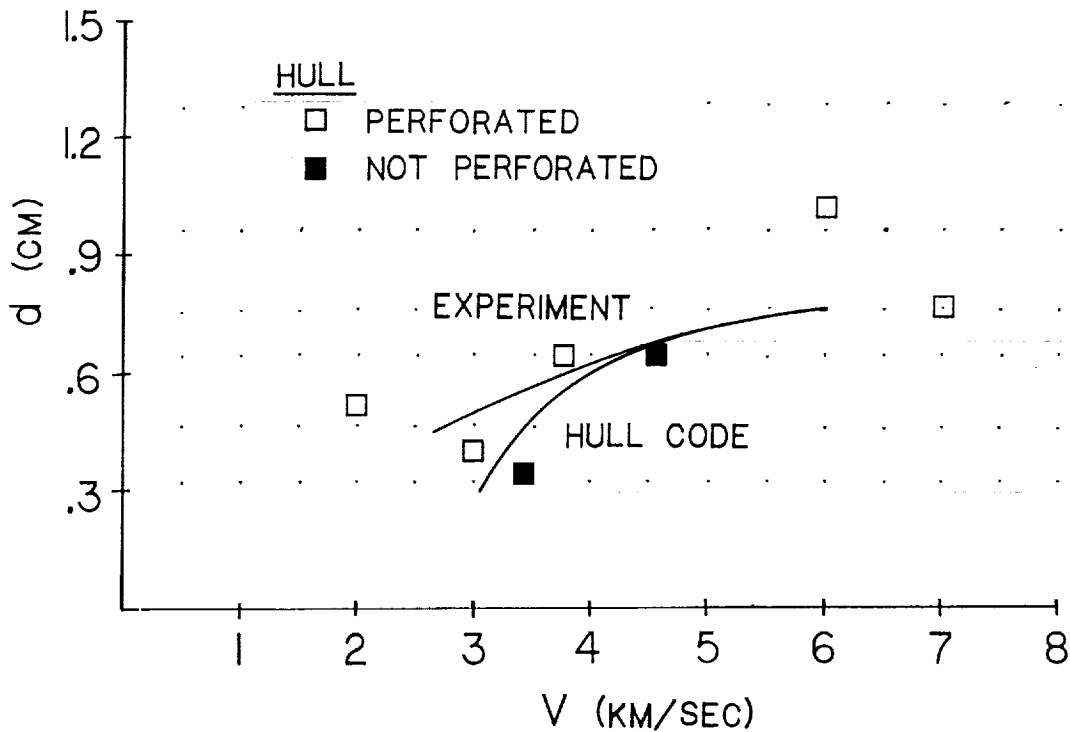


Figure 12. Ballistic Limit Curve, Double-Bumper System, Normal Impact  
 $t_{s1} = t_{s2} = 0.8$  mm,  $t_w = 3.175$  mm,  $S_1 = 2.54$  cm,  $S_2 = 7.62$  cm.



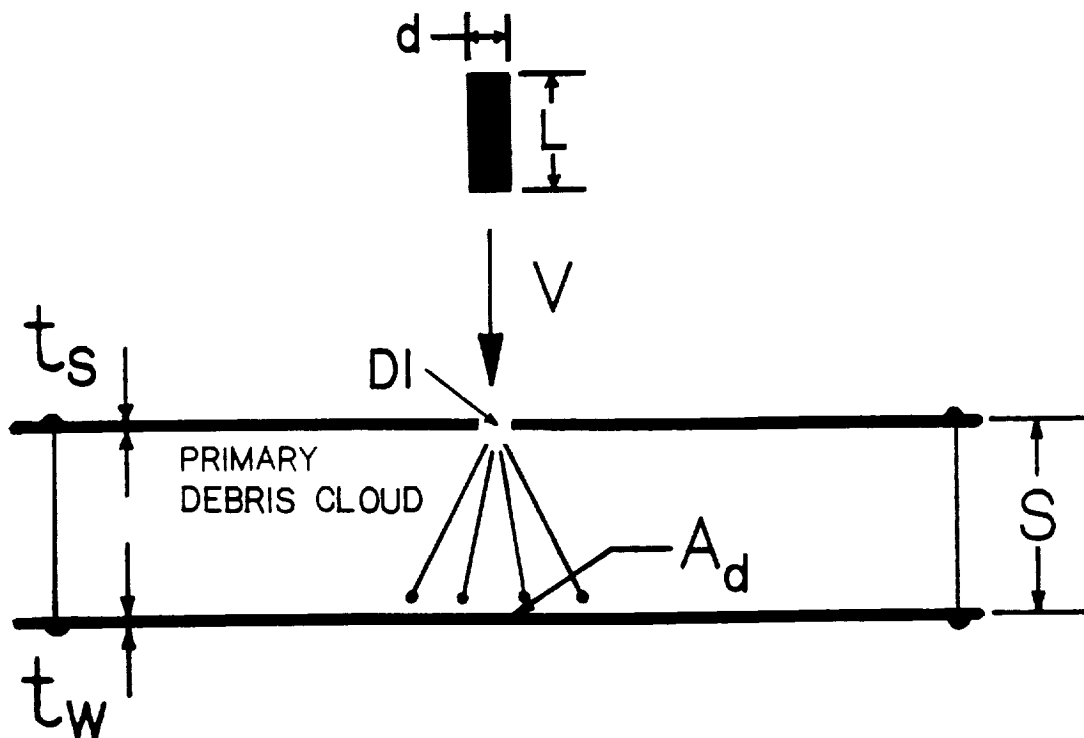


Figure 13. Normal Unyawed Cylindrical Projectile Impact of a Single-Bumper Structure.

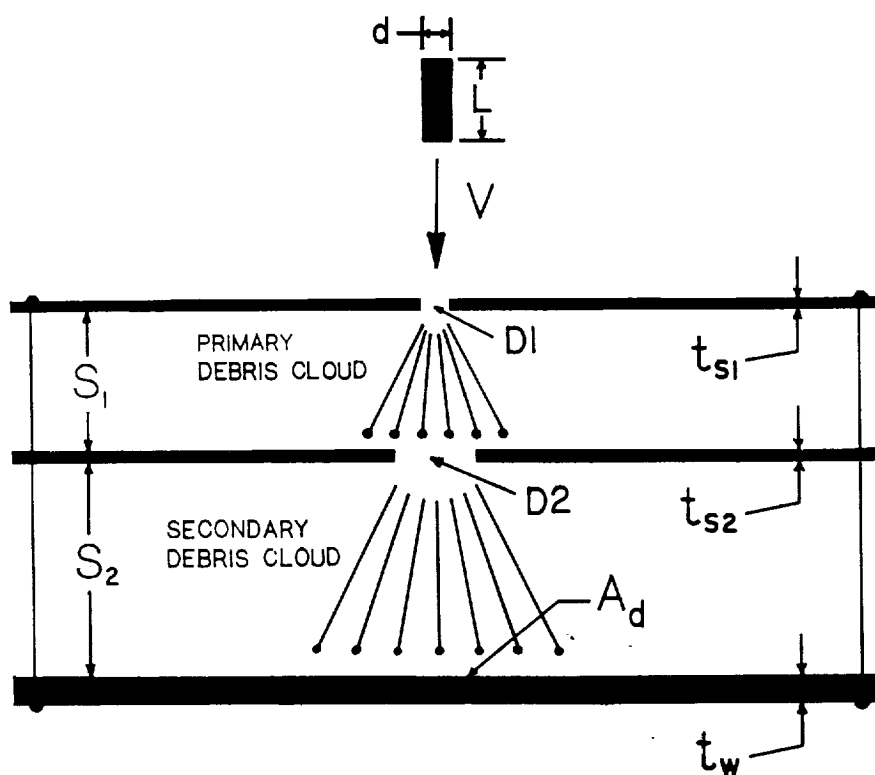


Figure 14. Normal Unyawed Cylindrical Projectile Impact of a Double-Bumper Structure.

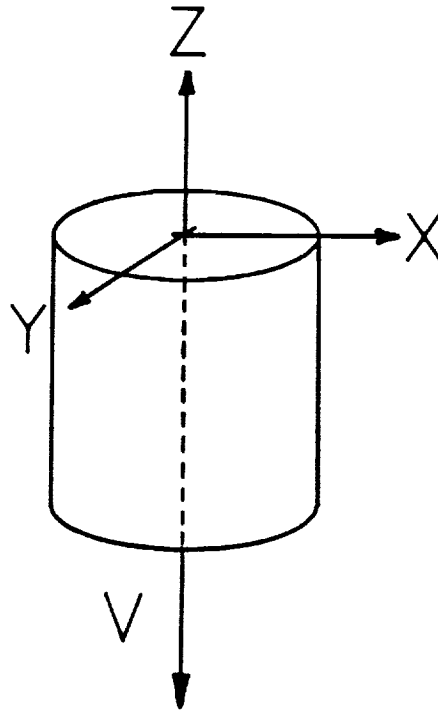


Figure 15. Coordinate System for Yaw Angle Definitions.

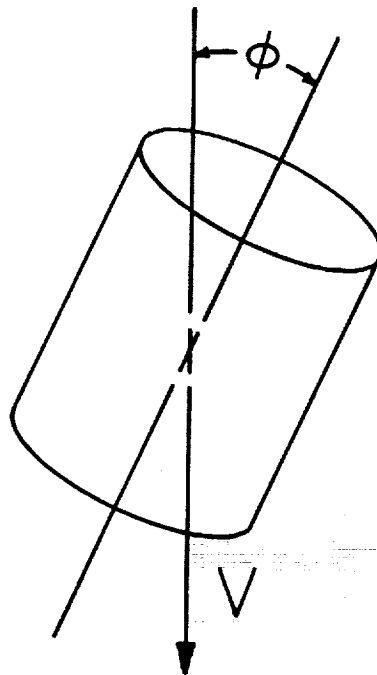


Figure 16. Example of Yawed Trajectory in the x-z Plane.

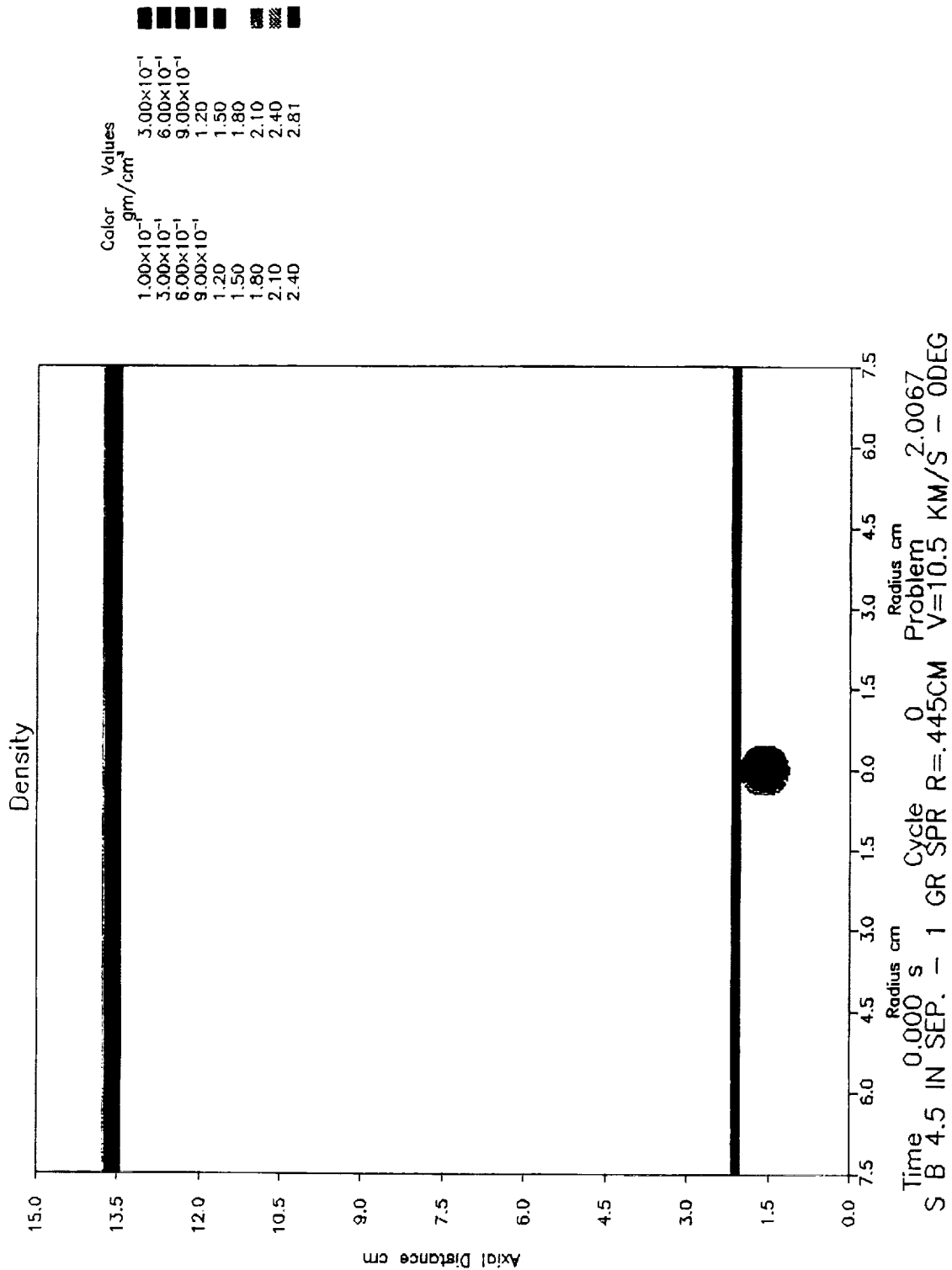


Figure 17a. HULL Code Impact Simulation NR-67-Spherical Projectile,  
t = 0.000  $\mu$  s.

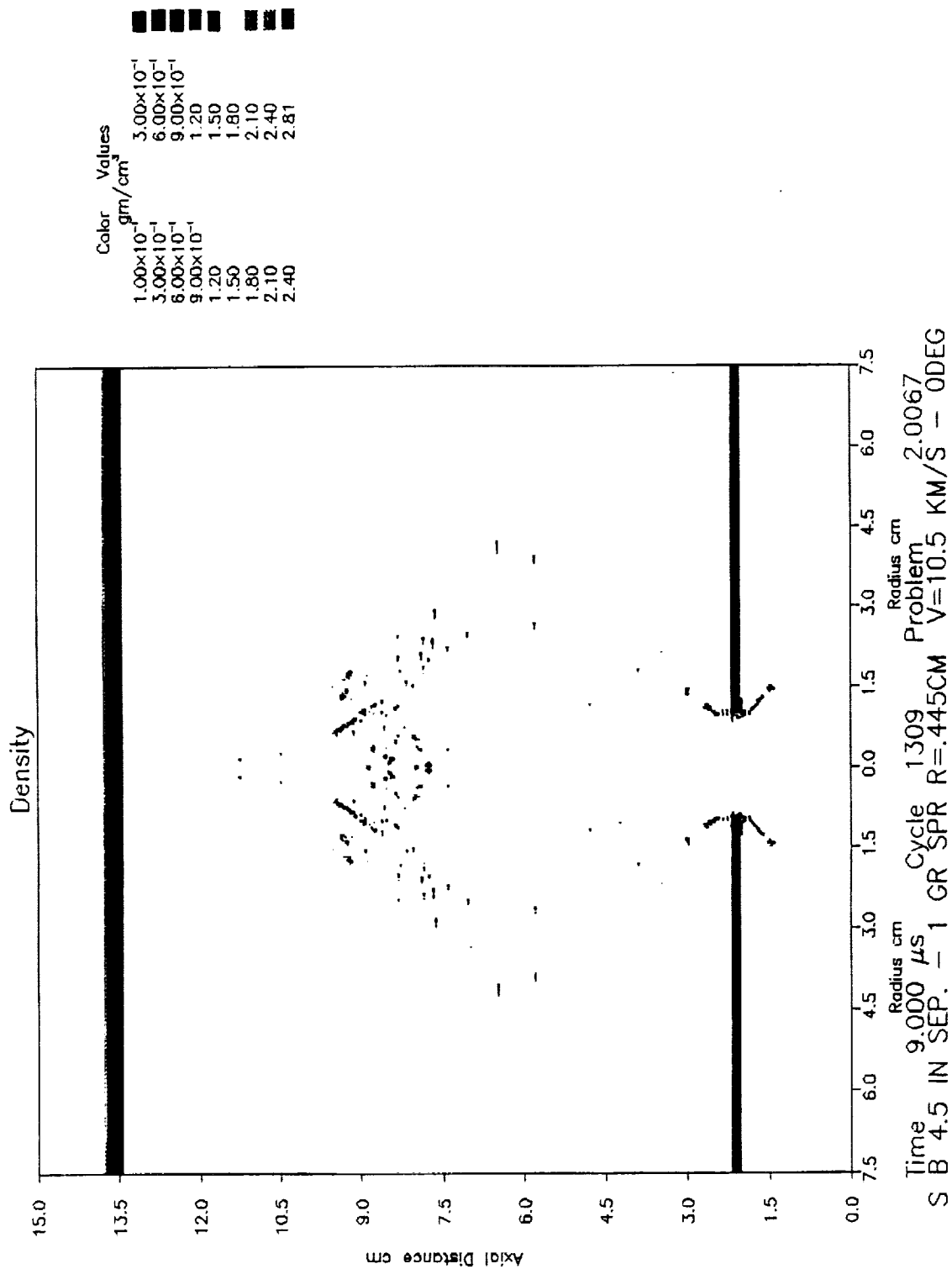


Figure 17b. HULL Code Impact Simulation NR-67-Spherical Projectile,  
 $t = 9.000 \mu s$ .

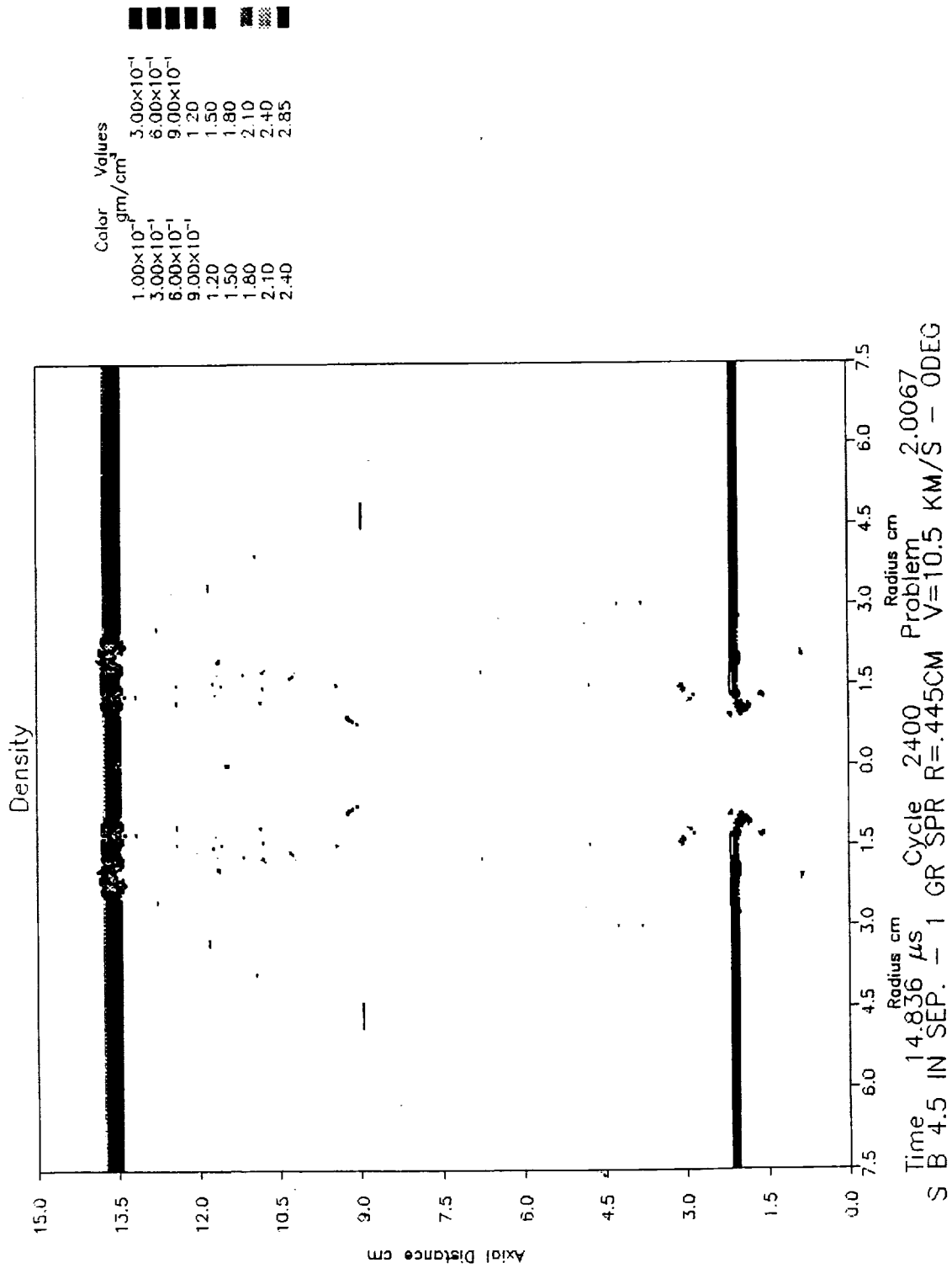


Figure 17c. HULL Code Impact Simulation NR-67-Spherical Projectile,  
 $t = 14.836 \mu$ s.

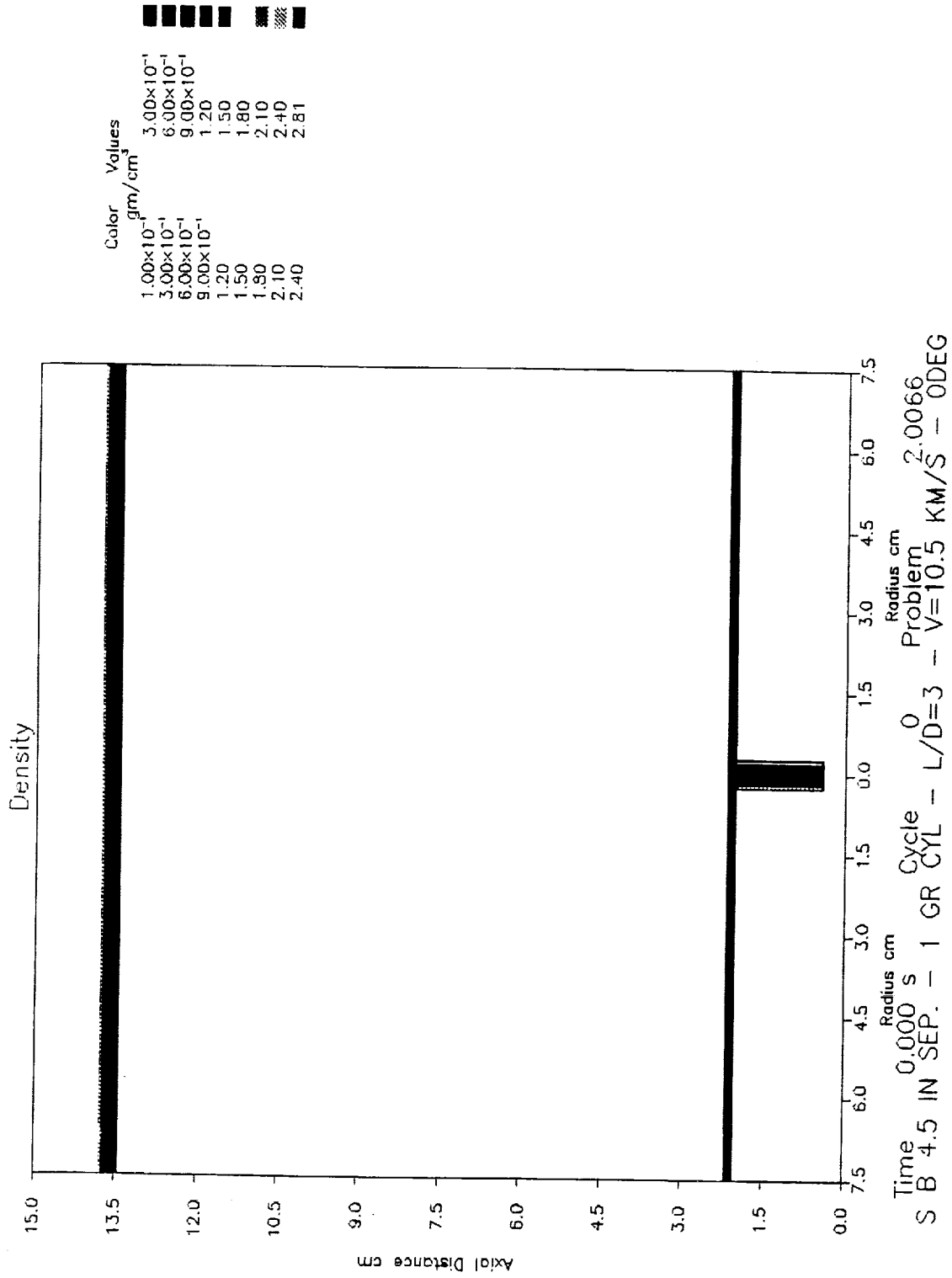


Figure 18a. HULL Code Impact Simulation NR-66-Cylindrical Projectile,  
t = 0.000 μs.

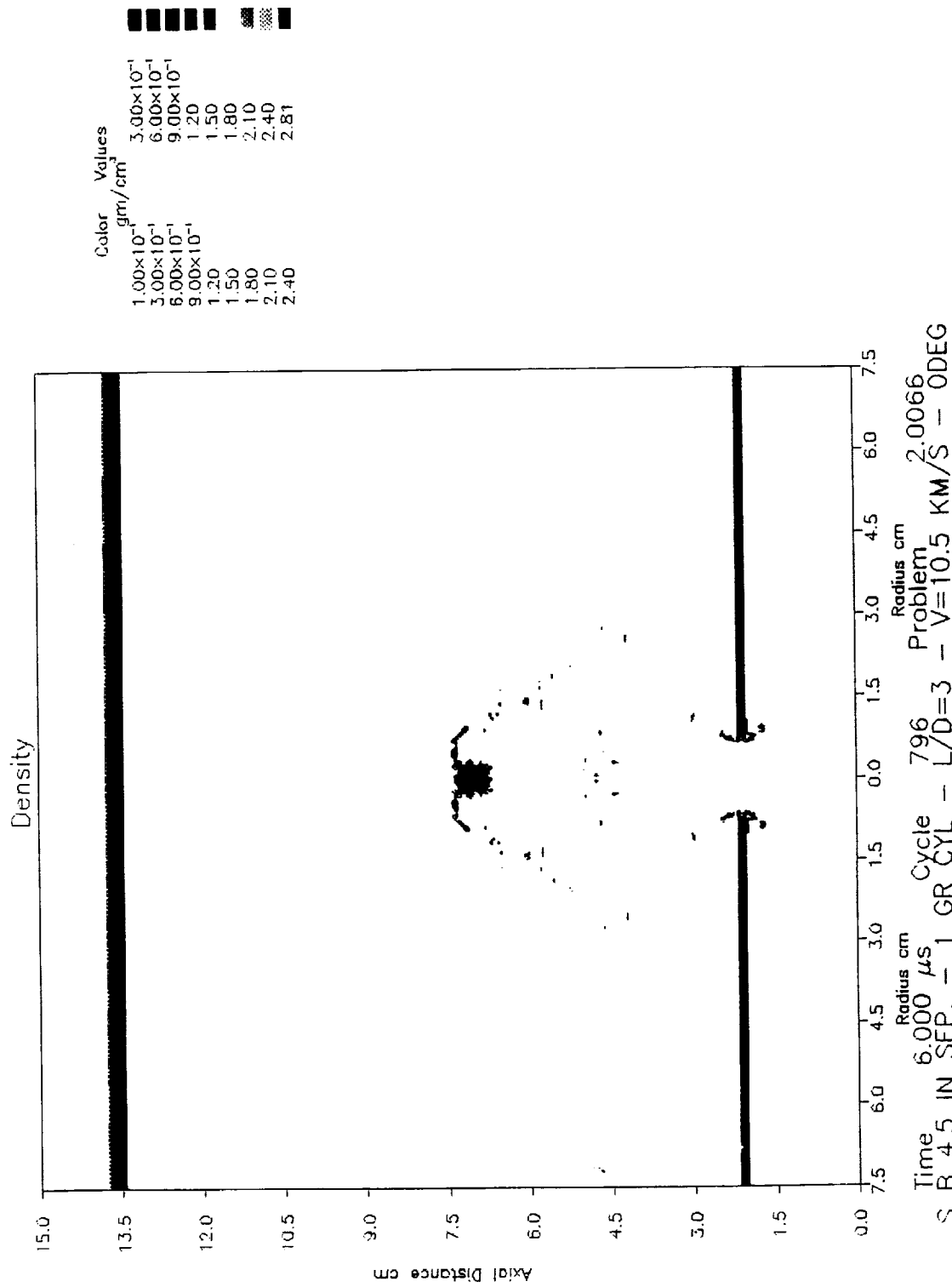


Figure 18b. HULL Code Impact Simulation NR-66-Cylindrical Projectile,  
 $t = 6.000 \mu s$ .

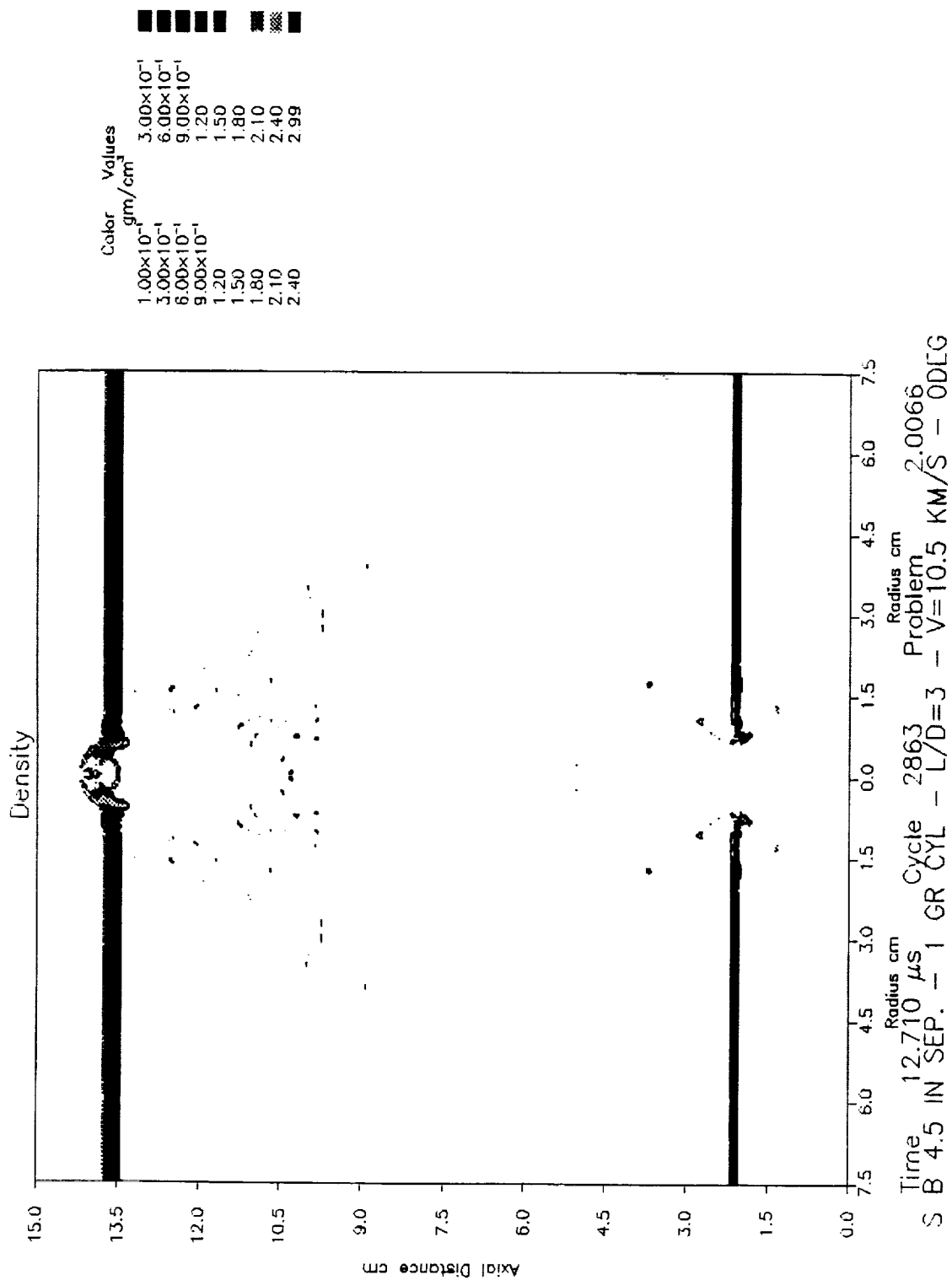


Figure 18c. HULL Code Impact Simulation NR-66-Cylindrical Projectile,  
 $t = 12.710 \mu$ s.



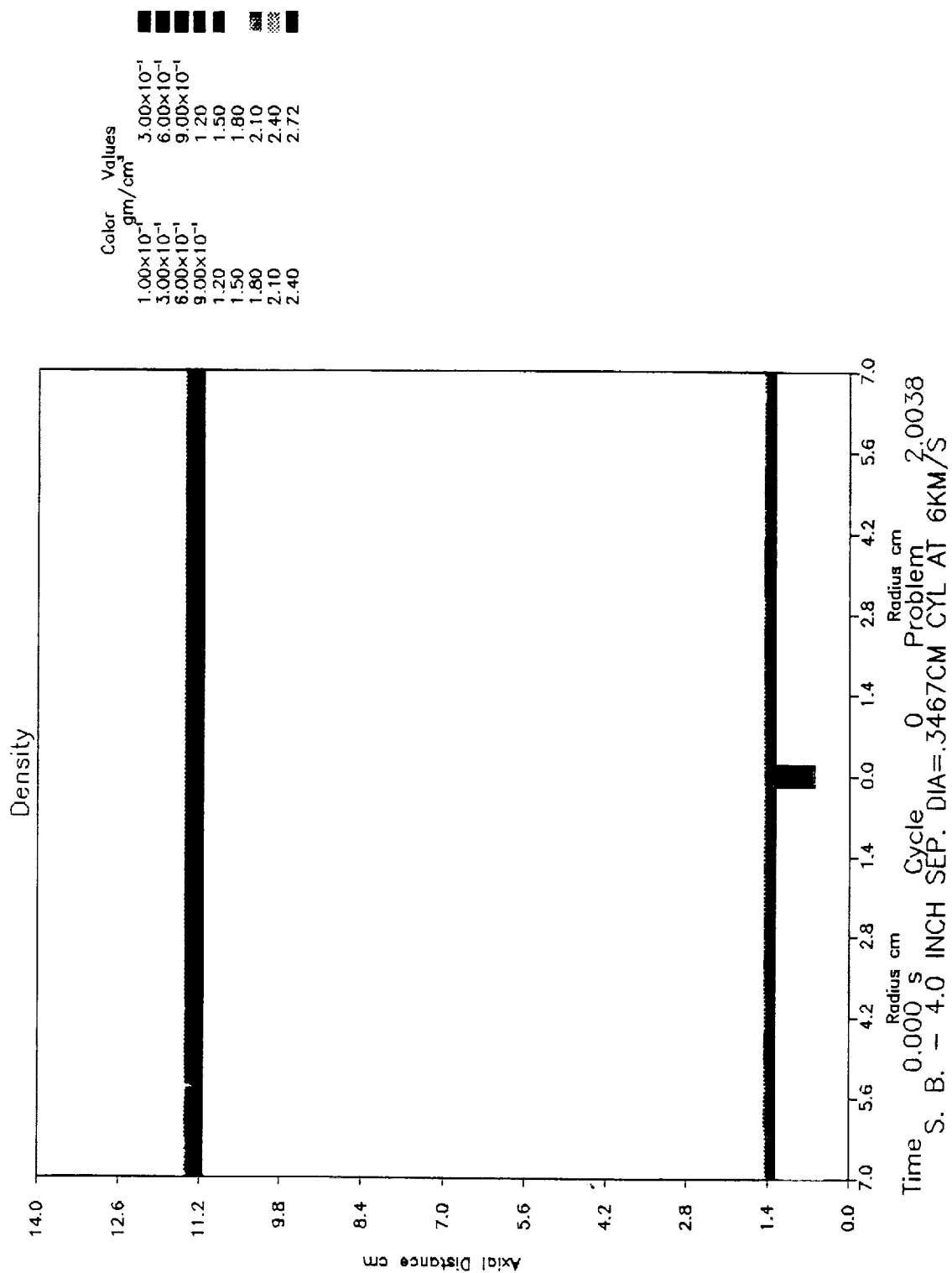


Figure 19a. HULL Code Impact Simulation NR-38-Cylindrical Projectile,  
L/d = 2.0, t = 0.000  $\mu$ s.

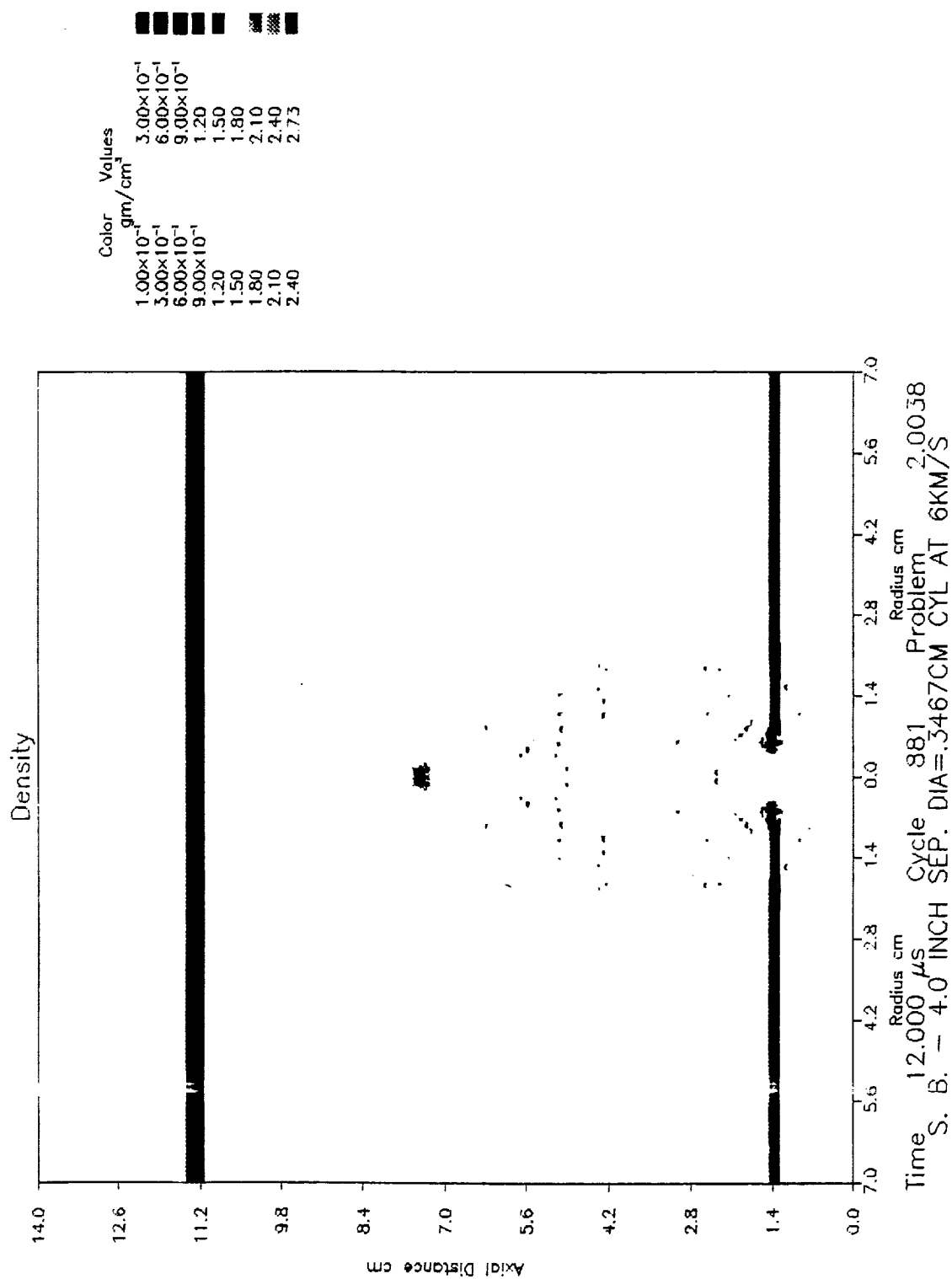


Figure 19b. HULL Code Impact Simulation NR-38-Cylindrical Projectile,  
 L/d = 2.0, t = 12.000  $\mu$ s.

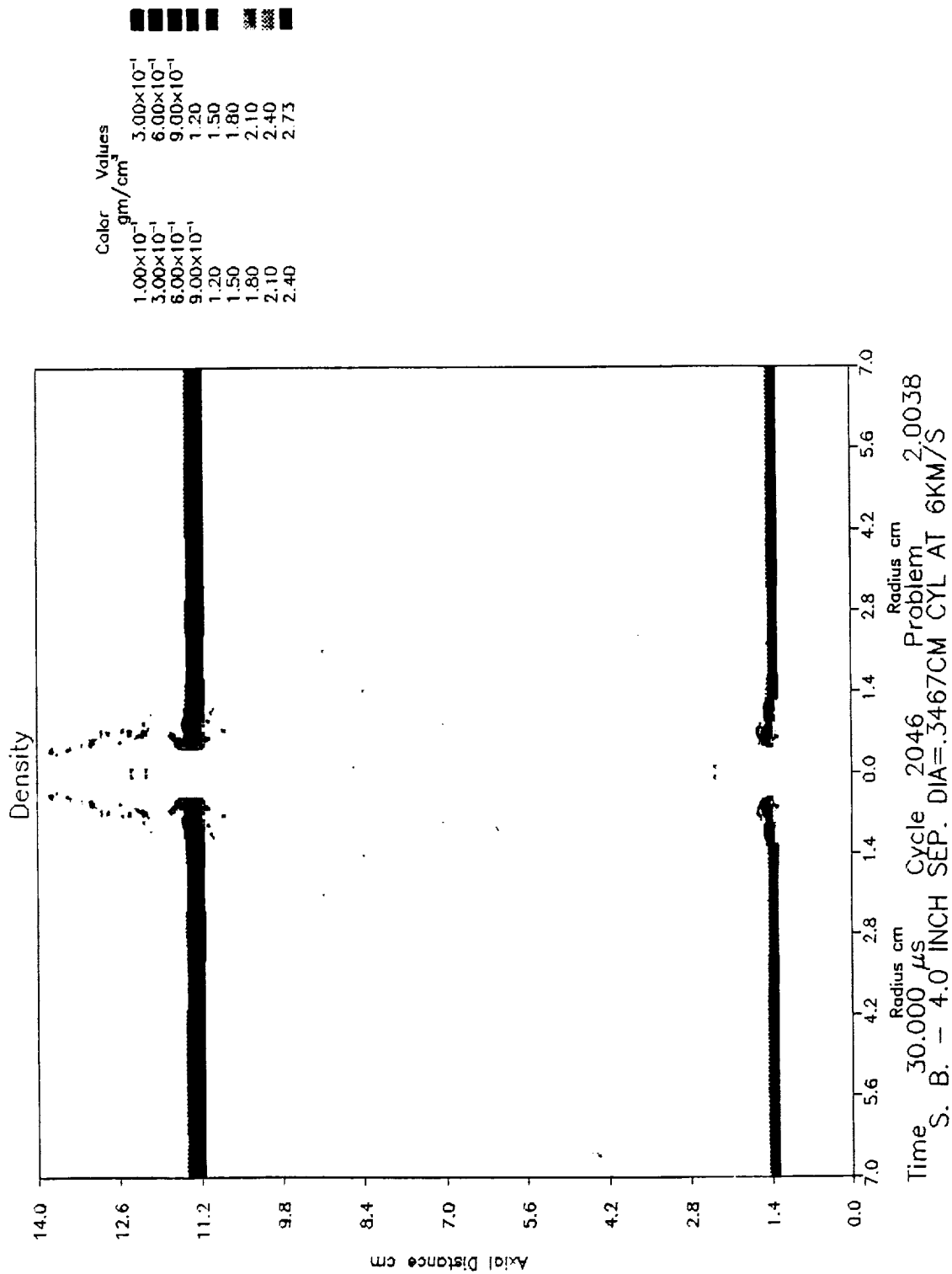


Figure 19c. HULL Code Impact Simulation NR-38-Cylindrical Projectile,  
 L/d = 2.0, t = 30.000  $\mu$ s.

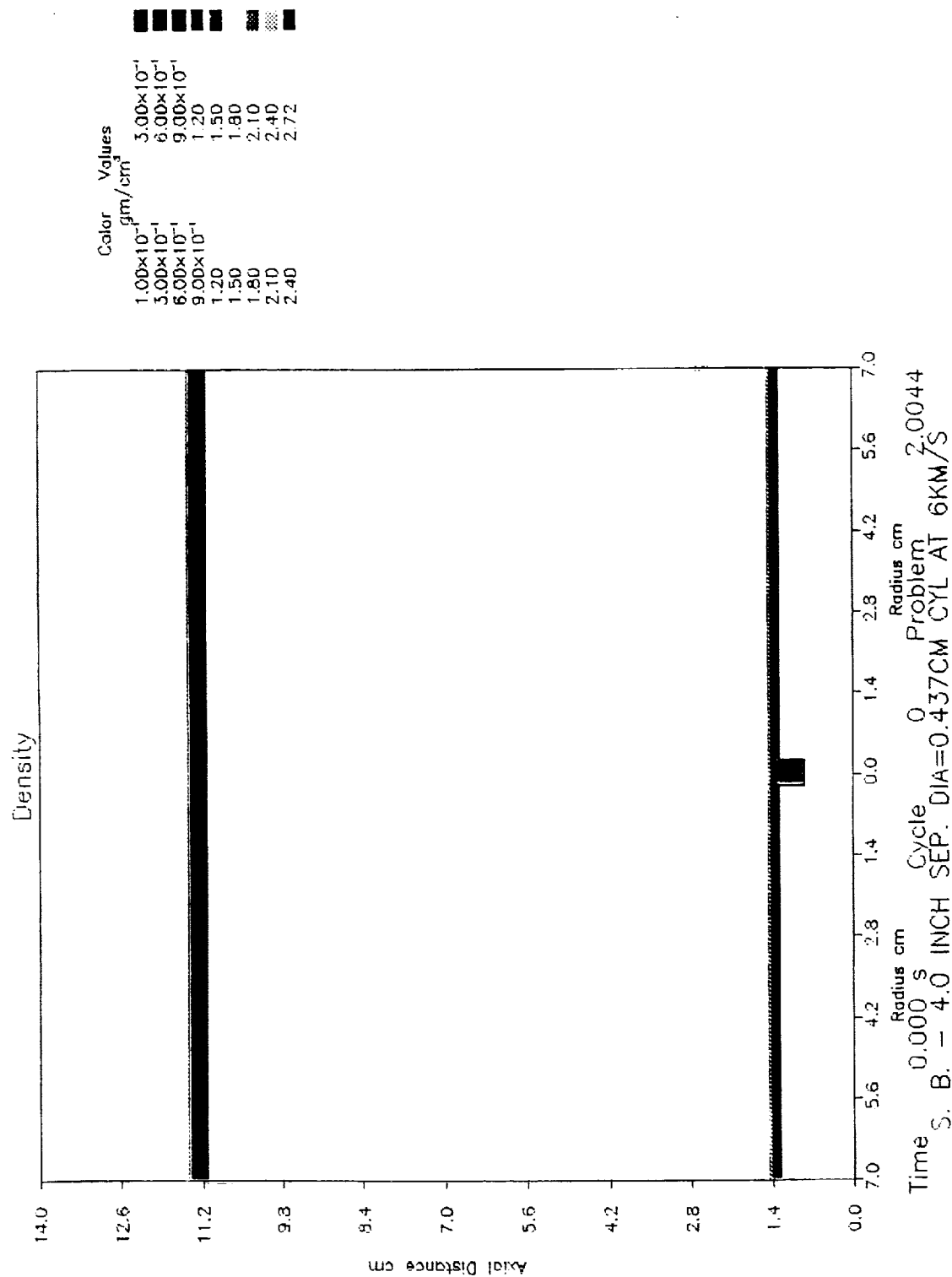


Figure 20a. HULL Code Impact Simulation NR-44-Cylindrical Projectile,  
L/d = 1.0, t = 0.000  $\mu$ s.

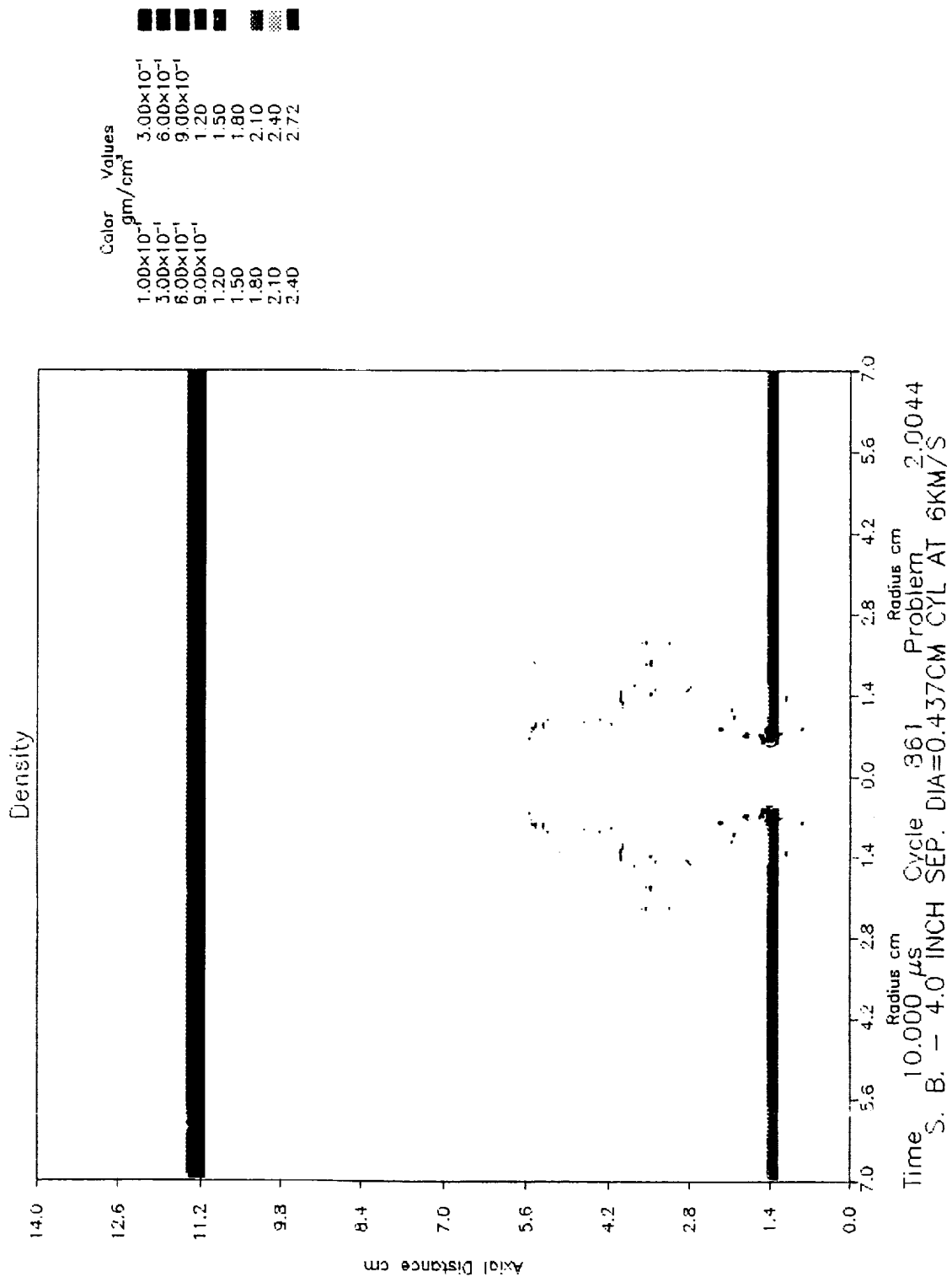


Figure 20b. HULL Code Impact Simulation NR-44-Cylindrical Projectile,  
 L/d = 1.0, t = 10.000  $\mu$ s.

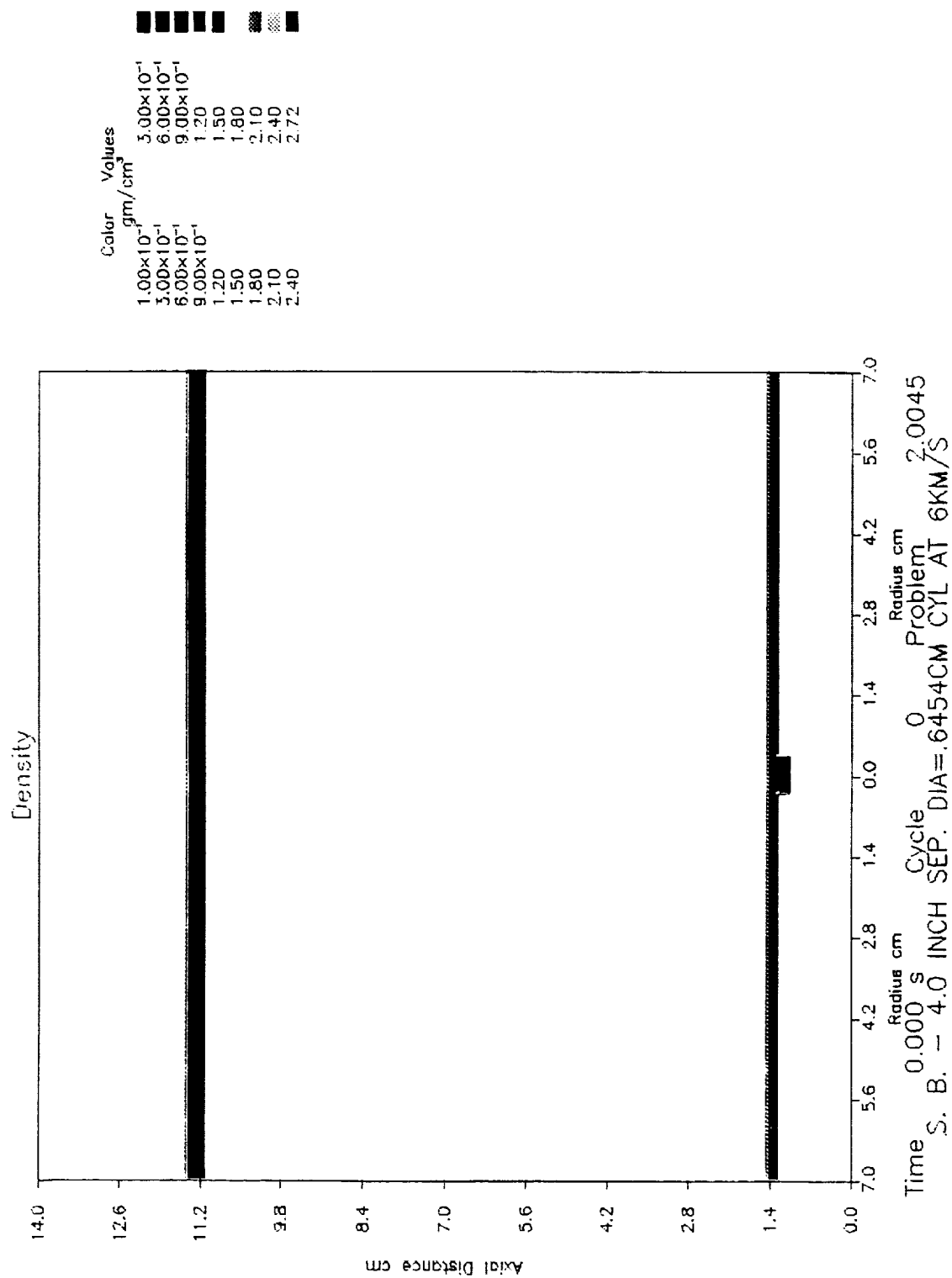


Figure 21a. HULL Code Impact Simulation NR-45-Cylindrical Projectile,  
L/d = 0.31, t = 0.000  $\mu$ s.

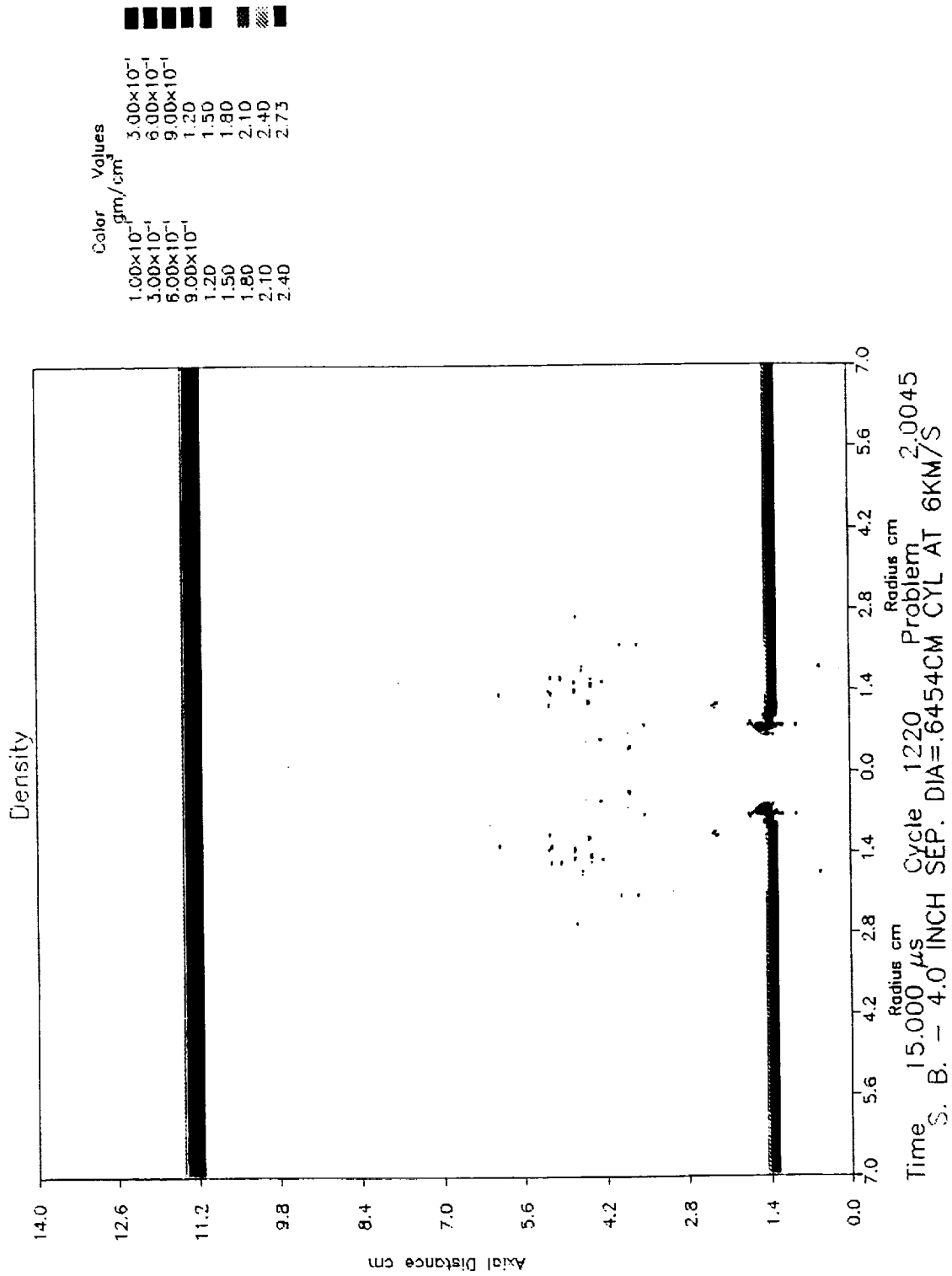


Figure 21b. HULL Code Impact Simulation NR-45-Cylindrical Projectile,  
L/d = 0.31, t = 15.000  $\mu$ s.





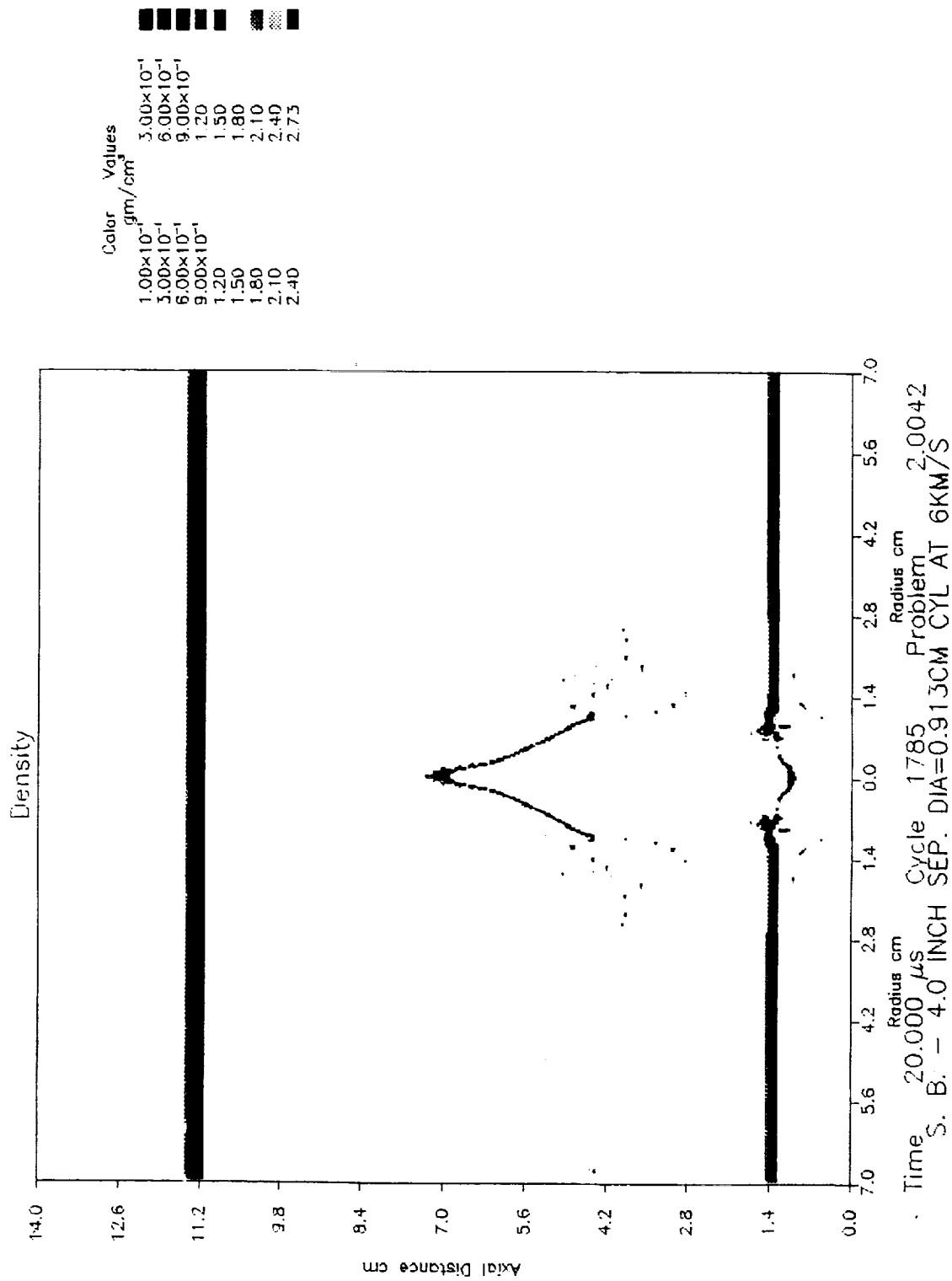


Figure 22b. HULL Code Impact Simulation NR-42-Cylindrical Projectile,  
L/d = 0.11, t = 20.000  $\mu$ s.

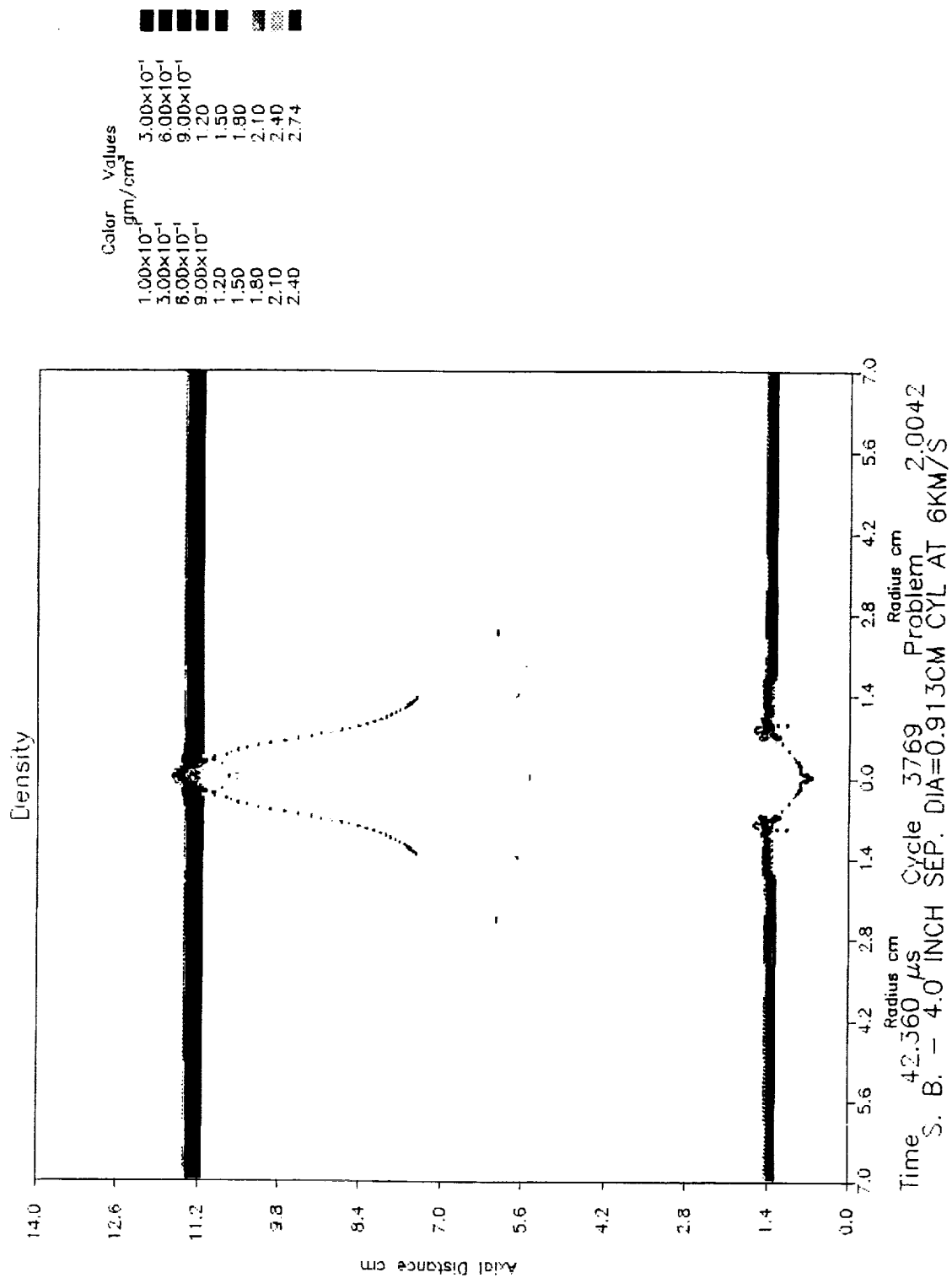


Figure 22c. HULL Code Impact Simulation NR-42-Cylindrical Projectile,  
L/d = 0.11, t = 42.360  $\mu$ s.

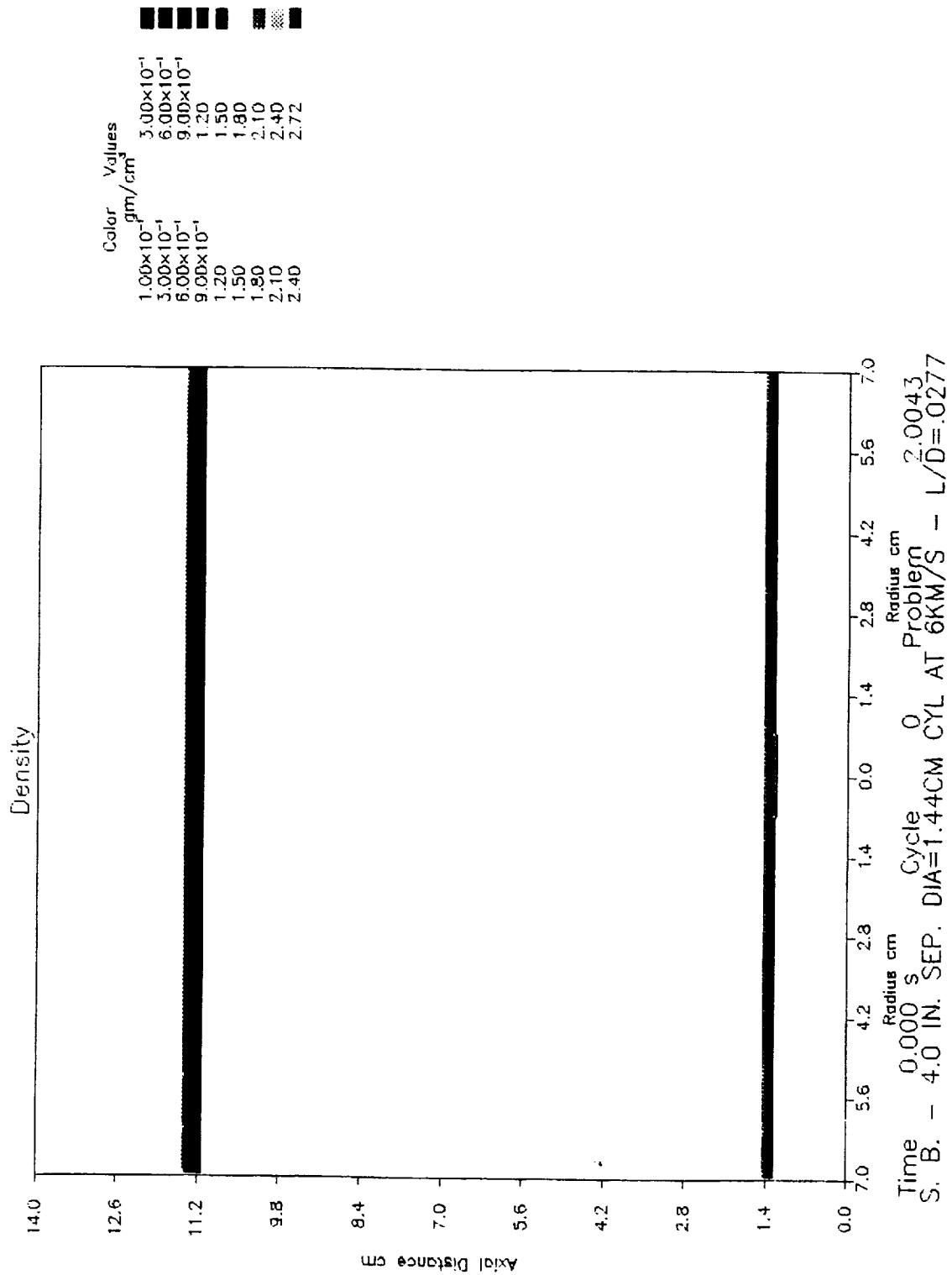


Figure 23a. HULL Code Impact Simulation NR-43-Cylindrical Projectile,  
L/d = 0.0277, t = 0.000  $\mu$ s.

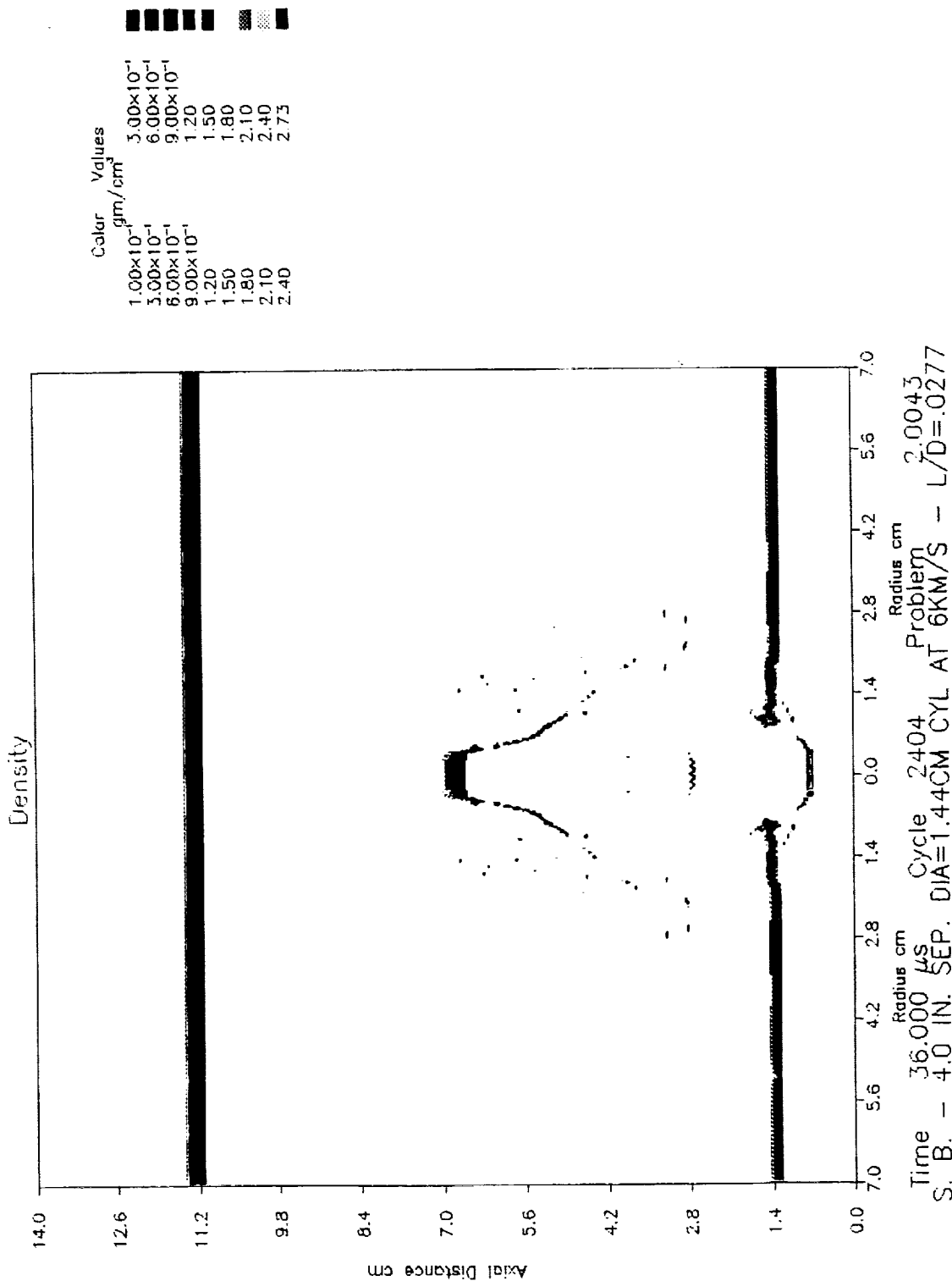


Figure 23b. HULL Code Impact Simulation NR-43-Cylindrical Projectile,  
L/d = 0.0277, t = 36.000  $\mu$ s.

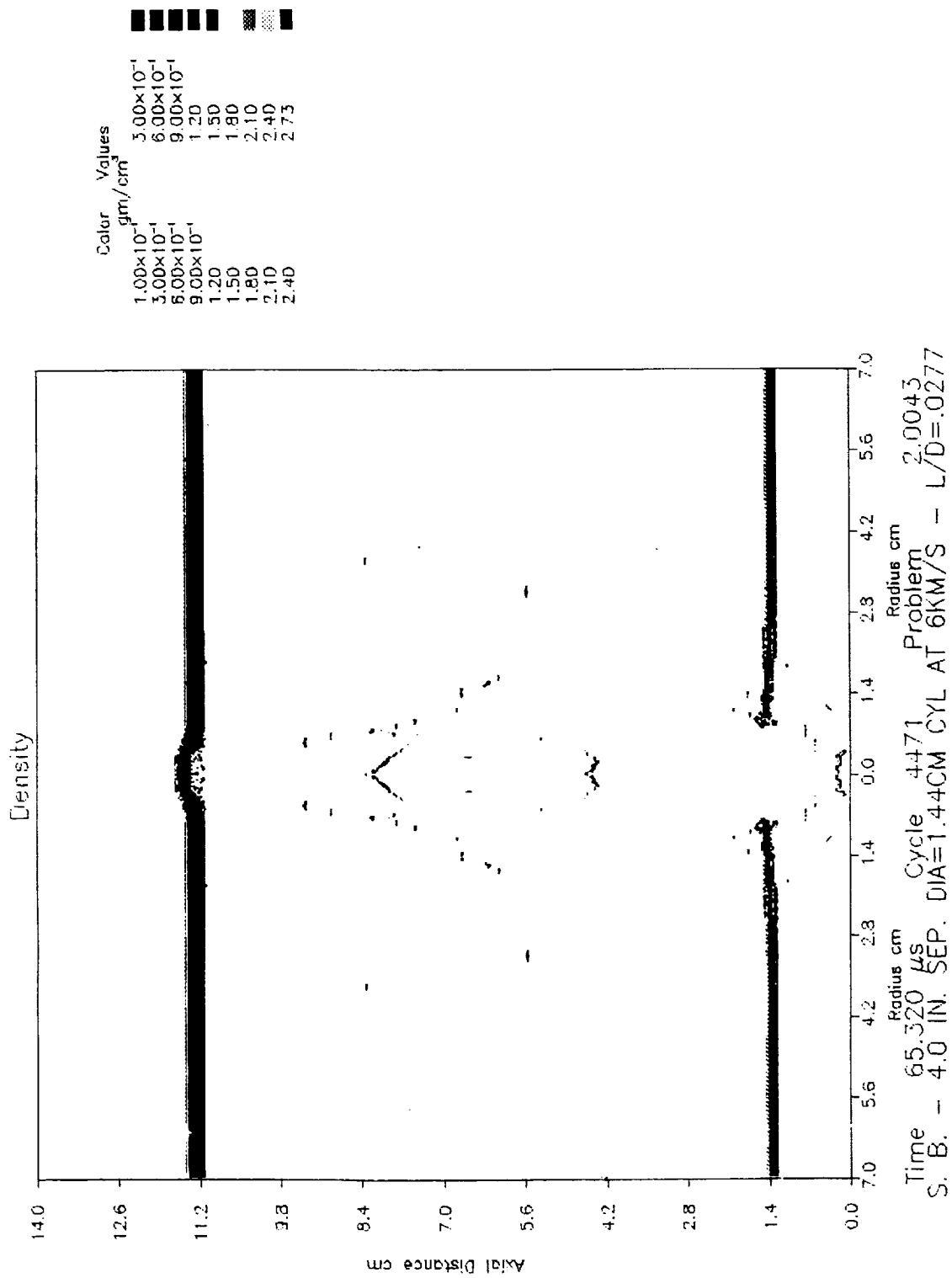


Figure 23c. HULL Code Impact Simulation NR-43-Cylindrical Projectile,  
 $L/d = 0.0277$ ,  $t = 65.320 \mu s$ .

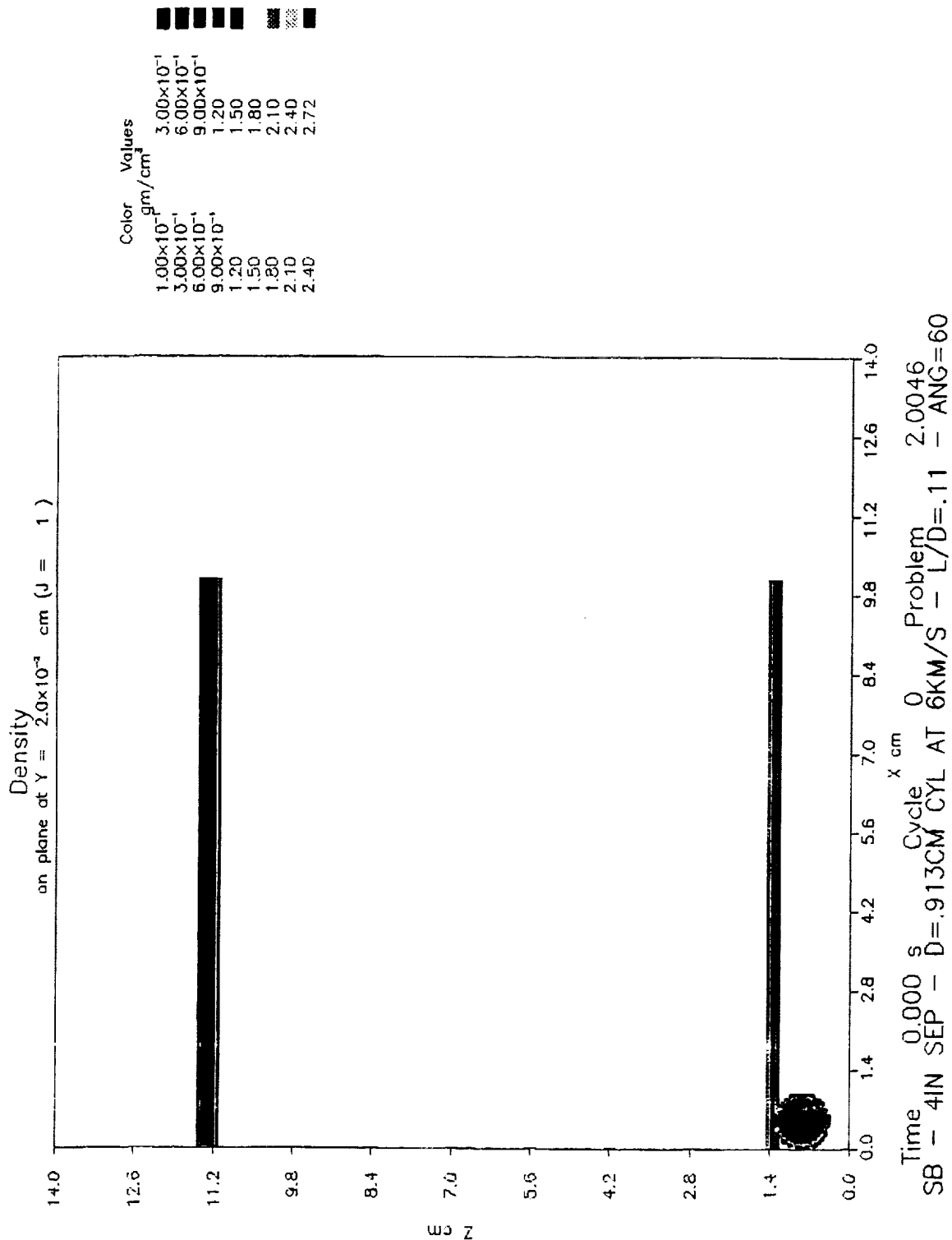


Figure 24a. HULL Code Impact Simulation NR-46-Cylindrical Projectile,  $L/d = 0.11$ ,  
 $\theta = 60^\circ$ ,  $\phi = 0^\circ$ ,  $\psi = 90^\circ$ ,  $t = 0.000 \mu s$ .

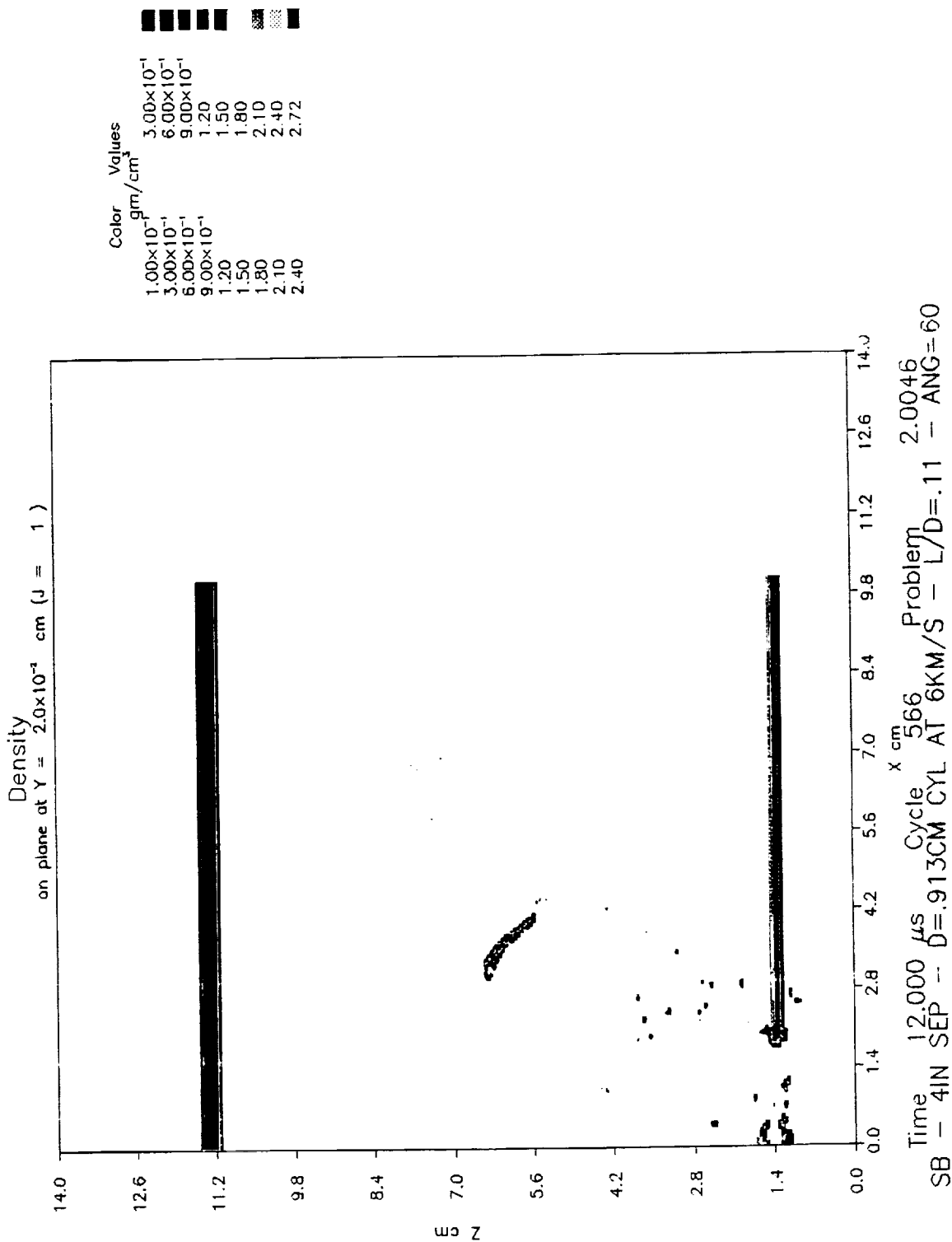


Figure 24b. HULL Code Impact Simulation NR-46-Cylindrical Projectile,  $L/d = 0.11$ ,  $\theta = 60^\circ$ ,  $\phi = 0^\circ$ ,  $\psi = 90^\circ$ ,  $t = 12.000 \mu$ s.

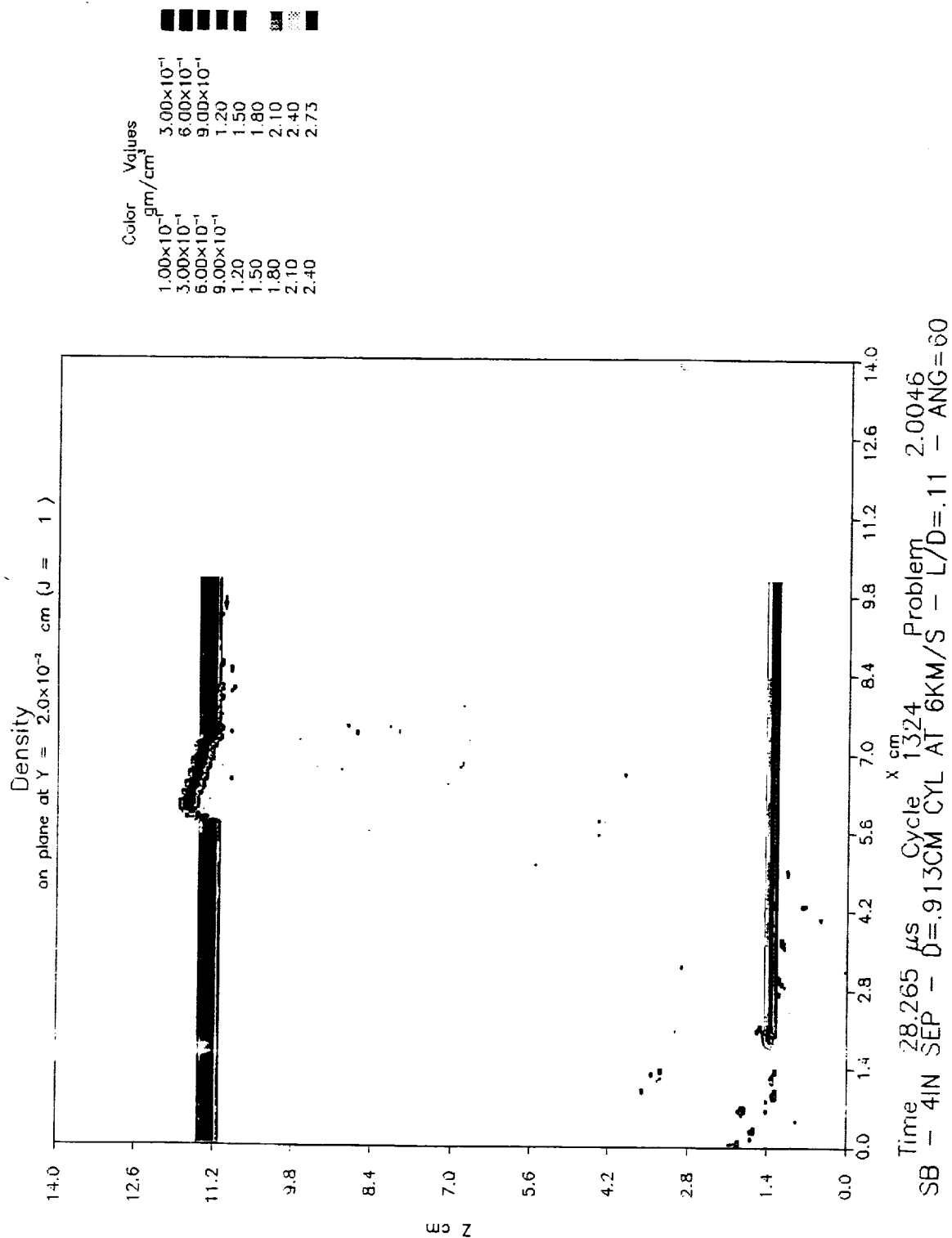


Figure 24c. HULL Code Impact Simulation NR-46-Cylindrical Projectile,  $L/d = 0.11$ ,  $\theta = 60^\circ$ ,  $\phi = 0^\circ$ ,  $\psi = 90^\circ$ ,  $t = 28.265 \mu$ s.



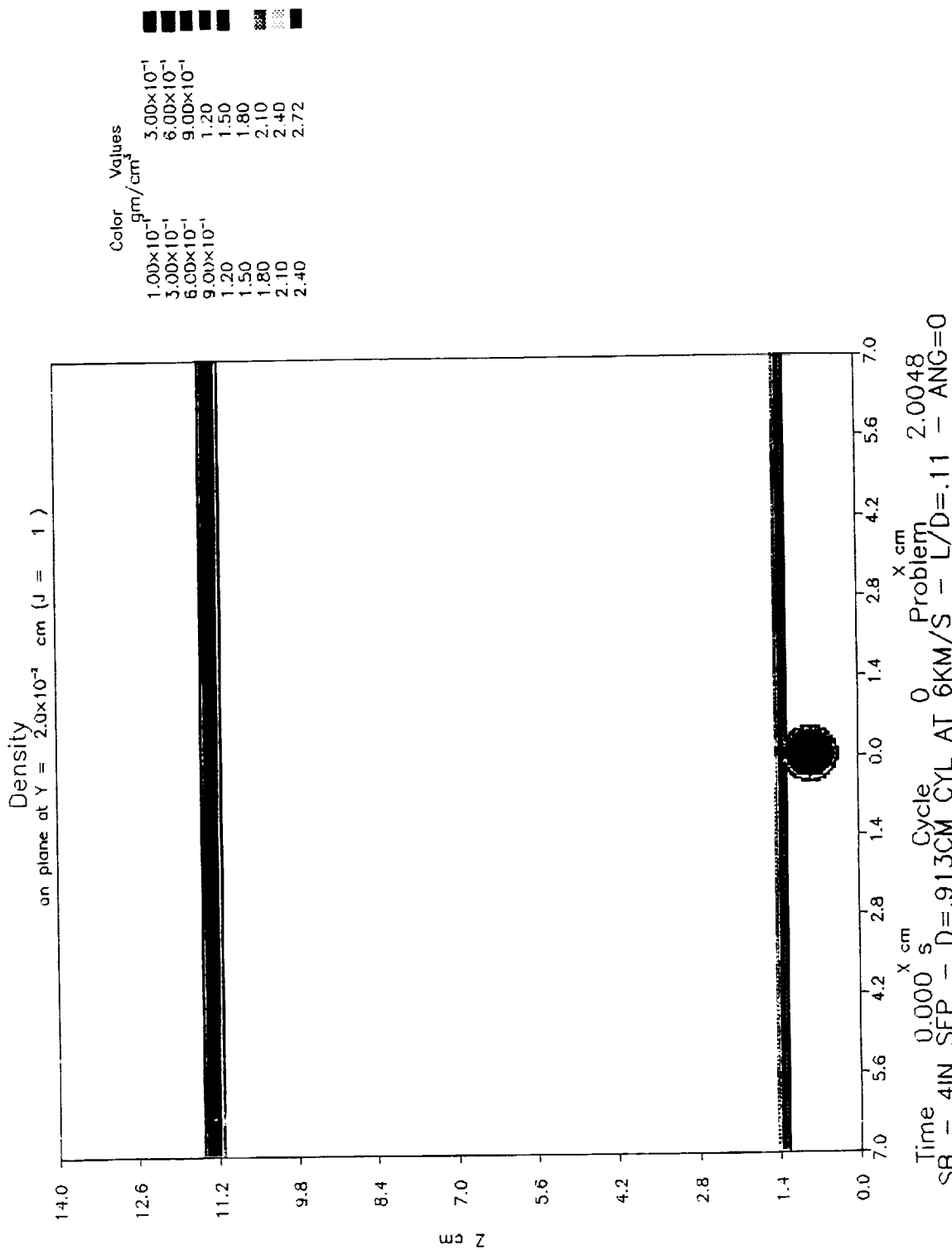


Figure 25a. HULL Code Impact Simulation NR-48-Cylindrical Projectile,  $L/d = 0.11$ ,  $\theta = 0^\circ$ ,  $\phi = 0^\circ$ ,  $\psi = 90^\circ$ ,  $t = 0.000 \mu\text{s}$ .

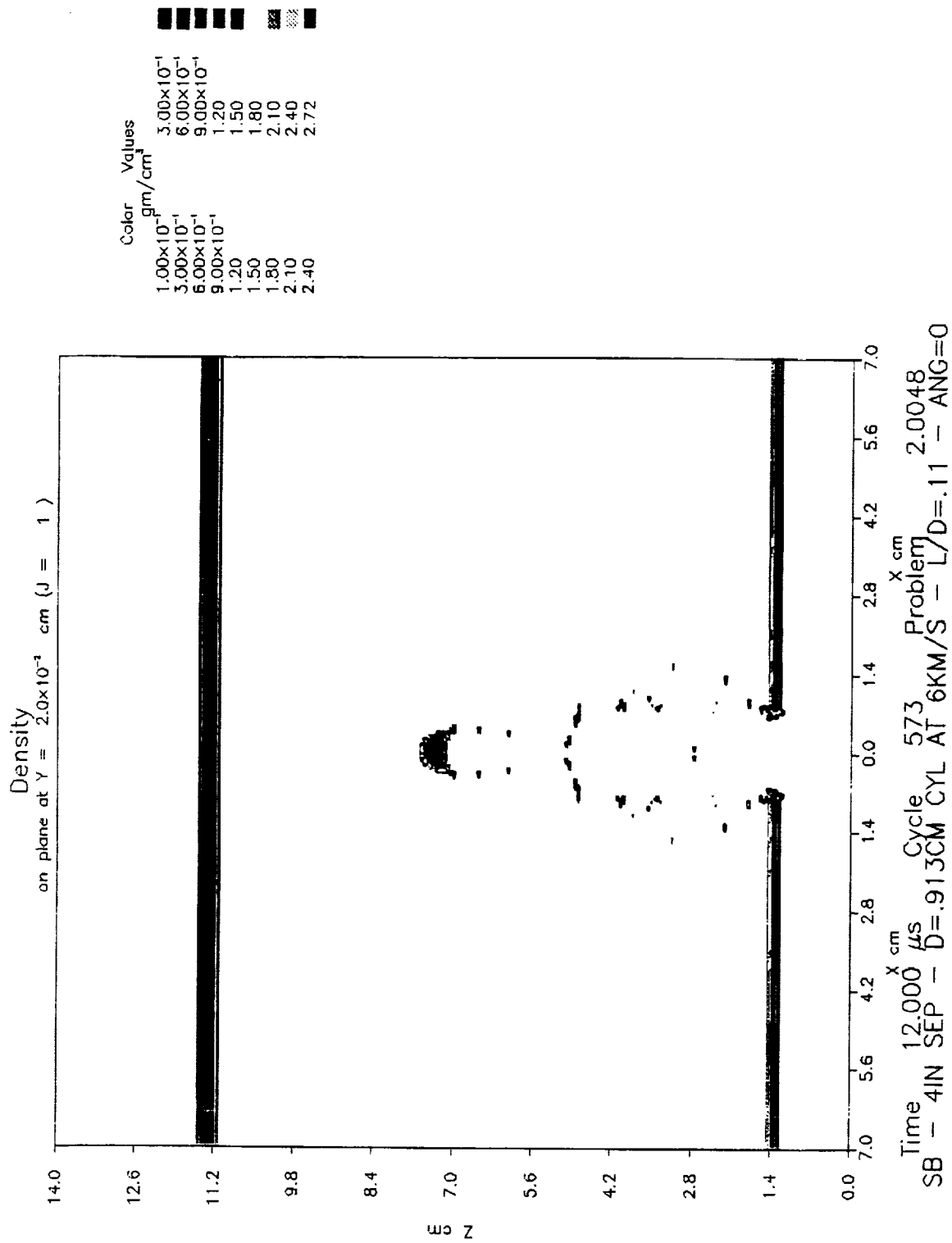


Figure 25b. HULL Code Impact Simulation NR-48-Cylindrical Projectile,  $L/d = 0.11$ ,  $\theta = 0^\circ$ ,  $\phi = 0^\circ$ ,  $\psi = 90^\circ$ ,  $t = 12.000 \mu\text{s}$ .

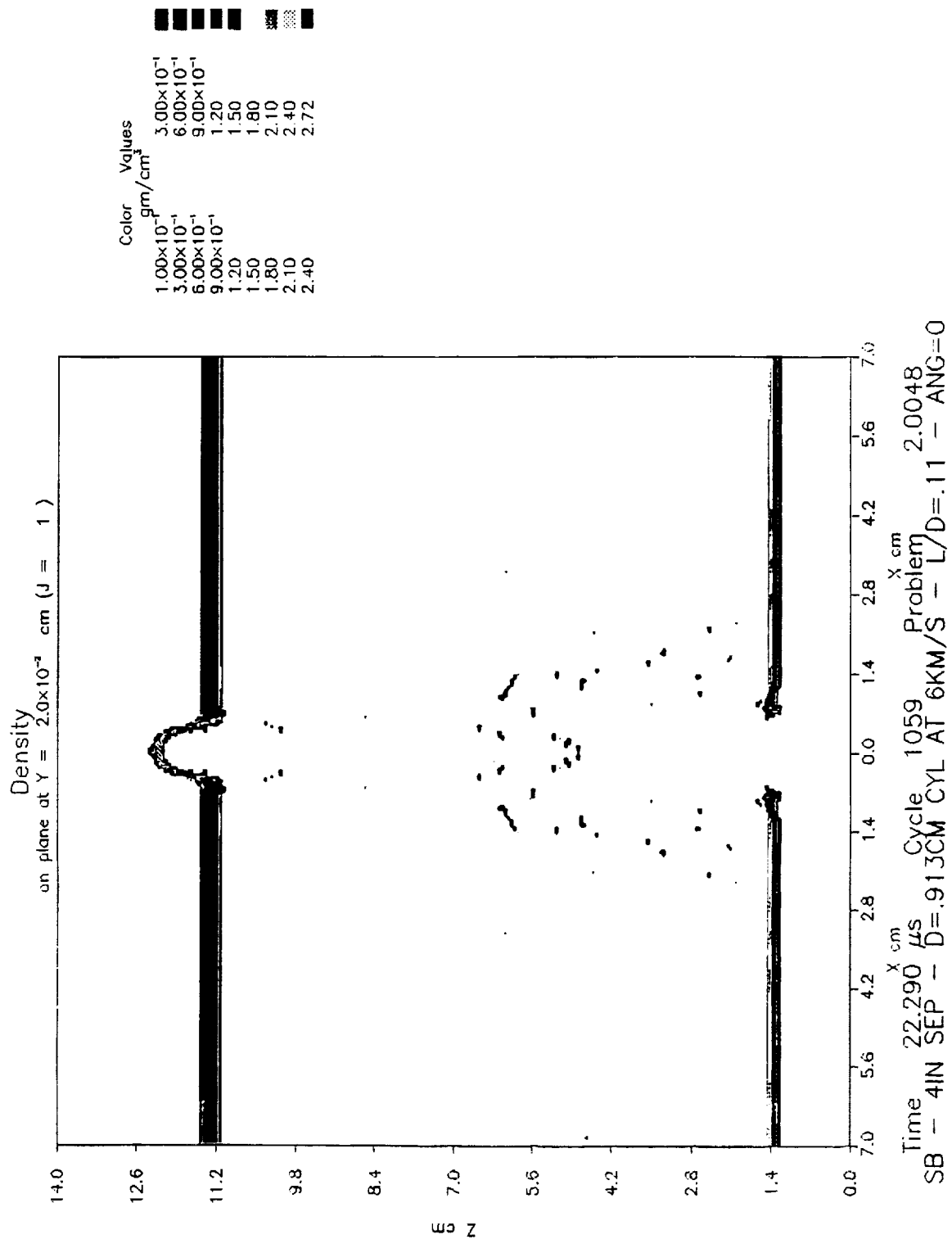


Figure 25c. HULL Code Impact Simulation NR-48-Cylindrical Projectile,  $L/d = 0.11$ ,  $\theta = 0^\circ$ ,  $\phi = 0^\circ$ ,  $\psi = 90^\circ$ ,  $t = 22.290 \mu$ s.

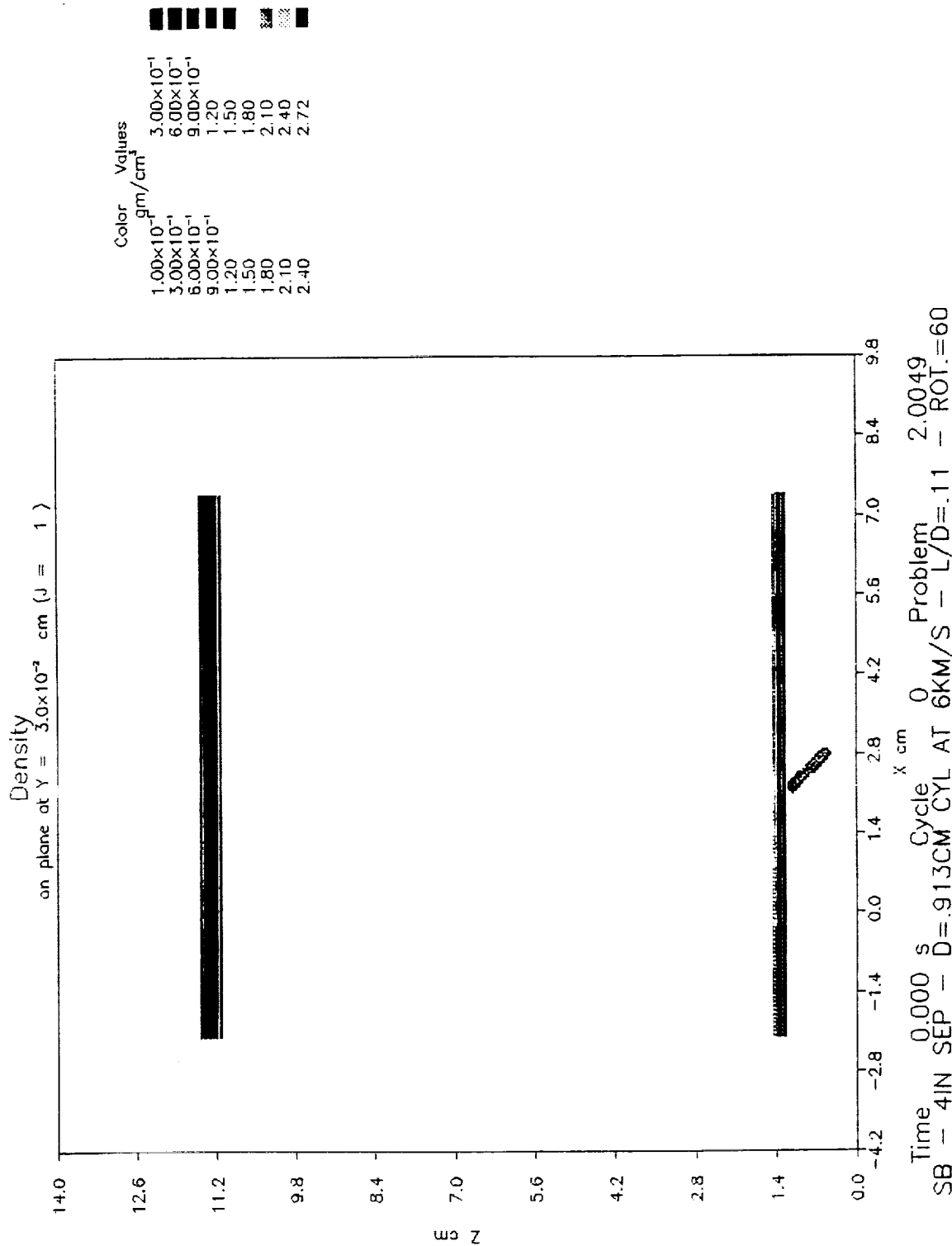


Figure 26a. HULL Code Impact Simulation NR-49-Cylindrical Projectile,  $L/d = 0.11$ ,  
 $\theta = 0^\circ$ ,  $\phi = 60^\circ$ ,  $\psi = 0^\circ$ ,  $t = 0.000 \mu s$ .

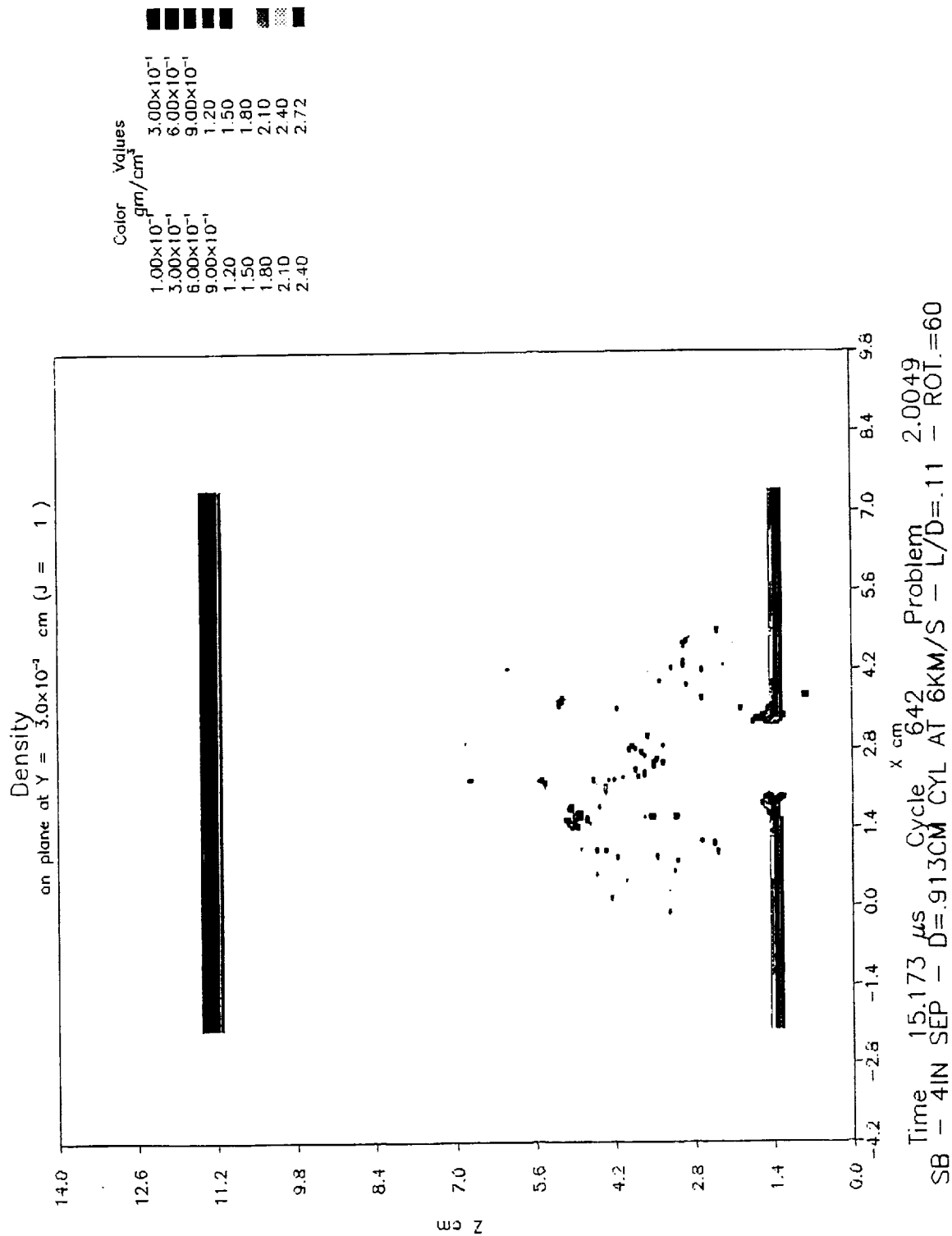


Figure 26b. HULL Code Impact Simulation NR-49-Cylindrical Projectile,  $L/d = 0.11$ ,  $\theta = 0^\circ$ ,  $\phi = 60^\circ$ ,  $\psi = 0^\circ$ ,  $t = 15.173 \mu\text{s}$ .

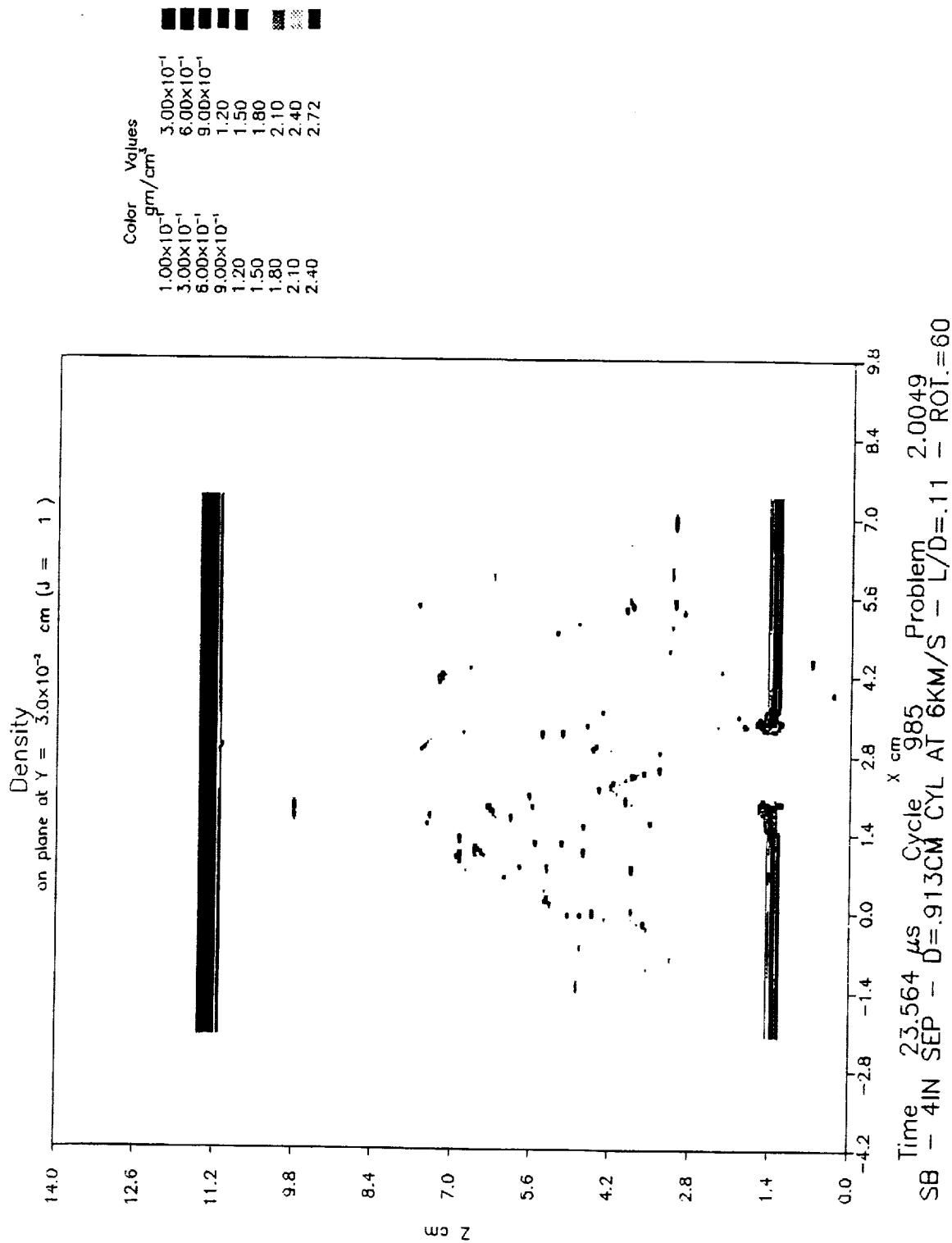


Figure 26c. HULL Code Impact Simulation NR-49-Cylindrical Projectile,  $L/d = 0.11$ ,  $\theta = 0^\circ$ ,  $\phi = 60^\circ$ ,  $\psi = 0^\circ$ ,  $t = 23.564 \mu\text{s}$ .

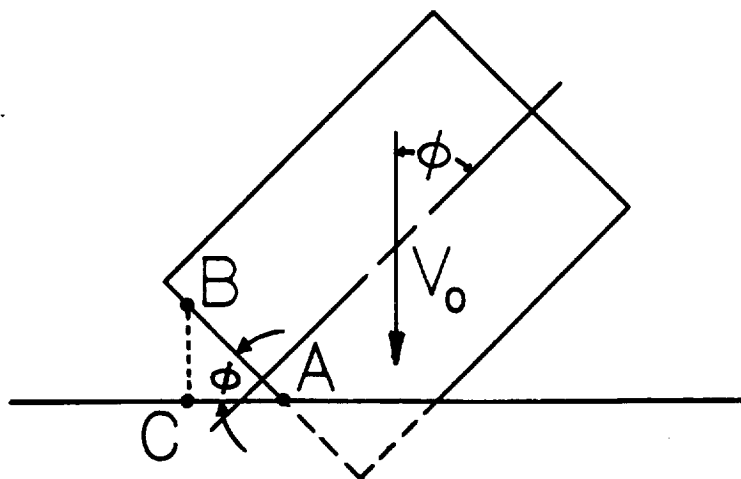


Figure 27. Critical Yaw Angle Calculation Geometry.

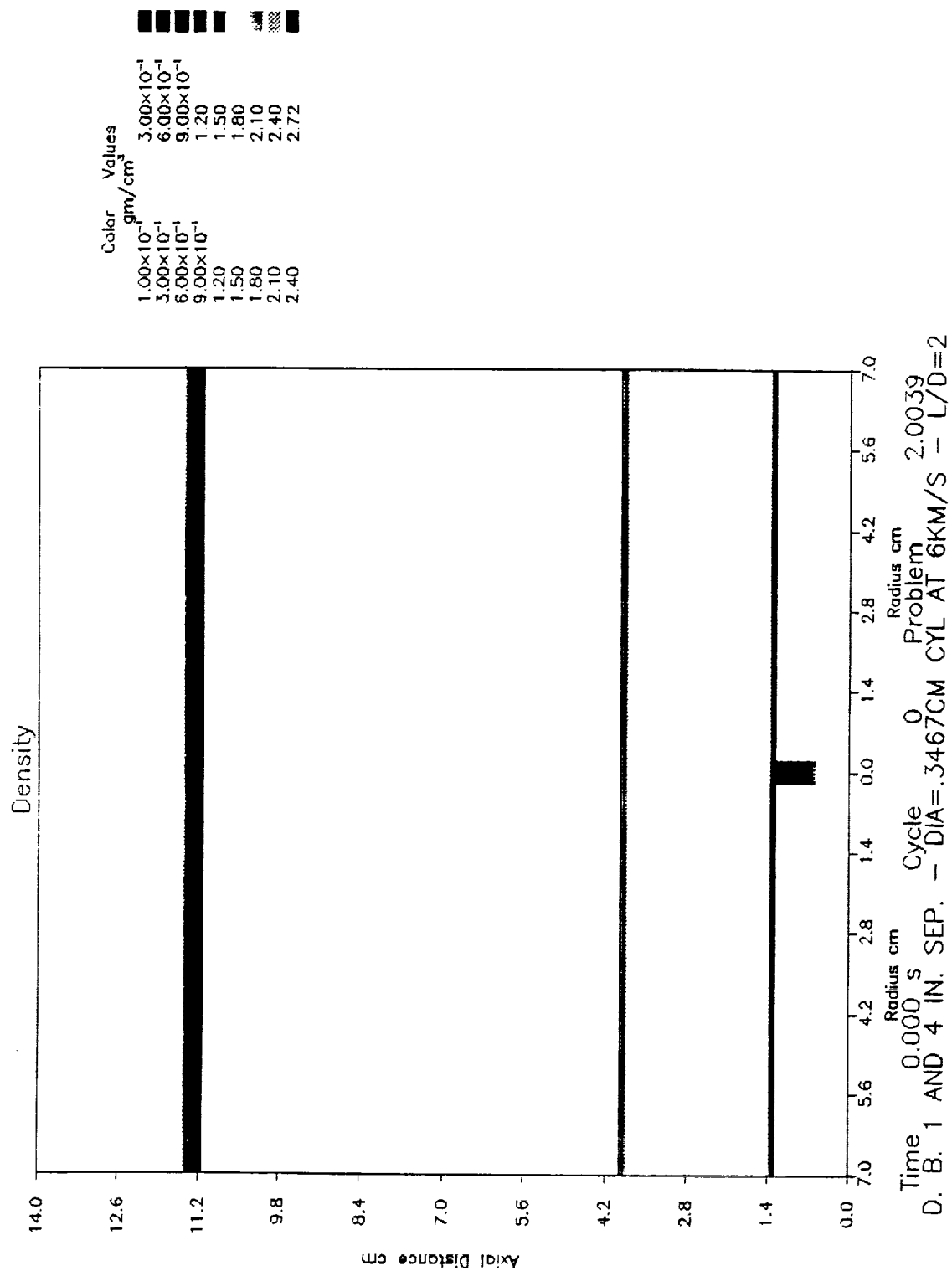


Figure 28a. HULL Code Impact Simulation NR-39-Cylindrical Projectile, Double-Bumper System, L/d = 2.0, t = 0.000  $\mu$ s.



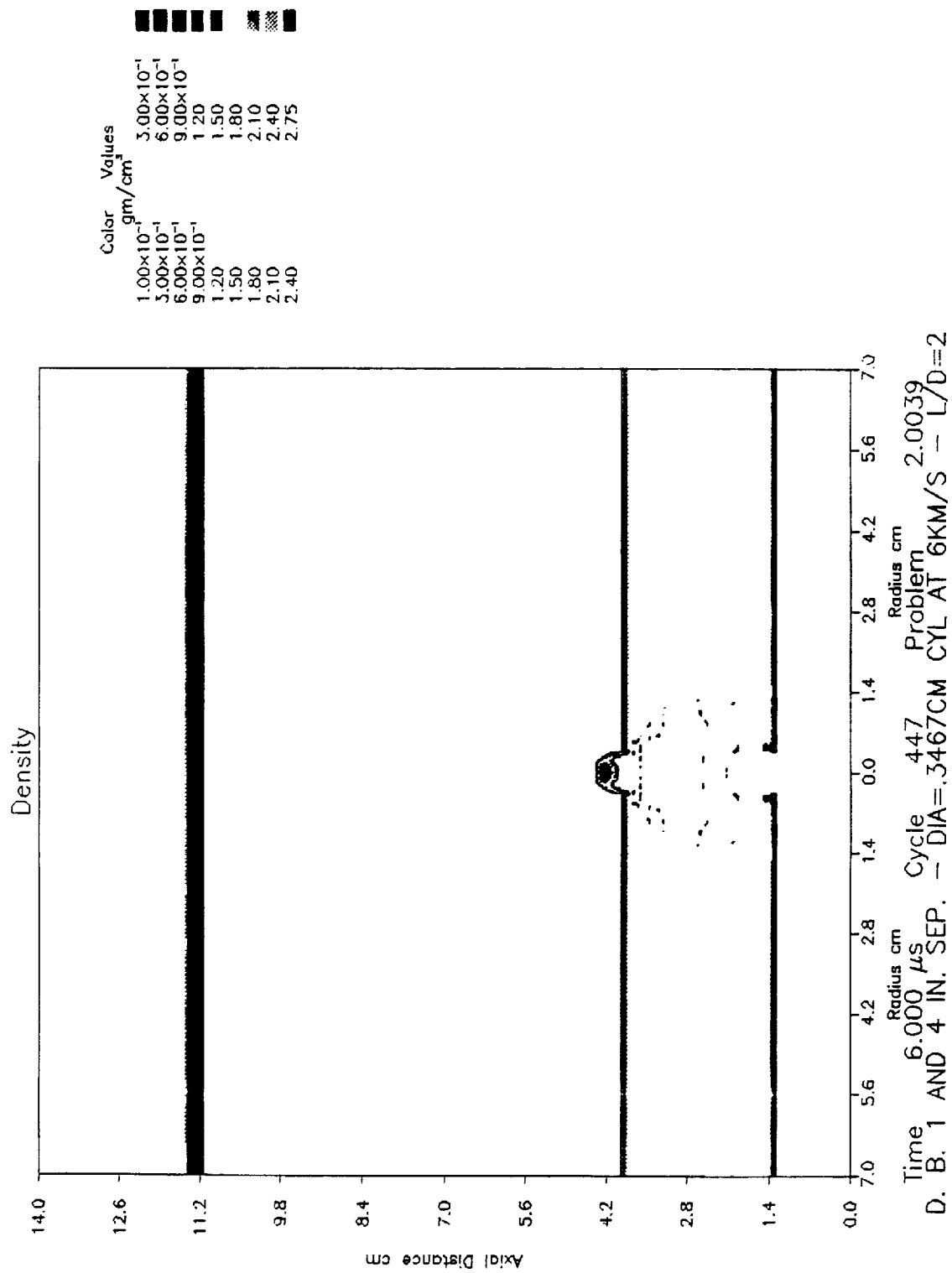


Figure 28b. HULL Code Impact Simulation NR-39-Cylindrical Projectile, Double-Bumper System, L/d = 2.0, t = 6.000  $\mu$ s.

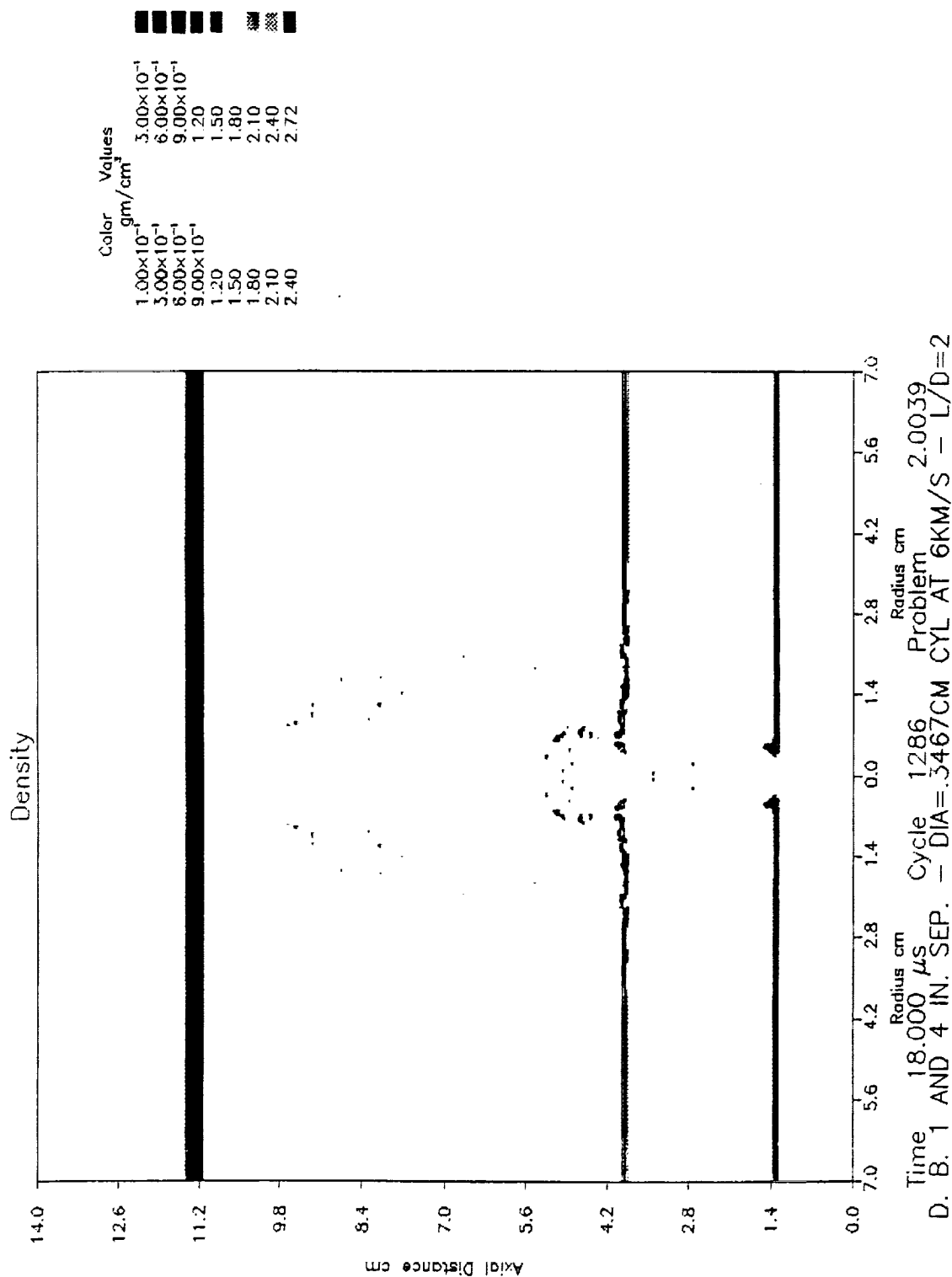


Figure 28c. HULL Code Impact Simulation NR-39-Cylindrical Projectile, Double-Bumper System, L/d = 2.0, t = 18.000  $\mu$  s.

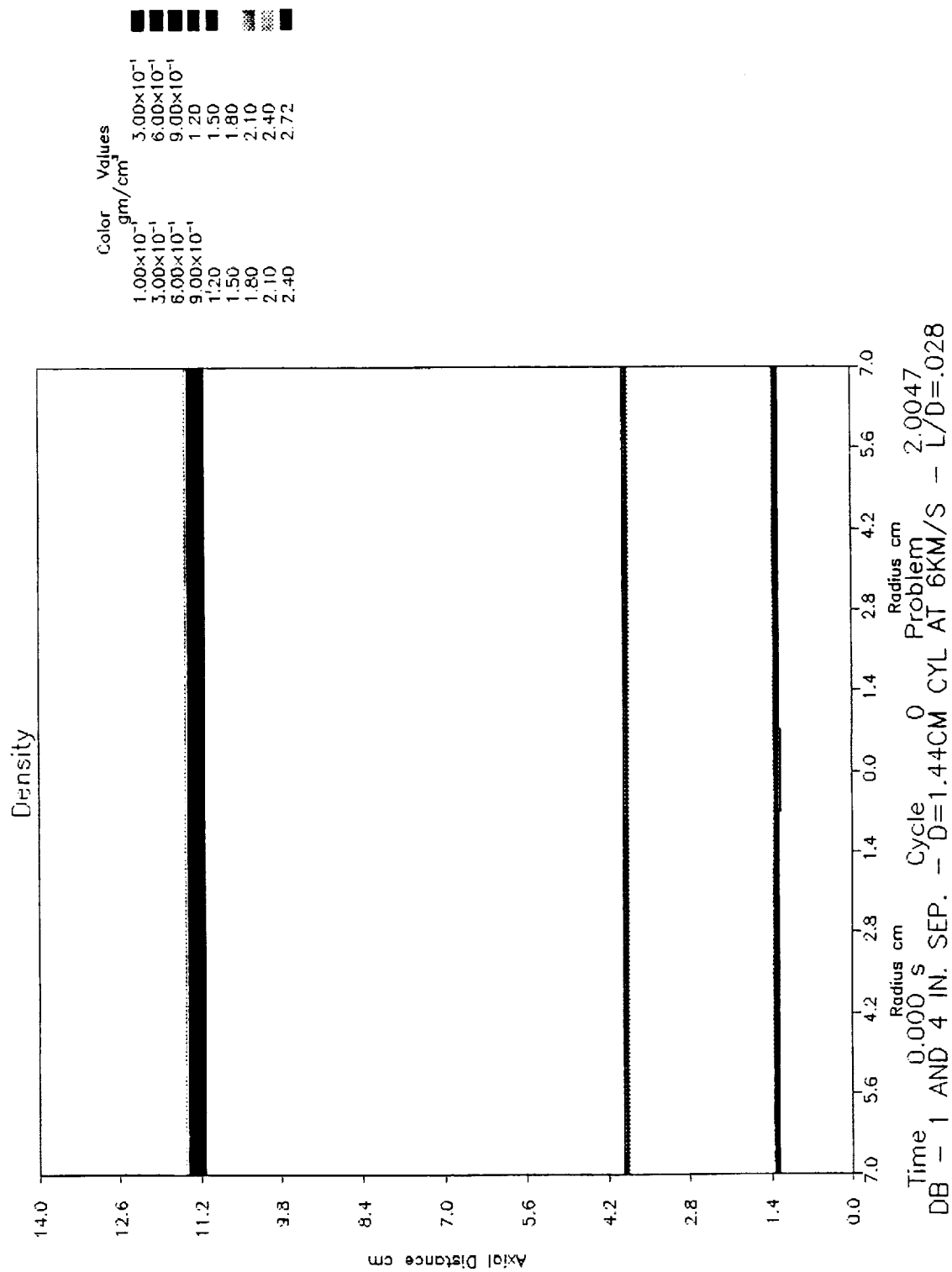


Figure 29a. HULL Code Impact Simulation NR-47-Cylindrical Projectile, Double-Bumper System, L/d = 0.0277, t = 0.000  $\mu$  s.

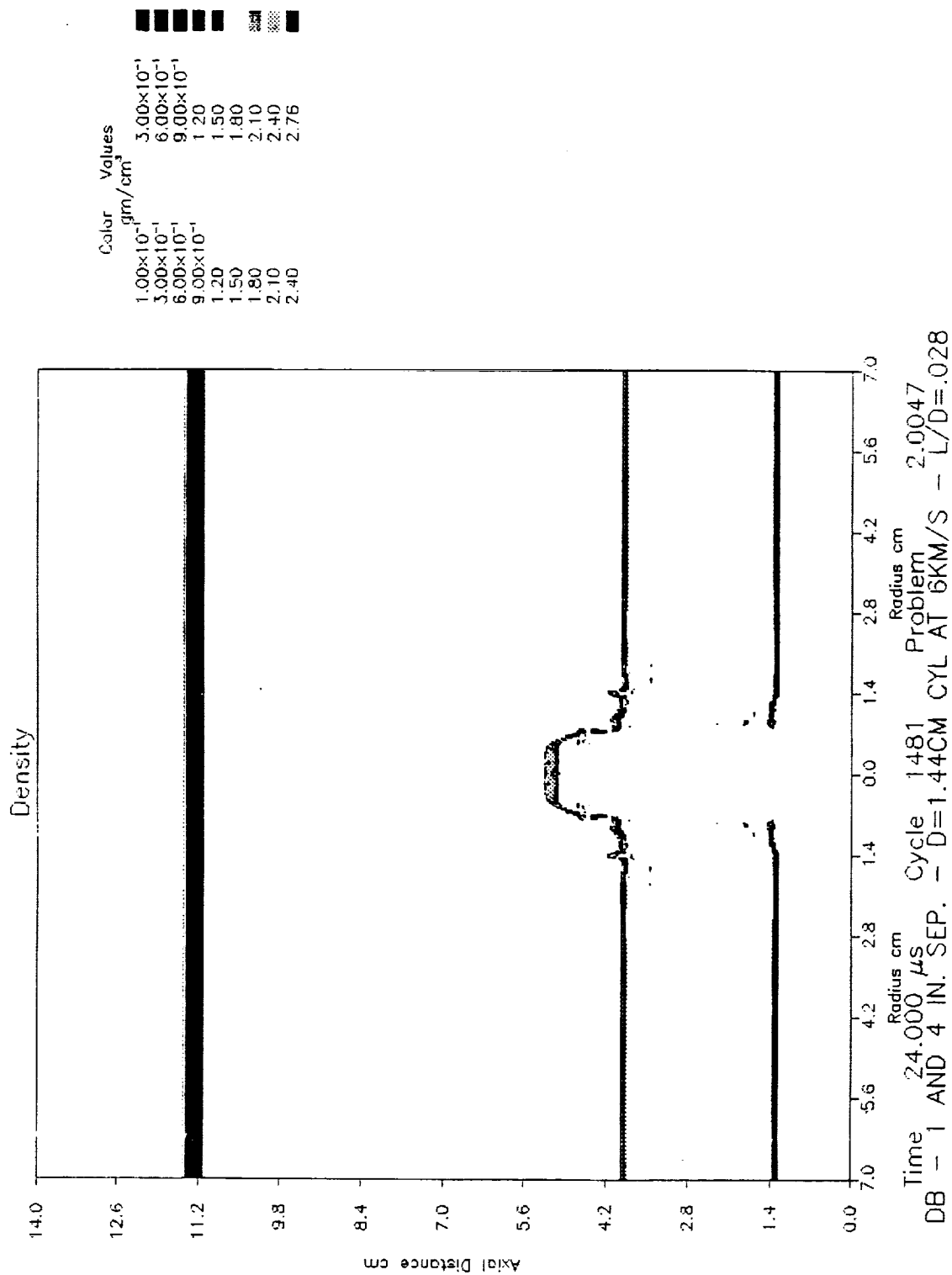


Figure 29b. HULL Code Impact Simulation NR-47-Cylindrical Projectile, Double-Bumper System, L/d = 0.0277, t = 24.000  $\mu$ s.

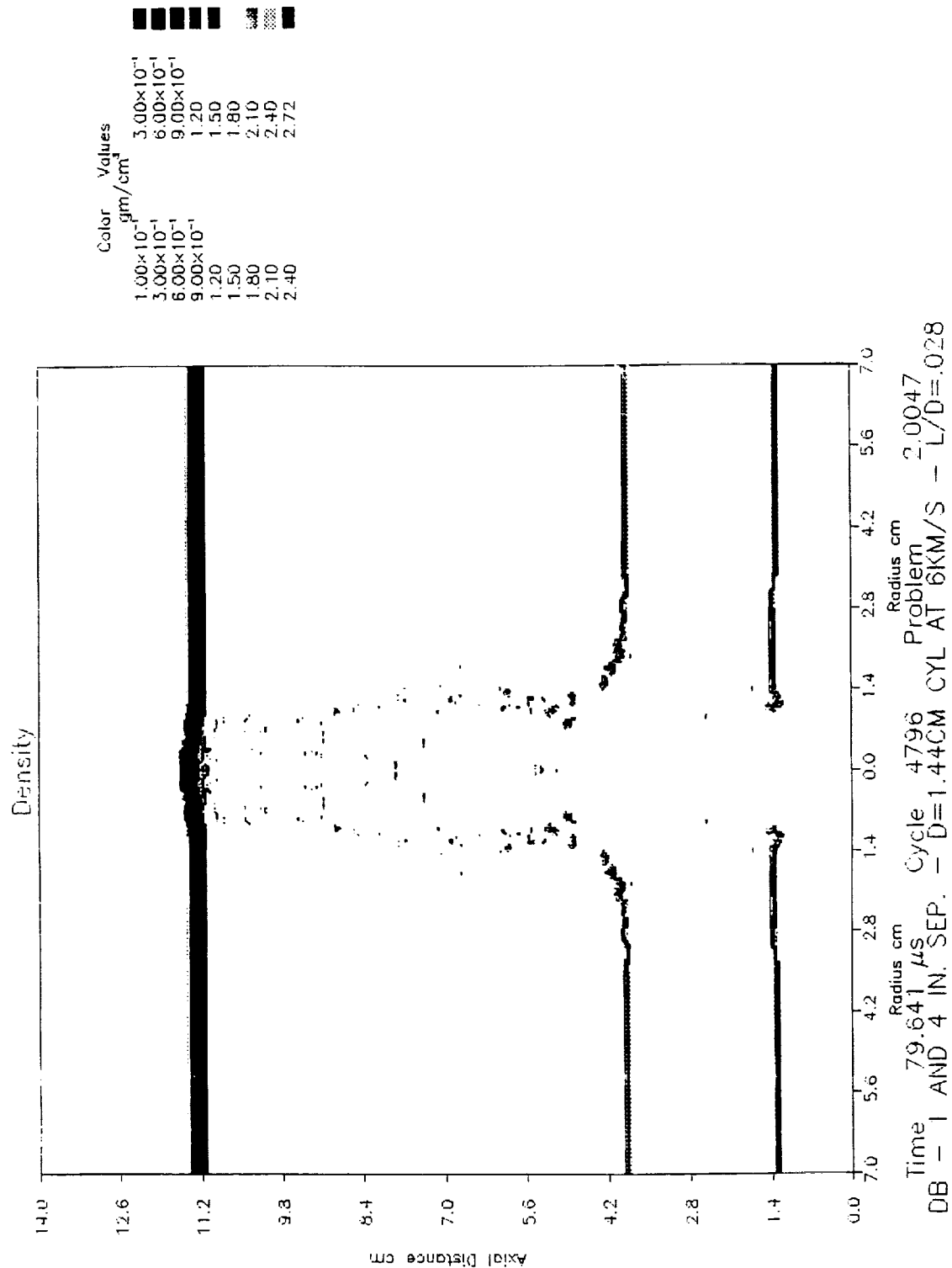



Figure 29c. HULL Code Impact Simulation NR-47-Cylindrical Projectile, Double-Bumper System, L/d = 0.0277, t = 79.641  $\mu$ s.





REPORT DOCUMENTATION PAGE			Form Approved OMB No. 0704-0188	
<small>Public reporting burden for this collection of information is estimated to average 7.5 minutes per response, including the time for reviewing existing data sources, gathering and maintaining the data needed, and completing and reviewing the collection of information. Send comments regarding this burden estimate or any other aspect of this collection of information, including suggestions for reducing this burden, to Washington Headquarters Services, Directorate for Information Operations and Reports, 1215 Jefferson Davis Highway, Suite 1204, Arlington, VA 22202-4302, and to the Office of Management and Budget, Paperwork Reduction Project (0704-0188), Washington, DC 20503.</small>				
1. AGENCY USE ONLY (Leave blank)	2. REPORT DATE January 1993	3. REPORT TYPE AND DATES COVERED Contractor Report		
4. TITLE AND SUBTITLE Predicting Multi-Wall Structural Response to Hypervelocity Impact Using the Hull Code		5. FUNDING NUMBERS Contract NAS8-36955/D.O. 74		
6. AUTHOR(S) William P. Schonberg				
7. PERFORMING ORGANIZATION NAME(S) AND ADDRESS(ES) Dept. of Mechanical Engineering University of Alabama in Huntsville Huntsville, AL 35899		8. PERFORMING ORGANIZATION REPORT NUMBER  M-710		
9. SPONSORING / MONITORING AGENCY NAME(S) AND ADDRESS(ES) National Aeronautics and Space Administration George C. Marshall Space Flight Center Marshall Space Flight Center, AL 35812		10. SPONSORING / MONITORING AGENCY REPORT NUMBER  NASA CR-4486		
11. SUPPLEMENTARY NOTES Contract Monitor: Miria M. Finckenor Marshall Space Flight Center, AL 35812				
12a. DISTRIBUTION / AVAILABILITY STATEMENT Unclassified - Unlimited Subject Category: 18		12b. DISTRIBUTION CODE  		
13. ABSTRACT (Maximum 200 words)  Previously, multi-wall structures have been analyzed extensively, primarily through experiment, as a means of increasing the meteoroid/space debris impact protection of spacecraft. As structural configurations become more varied, the number of tests required to characterize their response increases dramatically. As an alternative to experimental testing, numerical modeling of high-speed impact phenomena is often being used to predict the response of a variety of structural systems under different impact loading conditions. This report shows the results of comparing experimental tests to Hull Hydrodynamic Computer Code predictions. Also, the results of a numerical parametric study of multi-wall structural response to hypervelocity cylindrical projectile impact are presented.				
14. SUBJECT TERMS Hypervelocity, space debris, meteoroid, impact testing, hydrodynamic, impact damage, space structures		15. NUMBER OF PAGES 96		
		16. PRICE CODE A05		
17. SECURITY CLASSIFICATION OF REPORT Unclassified	18. SECURITY CLASSIFICATION OF THIS PAGE Unclassified	19. SECURITY CLASSIFICATION OF ABSTRACT Unclassified	20. LIMITATION OF ABSTRACT Unlimited	